

# The IceCube Neutrino Observatory

## Contributions to ICRC 2015 Part III: Cosmic Rays

---

### The IceCube Collaboration

#### Contents

<b>1</b>	<b>Search for High Energy Neutron Point Sources with IceTop — PoS(ICRC2015)0250</b>	<b>5</b>
<b>2</b>	<b>High <math>p_T</math> muons from cosmic ray air showers in IceCube — PoS(ICRC2015)0256</b>	<b>13</b>
<b>3</b>	<b>Surface muons in IceTop — PoS(ICRC2015)0267</b>	<b>21</b>
<b>4</b>	<b>Anisotropy in Cosmic-Ray Arrival Directions Using IceCube and IceTop — PoS(ICRC2015)0274</b>	<b>29</b>
<b>5</b>	<b>Latest Results on Cosmic Ray Spectrum and Composition from Three Years of IceTop and IceCube — PoS(ICRC2015)0334</b>	<b>37</b>
<b>6</b>	<b>Studying Cosmic Ray Composition with IceTop using Muon and Electromagnetic Lateral Distributions — PoS(ICRC2015)0338</b>	<b>45</b>
<b>7</b>	<b>Cosmic Ray Physics with the IceCube Observatory — PoS(ICRC2015)0365</b>	<b>53</b>
<b>8</b>	<b>An IceTop module for the IceCube Masterclass — PoS(ICRC2015)0576</b>	<b>61</b>
<b>9</b>	<b>A Function to Describe Attenuation of Cosmic Ray Air Shower Particles in Snow — PoS(ICRC2015)0628</b>	<b>68</b>
<b>10</b>	<b>IceTop as Veto for IceCube — PoS(ICRC2015)1086</b>	<b>76</b>
<b>11</b>	<b>Full-Sky Analysis of Cosmic-Ray Anisotropy with IceCube and HAWC — PoS(ICRC2015)0444</b>	

[arXiv:1510.04134](https://arxiv.org/abs/1510.04134)

*The 34th International Cosmic Ray Conference,  
30 July- 6 August, 2015  
The Hague, The Netherlands*

## IceCube Collaboration Member List

M. G. Aartsen<sup>2</sup>, K. Abraham<sup>32</sup>, M. Ackermann<sup>48</sup>, J. Adams<sup>15</sup>, J. A. Aguilar<sup>12</sup>, M. Ahlers<sup>29</sup>, M. Ahrens<sup>39</sup>, D. Altmann<sup>23</sup>, T. Anderson<sup>45</sup>, I. Anseau<sup>12</sup>, M. Archinger<sup>30</sup>, C. Argüelles<sup>29</sup>, T. C. Arlen<sup>45</sup>, J. Auffenberg<sup>1</sup>, X. Bai<sup>37</sup>, S. W. Barwick<sup>26</sup>, V. Baum<sup>30</sup>, R. Bay<sup>7</sup>, J. J. Beatty<sup>17,18</sup>, J. Becker Tjus<sup>10</sup>, K.-H. Becker<sup>47</sup>, E. Beiser<sup>29</sup>, S. BenZvi<sup>29</sup>, P. Berghaus<sup>48</sup>, D. Berley<sup>16</sup>, E. Bernardini<sup>48</sup>, A. Bernhard<sup>32</sup>, D. Z. Besson<sup>27</sup>, G. Binder<sup>8,7</sup>, D. Bindig<sup>47</sup>, M. Bissok<sup>1</sup>, E. Blaufuss<sup>16</sup>, J. Blumenthal<sup>1</sup>, D. J. Boersma<sup>46</sup>, C. Boehm<sup>39</sup>, M. Börner<sup>20</sup>, F. Bos<sup>10</sup>, D. Bose<sup>41</sup>, S. Böser<sup>30</sup>, O. Botner<sup>46</sup>, J. Braun<sup>29</sup>, L. Brayeux<sup>13</sup>, H.-P. Bretz<sup>48</sup>, N. Buzinsky<sup>22</sup>, J. Casey<sup>5</sup>, M. Casier<sup>13</sup>, E. Cheung<sup>16</sup>, D. Chirkin<sup>29</sup>, A. Christov<sup>24</sup>, K. Clark<sup>42</sup>, L. Classen<sup>23</sup>, S. Coenders<sup>32</sup>, D. F. Cowen<sup>45,44</sup>, A. H. Cruz Silva<sup>48</sup>, J. Daughhetee<sup>5</sup>, J. C. Davis<sup>17</sup>, M. Day<sup>29</sup>, J. P. A. M. de André<sup>21</sup>, C. De Clercq<sup>13</sup>, E. del Pino Rosendo<sup>30</sup>, H. Dembinski<sup>33</sup>, S. De Ridder<sup>25</sup>, P. Desiati<sup>29</sup>, K. D. de Vries<sup>13</sup>, G. de Wasseige<sup>13</sup>, M. de With<sup>9</sup>, T. DeYoung<sup>21</sup>, J. C. Díaz-Vélez<sup>29</sup>, V. di Lorenzo<sup>30</sup>, J. P. Dumm<sup>39</sup>, M. Dunkman<sup>45</sup>, R. Eagan<sup>45</sup>, B. Eberhardt<sup>30</sup>, T. Ehrhardt<sup>30</sup>, B. Eichmann<sup>10</sup>, S. Euler<sup>46</sup>, P. A. Evenson<sup>33</sup>, O. Fadiran<sup>29</sup>, S. Fahey<sup>29</sup>, A. R. Fazely<sup>6</sup>, A. Fedynitch<sup>10</sup>, J. Feintzeig<sup>29</sup>, J. Felde<sup>16</sup>, K. Filimonov<sup>7</sup>, C. Finley<sup>39</sup>, T. Fischer-Wasels<sup>47</sup>, S. Flis<sup>39</sup>, C.-C. Fösig<sup>30</sup>, T. Fuchs<sup>20</sup>, T. K. Gaisser<sup>33</sup>, R. Gaior<sup>14</sup>, J. Gallagher<sup>28</sup>, L. Gerhardt<sup>8,7</sup>, K. Ghorbani<sup>29</sup>, D. Gier<sup>1</sup>, L. Gladstone<sup>29</sup>, M. Glagla<sup>1</sup>, T. Glüsenskamp<sup>48</sup>, A. Goldschmidt<sup>8</sup>, G. Golup<sup>13</sup>, J. G. Gonzalez<sup>33</sup>, D. Góra<sup>48</sup>, D. Grant<sup>22</sup>, J. C. Groh<sup>45</sup>, A. Groß<sup>32</sup>, C. Ha<sup>8,7</sup>, C. Haack<sup>1</sup>, A. Haj Ismail<sup>25</sup>, A. Hallgren<sup>46</sup>, F. Halzen<sup>29</sup>, B. Hansmann<sup>1</sup>, K. Hanson<sup>29</sup>, D. Hebecker<sup>9</sup>, D. Heereman<sup>12</sup>, K. Helbing<sup>47</sup>, R. Hellauer<sup>16</sup>, D. Hellwig<sup>1</sup>, S. Hickford<sup>47</sup>, J. Hignight<sup>21</sup>, G. C. Hill<sup>2</sup>, K. D. Hoffman<sup>16</sup>, R. Hoffmann<sup>47</sup>, K. Holzappel<sup>32</sup>, A. Homeier<sup>11</sup>, K. Hoshina<sup>29,a</sup>, F. Huang<sup>45</sup>, M. Huber<sup>32</sup>, W. Huelsnitz<sup>16</sup>, P. O. Hulth<sup>39</sup>, K. Hultqvist<sup>39</sup>, S. In<sup>41</sup>, A. Ishihara<sup>14</sup>, E. Jacobi<sup>48</sup>, G. S. Japaridze<sup>4</sup>, K. Jero<sup>29</sup>, M. Jurkovic<sup>32</sup>, B. Kaminsky<sup>48</sup>, A. Kappes<sup>23</sup>, T. Karg<sup>48</sup>, A. Karle<sup>29</sup>, M. Kauer<sup>29,34</sup>, A. Keivani<sup>45</sup>, J. L. Kelley<sup>29</sup>, J. Kemp<sup>1</sup>, A. Kheirandish<sup>29</sup>, J. Kiryluk<sup>40</sup>, J. Kläs<sup>47</sup>, S. R. Klein<sup>8,7</sup>, G. Kohlen<sup>31</sup>, R. Koirala<sup>33</sup>, H. Kolanoski<sup>9</sup>, R. Konietz<sup>1</sup>, A. Koob<sup>1</sup>, L. Köpke<sup>30</sup>, C. Kopper<sup>22</sup>, S. Kopper<sup>47</sup>, D. J. Koskinen<sup>19</sup>, M. Kowalski<sup>9,48</sup>, K. Krings<sup>32</sup>, G. Kroll<sup>30</sup>, M. Kroll<sup>10</sup>, J. Kunnen<sup>13</sup>, N. Kurahashi<sup>36</sup>, T. Kuwabara<sup>14</sup>, M. Labare<sup>25</sup>, J. L. Lanfranchi<sup>45</sup>, M. J. Larson<sup>19</sup>, M. Lesiak-Bzdak<sup>40</sup>, M. Leuermann<sup>1</sup>, J. Leuner<sup>1</sup>, L. Lu<sup>14</sup>, J. Lünemann<sup>13</sup>, J. Madsen<sup>38</sup>, G. Maggi<sup>13</sup>, K. B. M. Mahn<sup>21</sup>, R. Maruyama<sup>34</sup>, K. Mase<sup>14</sup>, H. S. Matis<sup>8</sup>, R. Maunu<sup>16</sup>, F. McNally<sup>29</sup>, K. Meagher<sup>12</sup>, M. Medici<sup>19</sup>, A. Meli<sup>25</sup>, T. Menne<sup>20</sup>, G. Merino<sup>29</sup>, T. Meures<sup>12</sup>, S. Miarecki<sup>8,7</sup>, E. Middell<sup>48</sup>, E. Middlemas<sup>29</sup>, L. Mohrmann<sup>48</sup>, T. Montaruli<sup>24</sup>, R. Morse<sup>29</sup>, R. Nahnauer<sup>48</sup>, U. Naumann<sup>47</sup>, G. Neer<sup>21</sup>, H. Niederhausen<sup>40</sup>, S. C. Nowicki<sup>22</sup>, D. R. Nygren<sup>8</sup>, A. Obertacke<sup>47</sup>, A. Olivás<sup>16</sup>, A. Omairat<sup>47</sup>, A. O'Murchadha<sup>12</sup>, T. Palczewski<sup>43</sup>, H. Pandya<sup>33</sup>, L. Paul<sup>1</sup>, J. A. Pepper<sup>43</sup>, C. Pérez de los Heros<sup>46</sup>, C. Pfendner<sup>17</sup>, D. Pieloth<sup>20</sup>, E. Pinat<sup>12</sup>, J. Posselt<sup>47</sup>, P. B. Price<sup>7</sup>, G. T. Przybylski<sup>8</sup>, J. Pütz<sup>1</sup>, M. Quinlan<sup>45</sup>, C. Raab<sup>12</sup>, L. Rädcl<sup>1</sup>, M. Rameez<sup>24</sup>, K. Rawlins<sup>3</sup>, R. Reimann<sup>1</sup>, M. Relich<sup>14</sup>, E. Resconi<sup>32</sup>, W. Rhode<sup>20</sup>, M. Richman<sup>36</sup>, S. Richter<sup>29</sup>, B. Riedel<sup>22</sup>, S. Robertson<sup>2</sup>, M. Rongen<sup>1</sup>, C. Rott<sup>41</sup>, T. Ruhe<sup>20</sup>, D. Ryckbosch<sup>25</sup>, S. M. Saba<sup>10</sup>, L. Sabbatini<sup>29</sup>, H.-G. Sander<sup>30</sup>, A. Sandrock<sup>20</sup>, J. Sandroos<sup>30</sup>, S. Sarkar<sup>19,35</sup>, K. Schatto<sup>30</sup>, F. Scheriau<sup>20</sup>, M. Schimp<sup>1</sup>, T. Schmidt<sup>16</sup>, M. Schmitz<sup>20</sup>, S. Schoenen<sup>1</sup>, S. Schöneberg<sup>10</sup>, A. Schönwald<sup>48</sup>, L. Schulte<sup>11</sup>, D. Seckel<sup>33</sup>, S. Seunarine<sup>38</sup>, R. Shanidze<sup>48</sup>, M. W. E. Smith<sup>45</sup>, D. Soldin<sup>47</sup>, M. Song<sup>16</sup>, G. M. Spiczak<sup>38</sup>, C. Spiering<sup>48</sup>, M. Stahlberg<sup>1</sup>, M. Stamatikos<sup>17,b</sup>, T. Stanev<sup>33</sup>, N. A. Stanisha<sup>45</sup>, A. Stasik<sup>48</sup>, T. Stezelberger<sup>8</sup>, R. G. Stokstad<sup>8</sup>, A. Stöbl<sup>48</sup>, R. Ström<sup>46</sup>, N. L. Strotjohann<sup>48</sup>, G. W. Sullivan<sup>16</sup>, M. Sutherland<sup>17</sup>, H. Taavola<sup>46</sup>, I. Taboada<sup>5</sup>, S. Ter-Antonyan<sup>6</sup>, A. Terliuk<sup>48</sup>, G. Tešić<sup>45</sup>, S. Tilav<sup>33</sup>, P. A. Toale<sup>43</sup>, M. N. Tobin<sup>29</sup>, S. Toscano<sup>13</sup>, D. Tosi<sup>29</sup>, M. Tselengidou<sup>23</sup>, A. Turcati<sup>32</sup>, E. Unger<sup>46</sup>, M. Usner<sup>48</sup>, S. Vallecorsa<sup>24</sup>, J. Vandenbroucke<sup>29</sup>, N. van Eijndhoven<sup>13</sup>,

S. Vanheule<sup>25</sup>, J. van Santen<sup>29</sup>, J. Veenkamp<sup>32</sup>, M. Vehring<sup>1</sup>, M. Voge<sup>11</sup>, M. Vraeghe<sup>25</sup>, C. Walck<sup>39</sup>, A. Wallace<sup>2</sup>, M. Wallraff<sup>1</sup>, N. Wandkowsky<sup>29</sup>, Ch. Weaver<sup>22</sup>, C. Wendt<sup>29</sup>, S. Westerhoff<sup>29</sup>, B. J. Whelan<sup>2</sup>, N. Whitehorn<sup>29</sup>, C. Wichary<sup>1</sup>, K. Wiebe<sup>30</sup>, C. H. Wiebusch<sup>1</sup>, L. Wille<sup>29</sup>, D. R. Williams<sup>43</sup>, H. Wissing<sup>16</sup>, M. Wolf<sup>39</sup>, T. R. Wood<sup>22</sup>, K. Woschnagg<sup>7</sup>, D. L. Xu<sup>43</sup>, X. W. Xu<sup>6</sup>, Y. Xu<sup>40</sup>, J. P. Yanez<sup>48</sup>, G. Yodh<sup>26</sup>, S. Yoshida<sup>14</sup>, M. Zoll<sup>39</sup>

<sup>1</sup>III. Physikalisches Institut, RWTH Aachen University, D-52056 Aachen, Germany

<sup>2</sup>Department of Physics, University of Adelaide, Adelaide, 5005, Australia

<sup>3</sup>Dept. of Physics and Astronomy, University of Alaska Anchorage, 3211 Providence Dr., Anchorage, AK 99508, USA

<sup>4</sup>CTSPS, Clark-Atlanta University, Atlanta, GA 30314, USA

<sup>5</sup>School of Physics and Center for Relativistic Astrophysics, Georgia Institute of Technology, Atlanta, GA 30332, USA

<sup>6</sup>Dept. of Physics, Southern University, Baton Rouge, LA 70813, USA

<sup>7</sup>Dept. of Physics, University of California, Berkeley, CA 94720, USA

<sup>8</sup>Lawrence Berkeley National Laboratory, Berkeley, CA 94720, USA

<sup>9</sup>Institut für Physik, Humboldt-Universität zu Berlin, D-12489 Berlin, Germany

<sup>10</sup>Fakultät für Physik & Astronomie, Ruhr-Universität Bochum, D-44780 Bochum, Germany

<sup>11</sup>Physikalisches Institut, Universität Bonn, Nussallee 12, D-53115 Bonn, Germany

<sup>12</sup>Université Libre de Bruxelles, Science Faculty CP230, B-1050 Brussels, Belgium

<sup>13</sup>Vrije Universiteit Brussel, Dienst ELEM, B-1050 Brussels, Belgium

<sup>14</sup>Dept. of Physics, Chiba University, Chiba 263-8522, Japan

<sup>15</sup>Dept. of Physics and Astronomy, University of Canterbury, Private Bag 4800, Christchurch, New Zealand

<sup>16</sup>Dept. of Physics, University of Maryland, College Park, MD 20742, USA

<sup>17</sup>Dept. of Physics and Center for Cosmology and Astro-Particle Physics, Ohio State University, Columbus, OH 43210, USA

<sup>18</sup>Dept. of Astronomy, Ohio State University, Columbus, OH 43210, USA

<sup>19</sup>Niels Bohr Institute, University of Copenhagen, DK-2100 Copenhagen, Denmark

<sup>20</sup>Dept. of Physics, TU Dortmund University, D-44221 Dortmund, Germany

<sup>21</sup>Dept. of Physics and Astronomy, Michigan State University, East Lansing, MI 48824, USA

<sup>22</sup>Dept. of Physics, University of Alberta, Edmonton, Alberta, Canada T6G 2E1

<sup>23</sup>Erlangen Centre for Astroparticle Physics, Friedrich-Alexander-Universität Erlangen-Nürnberg, D-91058 Erlangen, Germany

<sup>24</sup>Département de physique nucléaire et corpusculaire, Université de Genève, CH-1211 Genève, Switzerland

<sup>25</sup>Dept. of Physics and Astronomy, University of Gent, B-9000 Gent, Belgium

<sup>26</sup>Dept. of Physics and Astronomy, University of California, Irvine, CA 92697, USA

<sup>27</sup>Dept. of Physics and Astronomy, University of Kansas, Lawrence, KS 66045, USA

<sup>28</sup>Dept. of Astronomy, University of Wisconsin, Madison, WI 53706, USA

<sup>29</sup>Dept. of Physics and Wisconsin IceCube Particle Astrophysics Center, University of Wisconsin, Madison, WI 53706, USA

<sup>30</sup>Institute of Physics, University of Mainz, Staudinger Weg 7, D-55099 Mainz, Germany

- <sup>31</sup>Université de Mons, 7000 Mons, Belgium
- <sup>32</sup>Technische Universität München, D-85748 Garching, Germany
- <sup>33</sup>Bartol Research Institute and Dept. of Physics and Astronomy, University of Delaware, Newark, DE 19716, USA
- <sup>34</sup>Dept. of Physics, Yale University, New Haven, CT 06520, USA
- <sup>35</sup>Dept. of Physics, University of Oxford, 1 Keble Road, Oxford OX1 3NP, UK
- <sup>36</sup>Dept. of Physics, Drexel University, 3141 Chestnut Street, Philadelphia, PA 19104, USA
- <sup>37</sup>Physics Department, South Dakota School of Mines and Technology, Rapid City, SD 57701, USA
- <sup>38</sup>Dept. of Physics, University of Wisconsin, River Falls, WI 54022, USA
- <sup>39</sup>Oskar Klein Centre and Dept. of Physics, Stockholm University, SE-10691 Stockholm, Sweden
- <sup>40</sup>Dept. of Physics and Astronomy, Stony Brook University, Stony Brook, NY 11794-3800, USA
- <sup>41</sup>Dept. of Physics, Sungkyunkwan University, Suwon 440-746, Korea
- <sup>42</sup>Dept. of Physics, University of Toronto, Toronto, Ontario, Canada, M5S 1A7
- <sup>43</sup>Dept. of Physics and Astronomy, University of Alabama, Tuscaloosa, AL 35487, USA
- <sup>44</sup>Dept. of Astronomy and Astrophysics, Pennsylvania State University, University Park, PA 16802, USA
- <sup>45</sup>Dept. of Physics, Pennsylvania State University, University Park, PA 16802, USA
- <sup>46</sup>Dept. of Physics and Astronomy, Uppsala University, Box 516, S-75120 Uppsala, Sweden
- <sup>47</sup>Dept. of Physics, University of Wuppertal, D-42119 Wuppertal, Germany
- <sup>48</sup>DESY, D-15735 Zeuthen, Germany
- <sup>a</sup>Earthquake Research Institute, University of Tokyo, Bunkyo, Tokyo 113-0032, Japan
- <sup>b</sup>NASA Goddard Space Flight Center, Greenbelt, MD 20771, USA

**Acknowledgment:** We acknowledge the support from the following agencies: U.S. National Science Foundation-Office of Polar Programs, U.S. National Science Foundation-Physics Division, University of Wisconsin Alumni Research Foundation, the Grid Laboratory Of Wisconsin (GLOW) grid infrastructure at the University of Wisconsin - Madison, the Open Science Grid (OSG) grid infrastructure; U.S. Department of Energy, and National Energy Research Scientific Computing Center, the Louisiana Optical Network Initiative (LONI) grid computing resources; Natural Sciences and Engineering Research Council of Canada, WestGrid and Compute/Calcul Canada; Swedish Research Council, Swedish Polar Research Secretariat, Swedish National Infrastructure for Computing (SNIC), and Knut and Alice Wallenberg Foundation, Sweden; German Ministry for Education and Research (BMBF), Deutsche Forschungsgemeinschaft (DFG), Helmholtz Alliance for Astroparticle Physics (HAP), Research Department of Plasmas with Complex Interactions (Bochum), Germany; Fund for Scientific Research (FNRS-FWO), FWO Odysseus programme, Flanders Institute to encourage scientific and technological research in industry (IWT), Belgian Federal Science Policy Office (Belspo); University of Oxford, United Kingdom; Marsden Fund, New Zealand; Australian Research Council; Japan Society for Promotion of Science (JSPS); the Swiss National Science Foundation (SNSF), Switzerland; National Research Foundation of Korea (NRF); Danish National Research Foundation, Denmark (DNRF)

## Search for High Energy Neutron Point Sources with IceTop

---

**The IceCube Collaboration<sup>†</sup>,**

<sup>†</sup>[http://icecube.wisc.edu/collaboration/authors/icrc15\\_icecube](http://icecube.wisc.edu/collaboration/authors/icrc15_icecube)

*E-mail:* [sutherland.54@osu.edu](mailto:sutherland.54@osu.edu)

IceTop can detect an astrophysical flux of neutrons from Galactic sources as an excess of cosmic ray air showers arriving from the source direction. Neutrons are undeflected by the Galactic magnetic field and can typically travel  $10 (E / \text{PeV})$  pc before decay. Two searches through the IceTop dataset are performed to look for a statistically significant excess of events with energies above 10 PeV ( $10^{16}$  eV) arriving within a small solid angle. The all-sky search method covers from  $-90^\circ$  to approximately  $-50^\circ$  in declination. A targeted search is also performed, looking for significant correlation with candidate sources in different target sets. Flux upper limits can be set in both searches.

**Corresponding authors:** Michael S. Sutherland<sup>1\*</sup>,

<sup>1</sup>*Department of Physics and the Center for Cosmology and Astro-Particle Physics,  
The Ohio State University,  
Columbus, Ohio 43210, USA*

*The 34th International Cosmic Ray Conference,  
30 July- 6 August, 2015  
The Hague, The Netherlands*

---

\*Speaker.

## 1. Introduction

Secondary neutral particles are an expected signature of hadronic acceleration in Galactic sources. These particles would be produced as the cosmic ray primaries interact within the dense environment surrounding their source [1]. A source of high energy neutrons would manifest as a point source in cosmic ray arrival directions since neutrons are not deflected by magnetic fields. Because of the energy-dependent neutron lifetime, the search is sensitive to sources within a distance of  $\approx 10 E_{\text{PeV}}$  parsecs to Earth. Since plausible accelerators are no closer than tens of pc, searches at energies above 10 PeV are the most promising.

The Pierre Auger Observatory recently performed a search [2, 3] at ultra-high energies ( $> \text{EeV}$ ) finding no significant signal excesses or correlations with catalogs of Galactic objects and establishing flux upper limits. KASCADE [4] and CASA-MIA [5] found no point sources in the northern sky, also resulting in flux limits. AGASA [6] and a re-analysis [7] of SUGAR data reported excesses towards the Galactic center, although these were later not confirmed by the Pierre Auger analyses.

In this analysis, we perform two searches using four years of IceTop data: one search for general hotspots on the sky and another search for correlations with nearby Galactic sources. This latter analysis is not optimized to identify specific types of neutral particles. A dedicated photon search will be reported later.

## 2. IceTop Reconstructions and Dataset

IceTop [8], located 2835 m above sea level, is the surface air shower array of the IceCube Neutrino Observatory at the geographical South Pole. Its current configuration consists of 81 stations spread over an area covering  $1 \text{ km}^2$  with an average station separation of 125 m. A single station is comprised of a pair of tanks filled with frozen water and containing two photomultiplier detectors each. Detector construction started in 2005 and finished in 2010. Cosmic ray reconstruction relies on the optical detection of Cherenkov radiation in the tanks emitted by secondary particles produced in high energy interactions in the upper atmosphere. IceTop reconstruction uses information from individual tanks, including position, deposited charge, and pulse timing, to infer the air shower direction, core location, and shower size estimate  $S_{125}$  [9]. The relationship between  $S_{125}$  and cosmic ray energy is determined by comparison with Monte Carlo simulations.

Snow accumulates on top of the stations with time which attenuates the electromagnetic portion of the shower and lowers the shower size estimate  $S_{125}$ . Snow depth measurements for each tank are performed twice a year so that the depth at the time of an event can be interpolated. A correction factor is applied during event reconstruction so that the resulting  $S_{125}$  distributions for each year are consistent. The correction is an exponential function described by an attenuation length that differs for each year.

In this analysis, events are selected by requiring good fits to the shower lateral distribution and reconstructed core locations lying within 400 m of the array center (not near the boundary). A zenith angle cut of  $37^\circ$  and an energy threshold of 10 PeV and 100 PeV for the all-sky and targeted search, respectively, are applied. 1233487 (12558) events pass these cuts for each analysis,

respectively, from a total livetime of 3.76 years. The average angular resolution above 10 PeV is approximately  $0.5^\circ$ .

### 3. Search Methods

For both search methods, top-hat<sup>1</sup> search windows are drawn around areas of interest on the sky. In the all-sky search, these windows are centered on the pixels of a high-resolution HEALPix [10] map whereas in the targeted search they are centered on the catalog objects. This map contains 19800 points within the IceTop field-of-view from which to draw the search windows with a typical spacing of  $0.6^\circ$ . The radius of the search window ( $0.52^\circ$ ) is based on the actual IceTop point-spread function and is chosen such that it optimizes the sensitivity to a point source. The data is first binned using the pixels of a higher resolution HEALPix map (“bin map”) than the search window map. The content of search window  $i$  is the sum of contents of those pixels in the bin map whose centers fall within the search window and is labelled  $n_i$  ( $b_i$ ) for the dataset (background).

The background expectation for each search window is determined by time-scrambling the dataset many times. For each time and zenith angle pair in the data, a random azimuthal angle is chosen between 0 and  $2\pi$ . This preserves the time and zenith distributions. The background bin map is taken as the average of the maps for the time-scrambled datasets.  $10^4$  ( $10^6$ ) scrambled sets are generated for the all-sky (targeted) search.

The significance of signal excesses are computed differently for each method. For the all-sky search, the significance for each window is determined using the Li-Ma method [11], where we take the Li-Ma parameters  $N_{on} = n$  and  $N_{off} = b/\alpha$ . The parameter  $\alpha$  is taken to be the  $b/\xi$ , where  $\xi$  is the sum of the contents of search windows within  $\pm 90^\circ$  in right ascension of the window of interest. This definition of  $\alpha$  provides a local estimate of  $N_{off}$  for each search window, since IceTop observes a large-scale anisotropy [12]. For the targeted search, we calculate the Poisson probability  $p_i$  for observing  $n_i$  or more events within the search window expecting  $b_i$  for each object. Fisher’s method [13] combines a set of independent probabilities to determine a single measure of significance for the set. A supplemental measure of significance is provided by Good’s method [14] which allows for weights to be assigned to each probability. Here, these weights are proportional to the object’s recorded electromagnetic flux, its exposure to IceTop, and the expected flux attenuation factor<sup>2</sup> resulting from neutron decay. The weights are normalized such that the sum is 1 for each target set. Treating the Fisher and Good probabilities ( $P_F$ ,  $P_G$ ) as individual test statistics, we calculate the fraction of time-scrambled datasets with corresponding values less than that observed with the data. This post-trials fraction is an unbiased indicator of the correlation probability between the dataset and each source set.

The targeted search is performed on three classes of candidate sources: millisecond pulsars [15],  $\gamma$ -ray pulsars [16], and high mass X-ray binaries [17] (HMXB). Distances for each candidate are cross-checked with the TeVCat catalog [18] and objects must lie within the zenith angle cut. Sources that appear in multiple sets are retained only in the smaller set, resulting in 17 objects in the  $\gamma$ -ray pulsar set, 16 objects in the msec pulsar set, and 20 objects in the HMXB set. The

<sup>1</sup>Selecting events using a hard cut on the space angle between the event direction and the window center.

<sup>2</sup>The survival probability for neutrons from the distance of the candidate source assuming a  $E^{-2}$  energy spectrum.

location of each source object are shown in Figure 1. The Galactic plane is depicted by a green band to illustrate the preferential association of the  $\gamma$ -ray pulsar and HMXB catalogs with that part of the sky.

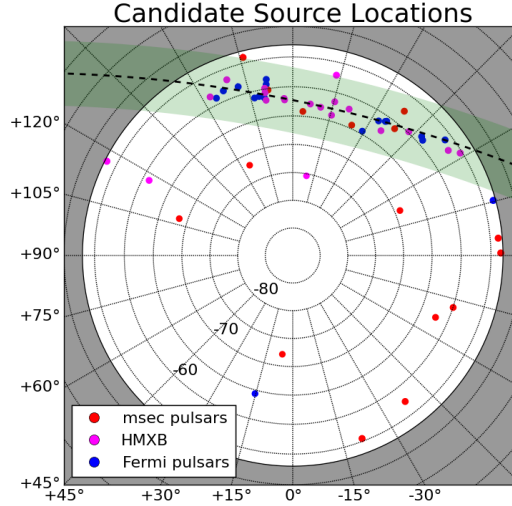


Figure 1: Equatorial polar skymap of each catalog set. The dashed black line indicates the Galactic plane and the green band shows roughly  $\pm 5^\circ$ . Each circle is  $0.5^\circ$  in radius.

Flux upper limits are calculated using  $F_{UL} = 1.39 s_{UL} / (T A \cos\theta \epsilon)$ , where  $s_{UL}$  is the upper limit on the expected number of signal events,  $T$  is the livetime,  $A \cos\theta$  is the geometrical area exposed to the search window which depends on the zenith angle, and  $\epsilon$  is the reconstruction efficiency (taken as 95%). The factor 1.39 is a compensation factor resulting from correcting  $s_{UL}$  for signal events that fall outside the search window, since the window radius is based on the angular resolution. The flux limit is a time-averaged value based on the IceTop exposure. Particularly for the objects in the targeted source sets, transient fluxes may temporarily exceed these limits.

#### 4. Results

Figure 2 shows the differential (left) and cumulative (right) distribution of Li-Ma values compared to the isotropic expectation. In both images, the blue (green) line shows the Li-Ma significance distribution for the data (isotropy). The dashed line shows the Gaussian function expected if deviations from isotropy are due only to statistical fluctuations. The gray shaded region in the cumulative plot shows the 95% containment band for isotropy; the presence of search windows with statistically significant signal excess would extend above and to the right of this band. The absence of such a feature indicates that no statistically significant signal excess is observed. Figure 3 shows skymaps of the Li-Ma and flux upper limit values for each search window. No statistically significant clustering on the sky is observed, particularly along the Galactic plane depicted by the black dotted ( $b = 0^\circ$ ) and solid ( $\pm 2.5^\circ$ ) lines.



Figure 4a shows the mean flux upper limit as a function of declination. The limits are strongest near the South Pole due to the maximal exposure, but there is greater uncertainty since there are fewer search windows.

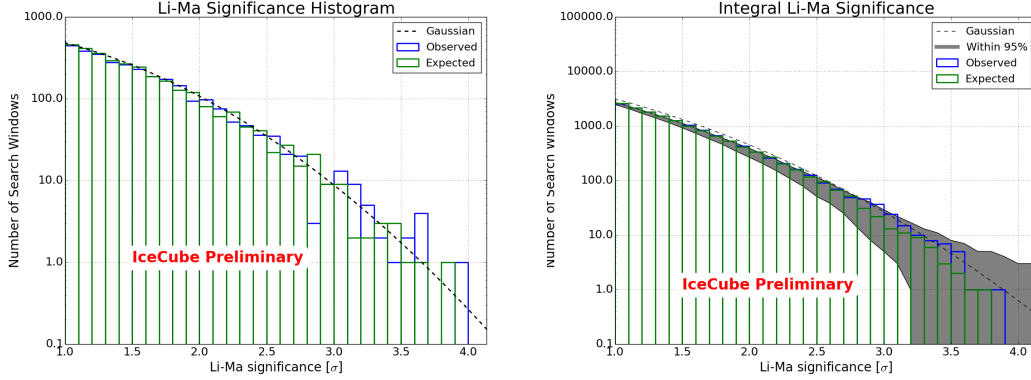


Figure 2: Histograms of Li-Ma values (blue) and the isotropic expectation (green).

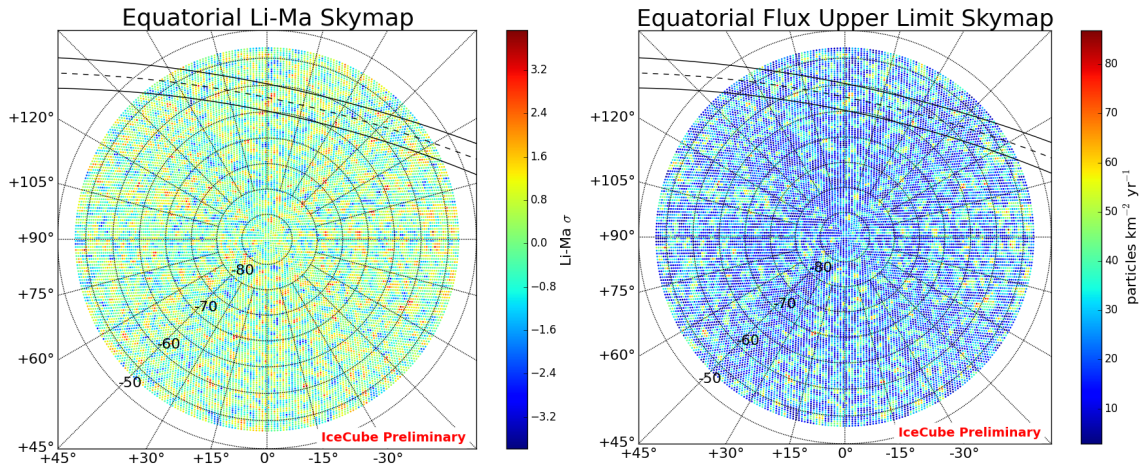


Figure 3: Equatorial polar skymap of Li-Ma (left) and flux upper limit (right) values for each search window. The solid black lines depict a  $5^\circ$  band centered on the Galactic plane.

Table 1 lists  $P_F$  and  $P_G$  for each catalog. The quantity in parentheses shows the post-trials probability value. No significant correlation is observed with any catalog. Table 2 lists details of the object with the smallest Poisson  $p$  in each catalog, including the neutron flux  $F_{UL}$  and energy flux  $F_{UL}^E$  for an  $E^{-2}$  spectrum. The post-trials probability (in parentheses) for the minimum  $p$  in each catalog also indicates that no evidence for PeV neutron flux from the candidates is observed.

There exists an underfluctuation in the data along  $b = 0^\circ$  compared to the background expectation, as illustrated in Figure 4b. The preferential clustering of the  $\gamma$ -ray pulsar and HMXB catalogs along the Galactic plane combined with this underfluctuation results in artificially high  $P_F$  and  $P_G$ . This behavior is verified by rotating the catalogs in right ascension. We also note that 4 pairs of

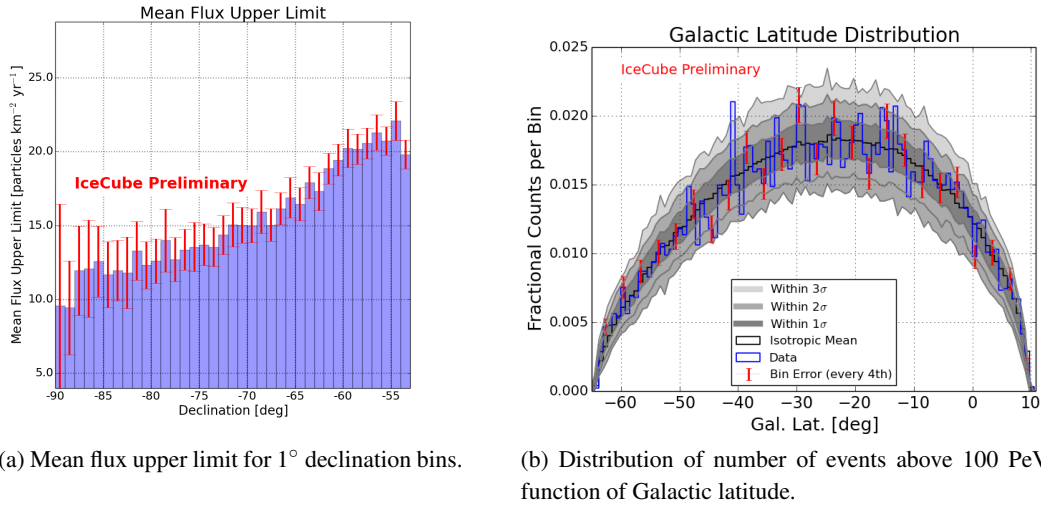


Figure 4: Left: The error bars indicate the statistical uncertainty on the mean value. The uncertainties are larger at small zenith angles since there are less search windows than at larger zenith angles. Right: The blue histogram shows the data; the black line shows the isotropic expectation from 800 time-scrambled datasets. The red error bars show the Poisson uncertainty in the data histogram and are plotted *only* for every 4th bin to reduce clutter. The gray shaded bands depict the 68%, 95%, and 99% containment bands for isotropy in each latitude bin.

Catalog	$P_F$	$P_G$
$\gamma$ -ray	0.998 (0.947)	0.887 (0.727)
msec	0.820 (0.457)	0.898 (0.792)
HMXB	0.999 (0.997)	0.945 (0.973)

Table 1: Targeted search results with each catalog. First column lists the catalog, second column lists the Fisher probability  $P_F$  and post-trials value, and third column lists the Good probability  $P_G$  and its post-trials value (in parentheses).

objects, where objects in each pair are distinct and from different catalogs, lie within  $1^\circ$  of each other. Results are consistent with Table 1 when we mask the object with the farther distance.

## 5. Summary

IceTop does not observe a statistically significant point source of cosmic ray arrival directions in an all-sky search within the field-of-view. Additionally, no significant correlation is found with known Galactic objects thought to be capable producing PeV neutrons. The mean flux upper limits for individual declination bands correspond to energy fluxes between about  $1.2 - 1.5 \text{ eV cm}^{-2} \text{ sec}^{-1}$ , which are comparable to TeV  $\gamma$  fluxes for Galactic objects [19]. Photons and neutrons can be produced through pion production of protons with ambient photons and nuclei. Photons resulting from  $\pi^0$  decay take a small fraction of the proton energy. Neutrons result from charge-exchange interactions where a  $\pi^+$  emerges with the proton's positive charge and the neutron retains most of

Catalog	Object Name	R.A. [deg]	Dec. [deg]	$n$	$b$	$F_{UL}$ [ $\text{km}^{-2} \text{yr}^{-1}$ ]	$F_{UL}^E$ [ $\text{eV cm}^{-2} \text{sec}^{-1}$ ]	$p_i$
$\gamma$ -ray	J1048-5832	162.05	-58.53	5	2.40	11.35	0.65	0.095 (0.665)
msec	J1933-6211	293.39	-62.20	6	2.57	14.87	0.86	0.047 (0.419)
HMXB	2S1417-624	215.30	-62.70	4	2.65	10.11	0.58	0.274 (0.993)

Table 2: Targeted search results for most significant object in each catalog. Columns lists the catalog name, object name, equatorial coordinates, number of events  $n$  and background expectation  $b$  within the search window, neutron number  $F_{UL}$  and energy  $F_{UL}^E$  flux upper limits, and Poisson p-value  $p_i(n, b)$  and post-trials value (in parentheses).

the energy. For parent protons with an  $E^{-2}$  spectrum, these upper limits provide constraints on the production origin of the TeV  $\gamma$ s and the energy evolution of proton spectra.

The non-observation of PeV neutron sources may simply indicate that such sources were not active during the data-taking period. Sources may emit particle jets continuously, but their number may be few and the jets are not oriented towards the Earth. Additionally, environments around any sources may not be dense enough to facilitate neutron production. These possibilities would apply if the parent proton spectra extended beyond tens of PeV, which may not be the case. IceTop observes a cosmic ray flux that becomes progressively heavier with energy and a decreasing proton fraction [20], which is about 20% at 10 PeV. Neutrons may be produced at lower energies where protons comprise a larger fraction, but the resulting lower energies severely limit neutron observations to near the production sites.

## References

- [1] R. M. Crocker *et al.*, *Astrophys. J.* **622** (2005) 892.
- [2] **Pierre Auger** Collaboration, A. Aab *et al.*, *Astrophys. J.* **760** (2012) 148.
- [3] **Pierre Auger** Collaboration, A. Aab *et al.*, *Astrophys. J.* **789** (2014) L34.
- [4] **KASCADE** Collaboration, T. Antoni *et al.*, *Astrophys. J.* **608** (2004) 865.
- [5] **CASA-MIA** Collaboration, J. Cronin *et al.*, *Phys. Rev. D* **D45** (1992) 4835.
- [6] **AGASA** Collaboration, N. Hayashida *et al.*, *Astropart. Phys.* **10** (1999) 303.
- [7] J. Bellido *et al.*, *Astropart. Phys.* **15** (2001) 167.
- [8] **IceCube** Collaboration, R. Abbasi *et al.*, *Nucl. Instrum. Meth.* **A700** (2013) 188.
- [9] **IceCube** Collaboration, M. Aartsen *et al.*, *Phys. Rev. D* **4** (2013) 042004.
- [10] K. Gorski *et al.*, *Astrophys. J.* **622** (2005) 759.
- [11] T. Li and Y. Ma, *Astrophys. J.* **272** (1983) 317.
- [12] **IceCube** Collaboration, PoS (ICRC2015) 334 these proceedings.
- [13] R. Fisher, *Statistical Methods for Research Workers*, Edinburgh: Oliver and Boyd (1925).
- [14] I. Good, *JRSS B* **17** (1955) 264.
- [15] R. Manchester *et al.*, *Astrophys. J.* **129** (2005) 1993.

- [16] **Fermi** Collaboration, A. Abdo *et al.*, *Astrophys. J. Suppl.* **208** (2013) 17.
- [17] Q. Liu *et al.*, *A&A* **455** (2007) 1165.
- [18] The TeVCat catalog, <http://tevcat.uchicago.edu>.
- [19] J. Hinton *et al.*, *ARA&A* **47** (2009) 523.
- [20] **IceCube** Collaboration, PoS (ICRC2015) 274 these proceedings.

## High $p_T$ muons from cosmic ray air showers in IceCube

---

The IceCube Collaboration<sup>†</sup>,

<sup>†</sup> [http://icecube.wisc.edu/collaboration/authors/icrc15\\_icecube](http://icecube.wisc.edu/collaboration/authors/icrc15_icecube)

E-mail: [soldin@uni-wuppertal.de](mailto:soldin@uni-wuppertal.de)

Cosmic ray air showers with primary energies above  $\gtrsim 1$  TeV can produce muons with high transverse momentum ( $p_T \gtrsim 2$  GeV). These isolated muons can have large transverse separations from the shower core, up to several hundred meters. Together with the muon bundle they form a double track signature in km<sup>3</sup>-scale neutrino telescopes such as IceCube. The muons originate from the decay of heavy hadrons, pions, and kaons produced very early in the shower development, typically in (multiple) high  $p_T$  jets. The separation from the core is a measure of the transverse momentum of the muon's parent particle and the muon lateral distribution depends on the composition of the incident nuclei. Hence, the composition of high energy cosmic rays can be determined from muon separation measurements. For  $p_T \gtrsim 2$  GeV particle interactions can be described in the context of perturbative quantum chromodynamics (pQCD). Thus, these muons may contribute to test pQCD predictions of high energy interactions involving intermediate nuclei.

We discuss the contributions from various hadrons produced in air showers to the high  $p_T$  muon flux. Based on dedicated simulations the prospects of composition measurements using high  $p_T$  muons in km<sup>3</sup>-scale neutrino telescopes are studied. We present analysis methods to study laterally separated muons in IceCube with lateral separations larger than  $\sim 135$  m.

**Corresponding author:** D. Soldin\*,

*Dept. of Physics, University of Wuppertal, 42119 Wuppertal, Germany*

*The 34th International Cosmic Ray Conference,  
30 July - 6 August, 2015  
The Hague, The Netherlands*

---

\*Speaker.

## 1. Introduction

In cosmic ray air showers with energies  $E_{\text{prim}} \gtrsim 1$  TeV, muons can be produced that have large transverse momentum ( $p_T$ ) imparted to them by their parent particles. Depending on their energy  $E_\mu$  these muons can have large angular separations  $\phi \simeq p_T/E_\mu \gtrsim 0.4^\circ$  and will diverge from the shower core while traveling to the ground. After the shower has propagated to the ground, they are observable as laterally separated muons (LS muons) that arrive with the main muon bundle. The resulting lateral separation on the ground is a direct measure of the  $p_T$  of the muon's parent. The IceCube Neutrino Observatory at the geographic South Pole is a  $\text{km}^3$ -scale detector in the antarctic ice in depths of 1450 m to 2450 m [1]. LS muons with several hundred meters separation have been observed as distinct “double track signatures” in the detector [2], which has a minimum resolvable track separation of about 135 m. Figure 1 (left) shows a simulated LS muon event in IceCube with the typical event signature of a muon bundle accompanied by the isolated LS muon. The muon's lateral separation from the shower core is related to its  $p_T$  via

$$d_T \simeq \frac{p_T \cdot H}{E_\mu \cdot \cos(\theta)}, \quad (1.1)$$

where  $H$  is its height of production and  $\theta$  the zenith angle of the arrival direction [3]. Here, and in the following, we use natural units  $c = 1$ . Figure 1 (right) shows the lateral separation as a function of the transverse momentum for a typical muon energy of 1 TeV at different zenith angles and interaction heights. The typical transverse momentum to produce laterally separated muons in IceCube is about 2 GeV, where parton interactions can be described in the context of perturbative quantum chromodynamics (pQCD) [2]. We consider muons with energies above  $E_{\mu,\text{min}} = 460$  GeV to ensure they can reach the deep ice detector [4], and a minimum transverse momentum to produce LS muons of  $p_{T,\text{min}} = 1$  GeV. In the following, the term “high  $p_T$ ” refers to transverse momenta and energies above these thresholds.

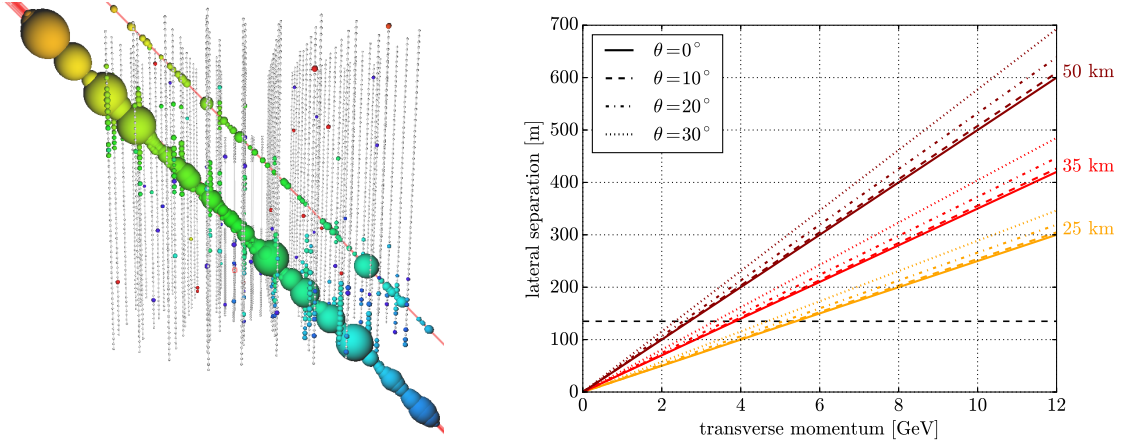


**Figure 1:** Left: Simulated LS muon event in the IceCube detector with a primary energy of  $\sim 6$  PeV and  $d_T = 232$  m. Small gray spheres indicate the detector DOMs and larger colored ones DOMs which triggered. Spheres along the muon tracks (red lines) show the simulated emitted light yield and colors indicate the time-ordering from red (early) to blue (late). The simulation also includes noise hits in the detector volume. Right: Lateral separation of a 1 TeV muon as a function of  $p_T$  for different zenith angles  $\theta$  and interaction heights.

High  $p_T$  particles are predominantly produced in the first interaction. Hence, measurements of the lateral separation distribution of LS muons can be used to test model predictions at very high energies and low Bjorken- $x$  which are not accessible at current accelerators. Moreover, these interactions can be described using pQCD and, in principle, the underlying theory is QCD rather than any phenomenological model. Additionally, it was previously shown [3, 5] that muon  $p_T$  distributions depend on the incident nuclei. Other composition measurements rely on the ratio of the measured electromagnetic energy to the number of muons [6, 7], the atmospheric depth  $X_{\max}$ , where an air shower reaches the maximum number of particles [8], or multivariate analyses that combine several observables [9]. An analysis of laterally separated muons in IceCube complements these measurements of the cosmic ray mass composition.

## 2. Simulation of high $p_T$ muon events

The fraction of laterally separated muons produced in air showers represents a rather small contribution to the total muon content inside the shower. Thus, simulating LS muon events with sufficiently large statistics using standard air shower simulation packages requires extremely high computational efforts. Moreover, previous studies have shown significant disagreement between simulations and data in the angular distribution of atmospheric muons [2, 4], especially for horizontal directions. This discrepancy is still not understood. Therefore, a detailed understanding of the underlying physics is crucial for the interpretation of such events requiring dedicated simulations.

The simulation of high  $p_T$  muon events is divided into two parts that are treated separately: the simulation of the central muon bundle and simulation of the isolated LS muon. These are re-combined after full shower propagation through the atmosphere. Although this violates energy conservation in the first interaction, the violation is below the 1% level and therefore negligible.

As a starting point cosmic ray air showers are simulated with primary energies in the relevant energy range using the CORSIKA package [10] with Sibyll 2.1 [11] to produce the typical central muon bundle signature as shown in Fig. 1. The primary spectrum is generated from a  $E^{-2}$  spectrum<sup>1</sup> in the range of  $600 \text{ GeV} \leq E_{\text{prim}} < 100 \text{ EeV}$  and re-weighted to the parametrization from Ref. [12] where the spectral index changes from  $-2.6$  to  $-3.0$  at  $E_{\text{knee}} = 4 \text{ PeV}$  (the “knee”). A full shower simulation is performed assuming proton and iron primaries respectively using CORSIKA. The propagation of the particles through the ice and the photon emission are simulated using standard IceCube software.

Laterally separated muons produced in the air shower are simulated separately using the CRMC package [13] as an interface to get access to several hadronic interaction models. The production probabilities, as well as transverse momentum and energy distributions of high  $p_T$  particles produced in the first interaction can thereby be obtained from any hadronic interaction model. The production of particles with high transverse momentum from secondary interactions is highly suppressed due to significantly lower center-of-mass energies and is therefore neglected. All high  $p_T$  hadron energies and transverse momenta are drawn from these distributions for each individual primary that was used for the pre-simulated CORSIKA shower. Hence, the kinematic variables need only be generated in the limited phase space which is relevant to produce laterally separated muons that can reach the IceCube detector.

<sup>1</sup>Showers with primary energies below 1 PeV are generated from an  $E^{-2.6}$  spectrum.

All types of secondary high  $p_T$  hadrons produced in the first interaction that predominantly contribute to the muon flux are taken into account:

- **pions and kaons:**  $\pi^\pm, K^\pm, K_L^0, \bar{K}_L^0$ .
- **prompt hadrons:**  $D^+, D^0, D_s^+, \Lambda_c^+, \Omega_c^0, \Xi_c^+, \Xi_c^0, B^+, B^0, B_s^0, B_c^+, \Lambda_b^0, J/\psi$ , and anti-particles.
- **short-lived unflavored mesons:**  $\eta, \eta', \rho^0, \omega, \phi$ , and anti-particles.

Secondary contributions from high  $p_T$  kaons and unflavored mesons that decay into pions ( $K_L^0, K_S^0, \eta, \eta', \rho^0, \rho^\pm, \omega, \phi$ , and anti-particles), as well as from  $\phi$ -mesons that can decay into kaons are also explicitly taken into account<sup>2</sup>. Since nitrogen is the most abundant element in the atmosphere (78.4%) it is used as target particle for all simulations. The contribution from oxygen (21.1%) has a similar mass number which obviates a distinctive treatment.

Figure 2 (left) shows the average number of high  $p_T$  hadrons produced per collision, the “high  $p_T$  hadron abundance”, for different primary energies obtained from EPOS-LHC [15] and QGSJet II-4 [16] assuming proton primaries. Since HIJING 1.3 [17] is the only available interaction model including a full modeling of the prompt component all distributions of prompt hadrons in this work are based on HIJING predictions<sup>3</sup> even if not explicitly denoted. Each LS muon event is weighted with the hadron abundance according to the spline interpolations shown in Fig. 2 (left, lines). Events with a high  $p_T$  hadron abundance below  $10^{-4}$  are not taken into account because high  $p_T$  particle production is highly suppressed. Additionally LS muon detection from primaries with energies  $\sim 1$  TeV is suppressed due to the natural shielding of the ice and by a subsequent high energy filtering (see Sec. 3).

Figure 2 (right) shows the transverse momentum distributions of various components for a primary energy of 1 PeV obtained from different hadronic models. A transition from soft to hard interactions that can be described in the context of pQCD is expected to be visible in these distributions as an exponential fall-off with a transition to a power law at  $p_0 \simeq 2$  GeV [2]. Thus, the  $p_T$

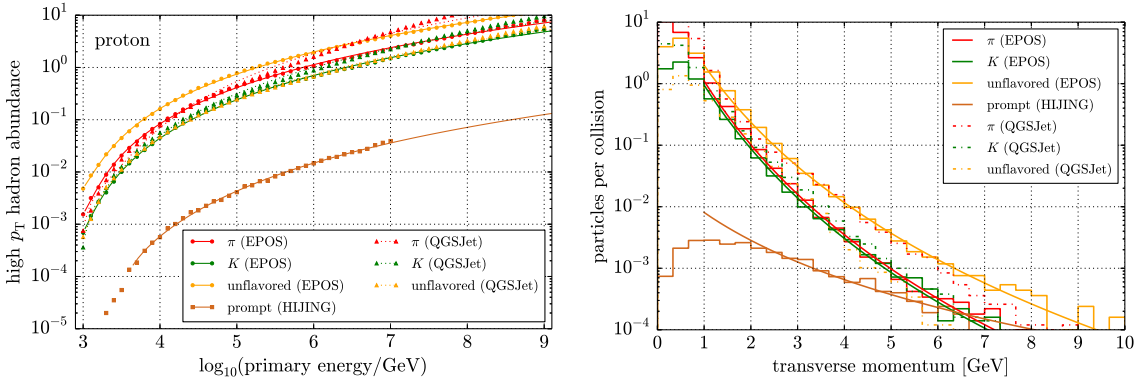


**Figure 2:** Left: High  $p_T$  hadron abundance for different interaction models. Right: Transverse momentum distribution of various hadrons with  $E_h \geq 460$  GeV for a primary energy of 1 PeV as well as corresponding fits (lines) using Eq. (2.1).

<sup>2</sup>In the QGSJet model contributions from short-lived resonances are already included in the final state spectra of stable hadrons [14] therefore secondary decays into pions and kaons are not treated explicitly.

<sup>3</sup>HIJING pion, kaon, and unflavored distributions have rather good agreement with QGSJet predictions [5].



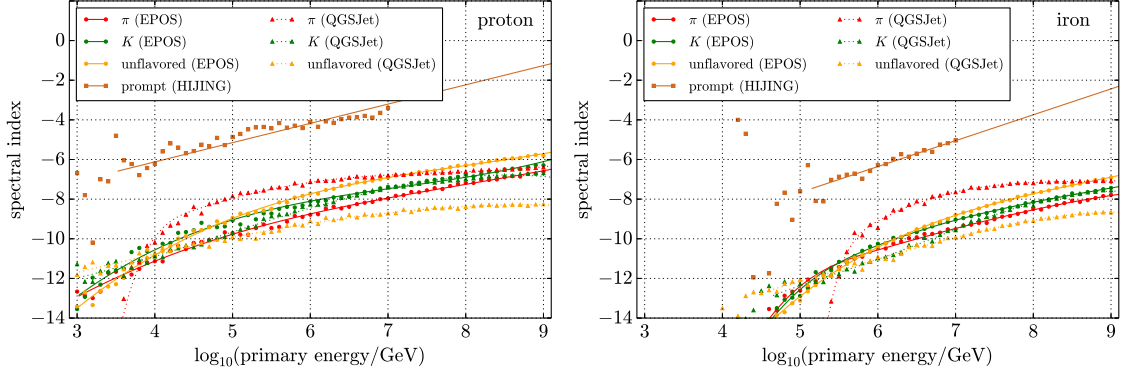


**Figure 3:** Spectral indices  $\beta$  obtained from fits using Eq. (2.1) applied to transverse momentum distributions for proton (left) and iron (right) primaries respectively and different hadronic models. The corresponding spline fits as a function of the primary energy are shown as lines.

distributions are fit with the QCD inspired “*modified Hagedorn function*” [18, 19]

$$\frac{dN}{dp_T} = \alpha \left( 1 + \frac{p_T}{p_0} \right)^\beta \quad (2.1)$$

for  $p_T \geq p_0 = 2$  GeV where  $\alpha$  and  $\beta$  are allowed to vary. This function behaves exponentially at small  $p_T$  and as a pure power law at high  $p_T$ . The lines shown in Fig. 2 (right) represent these fits. Spectral indices  $\beta(E_{\text{prim}})$  obtained for various initial energies are shown in Fig. 3 for proton (left) and iron primaries (right). The solid lines are spline interpolations used to define the spectral index as a function of the primary energy, where the end of the lines indicate where the hadron abundance drops below  $10^{-4}$ . As expected, the  $p_T$  distributions flatten with increasing initial energy and the prompt component shows a generally harder spectrum.

Using these interpolations, the spectral index  $\beta(E_{\text{prim}})$  is obtained according to the underlying primary energy for each pre-simulated CORSIKA event. The transverse momentum of the additional high  $p_T$  hadron is then generated from Eq. (2.1) over the range  $1 \text{ GeV} \leq p_T \leq 12 \text{ GeV}$  with a spectral index of  $\beta = -1$ , and re-weighted to the corresponding spectral index  $\beta(E_{\text{prim}})$ . This is done to increase the statistics of events carrying high  $p_T$  that predominantly produce large lateral separations. The energy distributions of hadrons are obtained analogously from different hadronic interaction models and several initial energies. The high  $p_T$  hadron energy of each event is then generated in the range  $E_h \geq E_{\mu, \text{min}} = 460 \text{ GeV}$  from the distribution with the simulated energy closest to the underlying primary energy.

Propagation and decay of particles is performed using the Monte Carlo method from Ref. [12] to decide if a hadron decays or re-interacts with an air molecule within the atmosphere. The cross-sections of hadron-air<sup>4</sup> interactions are obtained from the underlying hadronic model. The decay probabilities as well as all relevant branching ratios of the different hadrons into muons are included in simulation via event weighting. To estimate energy losses due to the decay, the energy fractions

<sup>4</sup>The cross-sections of prompt hadrons which cannot be used as an initial particle in any interaction model are approximated by the corresponding kaon cross-section. Since the prompt cross-sections should be somewhat smaller this results in a small underestimation of the prompt flux.

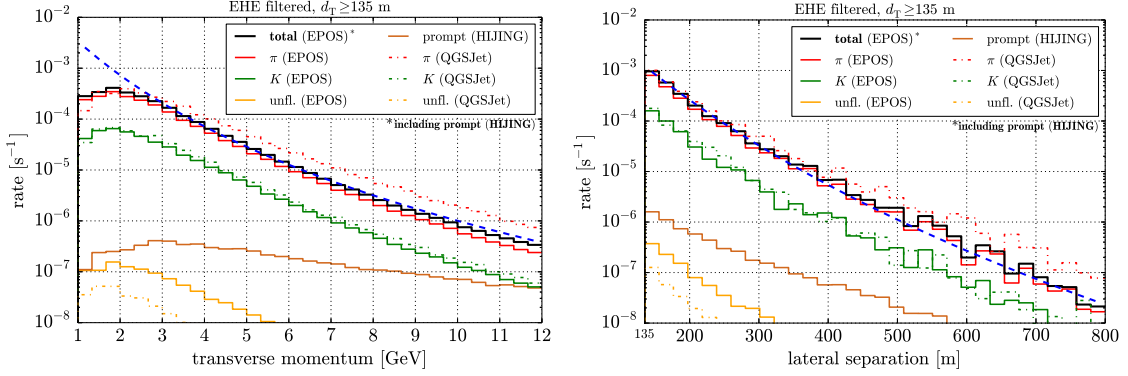


**Figure 4:** Transverse momentum (left) and lateral separation distribution (right) of simulated LS muon events in IceCube after EHE filtering and with separations above 135 m assuming proton primaries using different hadronic models. Also shown are fits using Eq. (2.1) applied to both distributions (blue lines).

$E_\mu/E_h$  of the resulting muons are obtained from PYTHIA 8.1 [20] simulations. Deflections caused by the Earth’s magnetic field as well as multiple scattering in the atmosphere are negligible for the energies and lateral separations considered here [2]. Using standard IceCube software the propagation of the LS muon and the emitted photons in the ice is simulated. Finally, the LS muon and the pre-simulated muon bundle signals are combined and the detector response simulated to form a complete laterally separated muon event in IceCube.

### 3. Simulated LS muon distributions in IceCube

LS muons are selected from the IceCube high energy filter stream (“*EHE filter*”) which keeps events with at least  $10^3$  photoelectrons in the detector [2]. Additionally, only events with lateral separations larger than 135 m are considered as LS muon events. Figure 4 (left) shows the transverse momentum distribution of simulated LS muon events passing these selection criteria for proton primaries and various parent particles based on EPOS-LHC and QGSJet II-4. As expected, the contribution of events with  $p_T \lesssim 2$  GeV is suppressed due to the constraint on minimum lateral separation despite the lower transverse momenta being overestimated (see Fig. 2). A fit using Eq. (2.1) applied to the total LS muon distribution based on EPOS for  $p_T \geq p_0 = 3$  GeV (blue line) has a spectral index of  $\beta = -6.89 \pm 0.06$ . The same fit with the replacements  $p_T \rightarrow d_T$  and  $p_0 \rightarrow d_0 = 400$  m [2] applied to the lateral separation distribution shown in Fig. 4 (right) has a spectral index  $\beta = -13.45 \pm 0.14$ . A pure-iron composition assumption (not shown) results in steeper spectra with  $\beta = -9.87 \pm 0.04$  for the transverse momentum and  $-15.50 \pm 0.21$  for the lateral distribution respectively. The prompt component shows a harder spectrum for both distributions. The simulations, including detector response, produce results consistent with those previously observed [2] and in accordance with pQCD predictions. Figure 5 (left) shows the spectral indices obtained from fits using Eq. (2.1) applied to  $p_T$  distributions within different simulated primary energy (top) and total charge intervals (bottom) for proton and iron primaries respectively. The simulated deposited total charge in the detector is given in units of the number of photoelectrons (NPE) which depends on the detector setup. It is approximately proportional to the energy loss in the detector and therefore closely related to the initial primary energy. Nearly

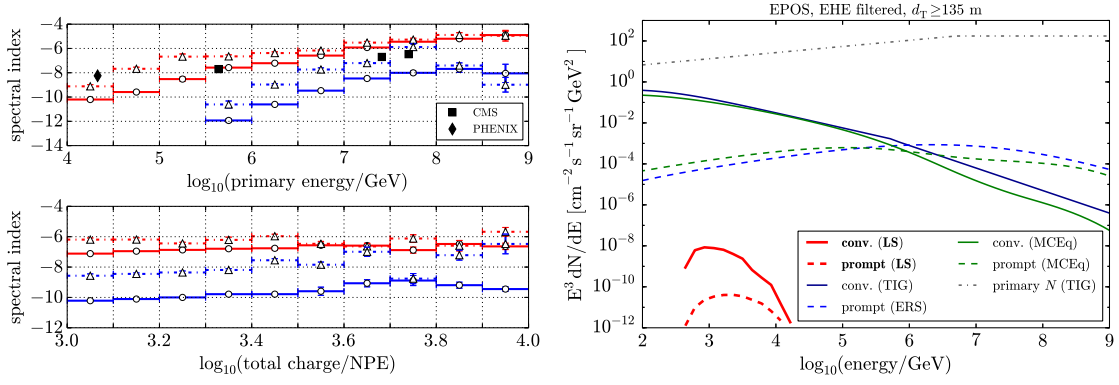


**Figure 5:** Left: Spectral indices of simulated  $p_T$  distributions within different primary energy (top) and total charge intervals in units of NPE (bottom) in IceCube. These are shown for proton (red) and iron primary interactions (blue) based on EPOS (circles) and QGSJet (triangles). Experimental data for proton-proton collisions from PHENIX [21] and CMS [22, 23] is shown for comparison. Right: Flux of LS muons in IceCube for proton primaries based on EPOS as well as muon flux predictions on surface from Ref. [12] (TIG), [24] (ERS), and [25] (MCEq) for comparison.

all LS muon events (96.1% for proton and 99.9% for iron primaries) are generated in the range  $10 \text{ TeV} \leq E_{\text{prim}} \leq 1 \text{ EeV}$ . The spectral indices show a clear separation between proton and iron assumptions. Also shown are spectral indices obtained from pion  $p_T$  distributions in proton-proton collisions from PHENIX at  $\sqrt{s} = 200 \text{ GeV}$  [21] and of charged hadron distributions from CMS at  $\sqrt{s} = 0.9 \text{ TeV}$ ,  $2.3 \text{ TeV}$ ,  $7 \text{ TeV}$  [22, 23]. The corresponding primary energies are given in the laboratory frame by  $E_{\text{prim}} = (s - 2m_p^2)/2m_p$  with proton mass  $m_p$  and the underlying assumption that all but one nucleon of each colliding ion can be regarded as spectators only. Figure 5 (right) shows the simulated energy spectrum (scaled with  $E^3$ ) of laterally separated muons assuming a pure-proton primary composition with EPOS in comparison to several theoretical predictions of the total muon flux on the surface [12, 24, 25]. Also shown is the primary spectrum used in this work [12]. The LS muon energy distribution peaks at  $E_\mu \sim 1 \text{ TeV}$  since extremely high energy muons with large separations are highly suppressed due to the  $1/E_\mu$  dependence in Eq. (1.1). The resulting total LS muon flux from proton primaries corresponds to an expected event rate of approximately 79,000 events in one year of IceCube high energy data. The event rate assuming pure-iron primary composition is roughly 21,000 events in one year of data. The corresponding event rates based on QGSJet simulations are approximately 25% higher (5% lower) for proton (iron) primaries.

#### 4. Conclusion and outlook

Muons with high transverse momentum have been observed as double track signatures in IceCube [2]. The lateral separation of these muons can be used to study their kinematic distributions and their parent particle's hadronic interactions. A method to simulate laterally separated muons was presented, including an explicit treatment of different air shower components. The simulated  $p_T$  and lateral distributions as well as the energy spectrum after high energy filtering were shown. The expected LS muon event rate is between 21,000 and 79,000 events in one year of IceCube data depending on the primary mass composition.

An analysis of laterally separated muons in IceCube based on these simulations is in preparation. Several selection criteria as well as dedicated double track reconstructions [2] will be used to get a pure sample of LS muon events to draw conclusions on the underlying physics. The simulations enable, for example, studies on the treatment of hadrons producing muons and their  $p_T$  modeling for different hadronic interaction models. Upcoming versions of hadronic interaction models with a prompt contribution to the muon flux, for example Sibyll with charm [26], can be included to further improve the simulation of laterally separated muons. Moreover, it was shown that the distributions of LS muons depend on the incident nuclei and they can therefore be used to study the cosmic ray mass composition. This complements other composition measurements and enables studies on high energy interactions of intermediate nuclei at low Bjorken- $x$ .

## References

- [1] A. Achterberg *et al.* (IceCube Collaboration), *Astropart.Phys.* **26** (2006) 155.
- [2] R. Abbasi *et al.* (IceCube Collaboration), *Phys. Rev. D* **87** (2013) 012005.
- [3] S. R. Klein, D. Chirkin for the IceCube Collab., in *Proc. of the 30th ICRC* (2007) [[arXiv:0711.0353](#)].
- [4] M. G. Aartsen *et al.* (IceCube Collaboration), (2015) [[arXiv:1506.07981](#)].
- [5] D. Soldin for the IceCube Collab., in *Proc. of the 18th ISVHECRI* (2014) [[arXiv:1411.4448](#)].
- [6] M. G. Aartsen *et al.* (IceCube Collaboration), PoS(ICRC2015)338 these proceedings (2015).
- [7] M. G. Aartsen *et al.* (IceCube Collaboration), PoS(ICRC2015)267 these proceedings (2015).
- [8] D. Kang *et al.*, in *Proc. of the 16th ISVHECRI* (2010) [[arXiv:1009.4902](#)].
- [9] M. G. Aartsen *et al.* (IceCube Collaboration), PoS(ICRC2015)334 these proceedings (2015).
- [10] D. Heck *et al.*, Tech. Rep. FZKA 6019 (Forschungszentrum Karlsruhe GmbH, Karlsruhe, 1998).
- [11] E. Ahn, R. Engel, T. Gaisser, P. Lipari, T. Stanev, *Phys. Rev. D* **80** (2009) 094003.
- [12] M. Thunman, G. Ingelman, P. Gondolo, *Astropart. Phys.* **5** (1996) 309.
- [13] C. Baus, T. Pierog, R. Ulrich, <http://web.ikp.kit.edu/rulrich/crmc.html> (2014).
- [14] S. Ostapchenko, *EPJ Web Conf.* **52** (2013) 02001.
- [15] T. Pierog *et al.*, (2013) [[arXiv:1306.0121](#)].
- [16] S. Ostapchenko, *Phys. Rev. D* **83** (2011) 014018.
- [17] M. Gyulassy and X.-N. Wang, *Comput. Phys. Commun.* **83** (1994) 307.
- [18] R. Hagedorn, *Rev. del Nuovo Cim.* **6N 10** (1984) 1.
- [19] J. Adams *et al.* (STAR Collaboration), *Phys. Rev. C* **70** (2004) 044901.
- [20] T. Sjöstrand, S. Mrenna, P. Skands, *Comput. Phys. Commun.* **178** (2008) 852-867.
- [21] A. Adare *et al.* (PHENIX Collaboration), *Phys. Rev. C* **81** (2010) 034911.
- [22] V. Khachatryan *et al.* (CMS Collaboration), *JHEP* **02** (2010) 041.
- [23] V. Khachatryan *et al.* (CMS Collaboration), *Phys. Rev. Lett.* **105** (2010) 022002.
- [24] R. Enberg, M. H. Reno and I. Sarcevic, *Phys. Rev. D* **78** (2008) 043005.
- [25] A. Fedynitch *et al.*, in *Proc. of the 18th ISVHECRI* (2014) [[arXiv:1503.00544](#)].
- [26] F. Riehn *et al.*, in *Proc. of the 18th ISVHECRI* (2014) [[arXiv:1502.06353](#)].

## Surface muons in IceTop

---

### The IceCube Collaboration<sup>1</sup>

<sup>1</sup> [http://icecube.wisc.edu/collaboration/authors/icrc15\\_icecube](http://icecube.wisc.edu/collaboration/authors/icrc15_icecube)

*E-mail:* [hdembins@udel.edu](mailto:hdembins@udel.edu)

IceTop, the surface component of the IceCube detector, has been used to measure the energy spectrum of cosmic rays over three decades from 1.6 PeV to 1.3 EeV. It was recently shown that the recorded data can also be used to measure the average density of GeV muons in the shower front at large lateral distances ( $> 300$  m) from the shower axis. The analysis is based on fitting the single muon peak in charge histograms built over many events. The shape of this peak can be accurately modeled and stands out above the electromagnetic background at large distances. Since the analysis can be done in several lateral intervals, we effectively extract the muon lateral distribution function from data ( $\mu$ -LDF). The amplitude of the  $\mu$ -LDF is connected to the average cosmic-ray mass.

We will present the measurement of the  $\mu$ -LDF for cosmic rays with energies between 1 PeV and 30 PeV and compare it to proton and iron simulations. By combining the  $\mu$ -LDF with complementary mass-sensitive observables, like the charge deposited by muon bundles in IceCube, we expect to significantly reduce systematic uncertainties in the inferred cosmic ray mass composition due to theoretical uncertainties in hadronic interaction models.

**Corresponding authors:** H.P. Dembinski\*, J.G. Gonzalez,  
*Bartol Institute, University of Delaware, USA*

*The 34th International Cosmic Ray Conference,  
30 July- 6 August, 2015  
The Hague, The Netherlands*

---

\*Speaker.

## 1. Cosmic rays and muons in air showers

Cosmic rays above 0.1 PeV are detected through air showers generated in Earth's atmosphere, typically with large ground arrays of particle detectors. The origin of PeV cosmic rays is a long standing puzzle. Since cosmic rays are charged, they are bent onto complex paths by galactic and extragalactic magnetic fields [1]. The arrival direction of a cosmic ray can be accurately measured, but it does not point back to the source. The two remaining identifying properties of a cosmic ray are its energy and mass. Knowledge of the energy spectrum and mass composition of cosmic rays does help to discriminate between different origin and propagation scenarios [2], but the inference from air shower data is model-dependent, which is the main obstacle in this approach.

The model-dependence enters through air shower simulations which provide the link between the properties of the incident cosmic rays and the measurement at the ground. These simulations rely on hadronic interaction models, phenomenological interpretations of collider data, extrapolated into phase-space regions relevant for air showers. The uncertainty on how to do the extrapolation is reflected in the variety of available hadronic interaction models [2].

The best strategy under these circumstances is to collect many different experimental observables. A hadronic model can then be tested on its consistency in inferring the mass composition from these observables. If the results differ, this might point to a deficiency in the model.

If separately measured, the muon content of an air shower on the one hand, and its electron and photon content on the other, form a potent pair of variables to infer the energy  $E$  and mass  $A$  of the cosmic ray [2]. Using a Heitler-approximation of a hadronic shower [3], it has been shown that the number of electrons at shower maximum approximately scales like  $E$ , while the muon component scales like  $E^\beta A^{1-\beta}$ , with  $\beta \simeq 0.9$  [4]. The energy  $E$  therefore can be deduced from the size of the electromagnetic component, and the mass  $A$  from the size of the muon component. The model-uncertainty enters through the values of  $\beta$  and the corresponding scaling factors, which have to be taken from simulations.

In this paper, we show a preliminary measurement of the average lateral density function of muons ( $\mu$ -LDF) obtained with IceTop [5], the surface component of the IceCube Neutrino Observatory, between 1 PeV and 30 PeV. The result is an update of the analysis first presented in Ref. [6], which is a statistical study of signals collected at large lateral distances (minimum radius varies between 250 m at 1 PeV and 400 m at 100 PeV). Muon-rich signals at large lateral distances were explored before [7], but the potential to measure the muon density was realized only recently. The analysis presented here yields a high-resolution measurement due to the large exposure collected by IceTop, does not rely on detector simulation, and works over a large zenith angle range from  $0^\circ$  to  $40^\circ$  (an extension to higher angles is under study). It exploits the low trigger threshold in each detector and the fact that GeV muons have a clear signature as through-going minimum-ionizing particles in IceTop detectors.

The average density of muons at a given reference distance scales with the overall average size of the muon component. As outlined above, this implies that the measurement of  $\mu$ -LDF can be converted into an estimate of the mean logarithmic mass [4]. In addition, the measurement of the  $\mu$ -LDF over a large lateral range and zenith angle range provides a wealth of data, which will allow us to test the consistency of a hadronic model. The  $\mu$ -LDF itself will be used in a future event-by-event fit of recorded signals [8]. Our measurement of GeV muons at the surface is complementary

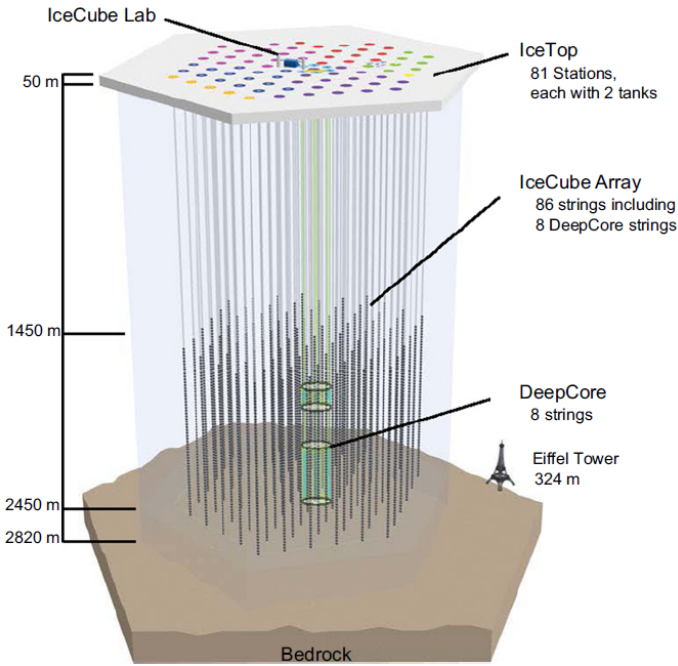


Figure 1: Schematic view of the IceCube experiment. The bulk of the light detectors are buried under 1.5 km of ice and form the in-ice detector. The in-ice detector is used mainly for neutrino astronomy and neutrino physics studies. The IceTop detector is formed by 81 pairs of ice-filled tanks at the surface. They are used to veto particles from cosmic-rays induced air showers that sometimes reach the in-ice detector, and for studies of cosmic rays at the South Pole at 2835 m altitude and an atmospheric depth of about  $680 \text{ g cm}^{-2}$ .

to ongoing analyses of muon bundles that reach IceCube [9], and the analysis of high- $p_T$  muons accompanying these bundles [10]. A related analysis of muon-rich signals in detectors at large lateral distance is ongoing, which studies their sensitivity to the cosmic-ray mass composition [11].

## 2. The IceTop array

The IceTop detector is the surface component of the IceCube Neutrino Observatory, shown in Fig. 1. It consists of 81 stations on a triangular grid with mean spacing of 125 m, covering roughly one square kilometer. Each station consists of two ice-Cherenkov detectors separated by 10 m. The active volume of each detector is a cylinder with a ground area of  $2.54 \text{ m}^2$  and a height of 0.9 m.

The detectors are sensitive to muons ( $E_\mu > 0.2 \text{ GeV}$ ), electrons and photons, but have no dedicated particle identification functionality. They measure the deposited PMT charge  $S$ , the time-integral of a localized pulse above the baseline, in units of VEM (vertical equivalent muon). The VEM is the mean charge generated by a muon passing vertically through the detector, which have a dynamic range of 0.2 to about 1000 VEM. A "Hard Local Coincidence" (HLC) occurs when two detectors from the same station trigger within a time window of  $1 \mu\text{s}$ . A single local trigger without such a partner is called a "Soft Local Coincidence" (SLC).

The difference between HLCs and SLCs for our purpose is that HLC charges are better calibrated. For an HLC, the whole time trace of the pulse is recorded, which allows us to do more sophisticated off-line processing to compute the charge. For an SLC, only the total charge computed by the on-board firmware is recorded. The resolution of SLC charges used in this analysis is improved by performing an off-line cross-calibration to HLC charges. After this correction, the charge resolutions of HLCs and SLCs agree within a few percent.

Air showers are reconstructed by fitting an LDF-model to the recorded charges and a model of the curved shower front to the signal arrival times [5]. The signal  $S_{125}$  at 125 m lateral dis-

tance to the shower axis is used to quantify the size of the shower at ground, and converted into an estimate of the cosmic ray energy using simulated air showers [12]. Up to zenith angles of  $40^\circ$ ,  $S_{125}$  is dominated by the electromagnetic component of the air shower. At large radii,  $r \gtrsim 250 (E/\text{PeV})^{0.25}$  m [6], photons and electrons become less energetic and fewer in number, so that their average contribution to the signal drops below 1 VEM. At this point, the muon component may be identified.

### 3. Data set and analysis

We use IceTop data recorded from 1 June 2010 to 31 May 2013, processed with the standard reconstruction [12]. After standard quality cuts [12], 82 M events remain. We analyze events with zenith angles  $\theta < 40^\circ$  and shower sizes  $S_{125} > 1.0$  VEM, which reduces the number to 47 M events.

The present work is an update of the analysis presented in Ref. [6]. The analysis approach was independently re-implemented from scratch, which allowed us to cross-check both implementations. The update differs from the first version in two key aspects.

Firstly, it addresses a known issue of the first implementation. Some recorded charge pulses do not originate from the air shower, but mimic muon pulses. This uncorrelated background is formed by random coincidences from other particles that hit the detector. The uncorrelated background is a significant distortion at low shower energies, where the muon density in the shower front is very small. In the first version, this contribution was subtracted based on a simple estimate of the background trigger rate, with some systematic uncertainty. In the updated version, the uncorrelated background is explicitly measured as explained below, and subtracted without uncertainty.

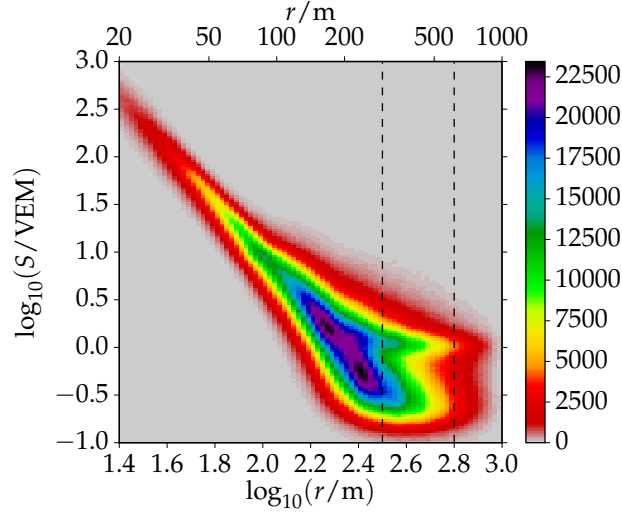
Secondly, the model for the expected charge distribution from pulses with muons was refined. In the first version, the distribution was tabulated from simulations of the detector response to muons. In the update, the tables were replaced by an analytical model of the detector response, whose parameters are completely determined by the data. This avoids uncertainties in the simulation of the muon response.

The analysis procedure is described in the following. For each reconstructed event, we select all recorded pulses compatible in time with the reconstructed shower front, using a window of  $1.5 \mu\text{s}$  (signal window). We measure the contribution of random coincidences by selecting all pulses in an off-time window before the shower front arrives, that has a length of  $8 \mu\text{s}$  (background window). Finally, we also count all detectors that were in data acquisition, whether they had a pulse in the signal window or not. Their number is needed to compute the Poisson probability for having  $k$  muon hits in a detector for a given expectation.

We then generate histograms of the charge  $S$  for the selected pulses. We generate independent histograms for bins of the lateral distance  $r$  to the shower axis, the shower size  $S_{125}$  (which is a proxy of the shower energy), and the shower zenith angle  $\theta$ . Separate sets of histograms are generated for the signal and the background window, and furthermore for HLC and SLC pulses, to take their minor differences in resolution into account.

Two charge histograms are shown in Fig. 2. At large radii, we find two distinct components. The first component peaks around  $S \approx 0.3$  VEM. It consists of detectors which were hit only by low-energy electrons and photons, which contribute a small fraction of a VEM per particle. The





(a) 2D charge histogram (sum of HLC and SLC histograms).

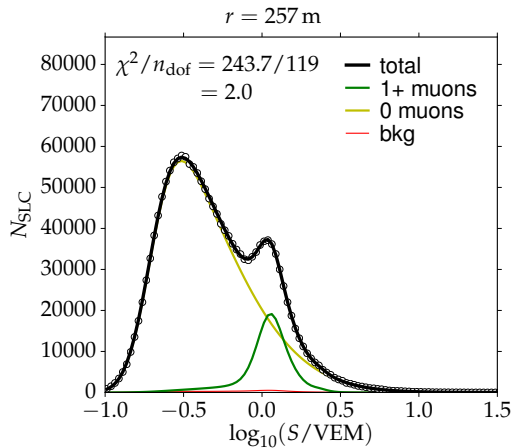
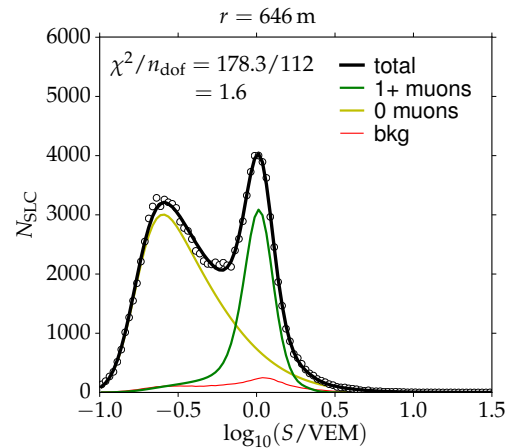
(b) Slice around  $r = 257$  m.(c) Slice around  $r = 646$  m.

Figure 2: Shown are histograms of recorded pulse charges  $S$  for near vertical air showers with  $\langle E \rangle \approx 3$  PeV and  $\langle \theta \rangle \approx 13^\circ$ . a) The dashed lines mark the slices shown in b) and c). Also shown in the slices is the model fitted to the histograms, which we use to compute the muon density per detector (thick black line), and its three components (thin lines). There is a component for hits without muons (0 muons), a component for hits with one or more muons (1+ muons), and the component for hits from uncorrelated background (bkg).

Table 1: Number of fitted parameters per charge histogram.

Model aspect	no. of parameters
signal threshold	2
shape of 0 muon-peak	2
shape of 1+ muon-peak	3
peak amplitudes	2
total	9

second component peaks around 1 VEM, and consists of detectors that were hit by at least one muon.

Our model for the charge distribution generated by muon hits is detailed and relies only on a few basic assumptions. GeV muons are distinct, because they are minimum-ionizing, penetrate the detector without being stopped, and are parallel to the shower axis within a few degrees. Particles that enter the detector through the top and leave through the base generate tracks of equal length. Since the generated Cherenkov-light is proportional to the track length and since the selected showers are close to vertical, the charges generated by muon hits are always very close to 1 VEM. This well-defined feature allows us to distinguish muon hits from other hits on a statistical basis. In principle, there is another peak for two simultaneous muons hits around 2 VEM and so on, but it is not visible in Fig. 2. These peaks are statistically suppressed, because the muon density at large lateral distances from the shower axis is very low. The chance for two simultaneous hits is very small at the radii that we consider. We model the charge distributions for up to three simultaneous muon hits and neglect higher contributions.

Mathematically, the charge distribution for hits with muons is constructed as follows. For a given muon density  $\rho_\mu$ , the expected number of muon hits  $\lambda_\mu$  per detector is computed from the effective area of the detector at the given zenith angle  $\theta$ . The chance for  $k$  simultaneous muon hits is computed from the Poisson distribution with expectation  $\lambda_\mu$ . We compute the charge distribution for  $k = 1$  by folding an analytical model of the track length distribution [13] (parameter free) with an exponentially modified Gaussian kernel [14]. The kernel models the finite detector resolution and the additional charge generated by electrons and photons that accompany the muon. The approach was found to describe the simulated detector response to muons very well. The charge distribution for  $k$  simultaneous muon hits then follows from auto-convolution of the distribution for  $k = 1$ .

The charge distribution for pulses without muons is described empirically by the density  $\sim \exp(a + b \log r + c \log^2 r)$ , and no effort is made to physically interpret it. Both distributions are multiplied with a Gaussian cumulative density function in the logarithm of the signal, which models the reduced efficiency for detecting low signals, caused by the threshold trigger in each detector. This approach statistically accounts for losses of muon signals due to the threshold trigger, so that these losses are automatically corrected. In near-vertical showers, these losses are also small, since the charge in pulses with muons is usually far larger than the threshold level of 0.2 VEM.

The measured charge distribution of random coincidences (uncorrelated background) is finally added on top of these distributions. The sum of all component distributions is fitted to the data using a log-likelihood method, which then extracts the muon density  $\rho_\mu$  for each lateral bin in which the muon peak is separable. The nine parameters (listed in Table 1) of our semi-analytical model are

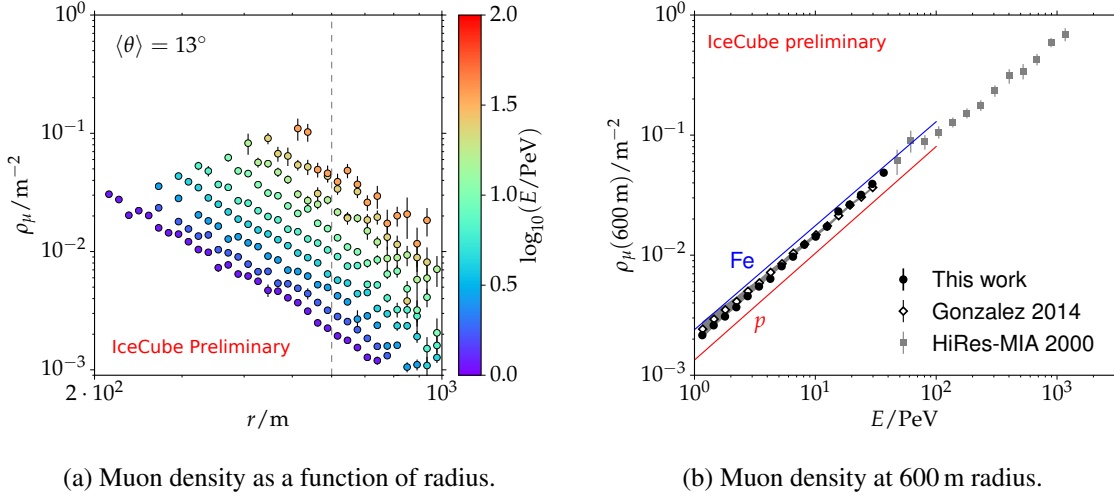


Figure 3: *Left*: Average muon density  $\rho_\mu$  in near-vertical showers ( $\langle\theta\rangle \approx 13^\circ$ , slant depth  $X \approx 700 \text{ g cm}^2$ ) at various energies and lateral distances measured at the South Pole, for one month of data (June 2011). The dashed line indicates the reference radius of 600 m. *Right*: Comparison of  $\rho_\mu(600 \text{ m})$  obtained in this work with the corrected previous result from Gonzalez [6] (see text for details). The gray band represents the systematic uncertainty associated the approximate subtraction of uncorrelated background in the previous analysis. Shown for reference are simulation results for proton and iron showers, generated with CORSIKA, using Sibyll-2.1 and Fluka [15, 16, 17]. Also shown for reference is a measurement from HIRES-Mia in Utah, Colorado [18]. The latter is located at a different slant depth of  $X \approx 860 \text{ g cm}^{-2}$ .

completely determined by data, and fitted independently to each charge histogram.

The effective energy threshold for our method is given by the energy required for muons to fully penetrate the ice volume inside a detector and the snow layer on top of it. The latter varies between 0.1 m and 3 m. The density of snow at the South Pole is about  $0.4 \text{ g cm}^{-3}$  [5], so that we obtain an effective energy threshold of  $(0.16 + 0.08 h_{\text{snow}}[\text{m}]) \text{ GeV} / \cos \theta$  due to ionization losses, where  $h_{\text{snow}}$  is the snow height in meter. The muons that we investigate have typical energies of a few GeV, therefore we do not expect significant losses in near-vertical showers. We will experimentally investigate the impact of the snow layer by comparing detectors in different depths in the future.

#### 4. Preliminary results and outlook

In Fig. 3, we show our preliminary estimate of the average muon density  $\rho_\mu$  in near-vertical air showers between 1 PeV and 30 PeV from one month of data (June 2011). Overlaid are estimates of  $\rho_\mu(600 \text{ m})$  from the first presentation of the analysis [6], which have been modified here to correct a calculation error that was discovered after comparing the two analysis implementations. The error had made our initial estimate of  $\rho_\mu(600 \text{ m})$  by a factor of about 1.5 too high. Both results are in very good agreement after the correction.

The HiRes-MIA and the Pierre Auger collaborations reported muon densities above 50 PeV and 5 EeV respectively [18, 4] which exceeded expectations from all tested hadronic interaction

models. In Fig. 3, we compared our estimate with CORSIKA simulations for proton and iron showers using the hadronic interaction models Sibyll-2.1 and Fluka [15, 16, 17]. The simulations bracket our data. We will follow up on this investigation by comparing to more hadronic interaction models, once our results are final.

The next step towards finalizing the analysis is to perform a check of our approach based on an analysis of fully detector-simulated air showers. We want to determine how well our fits of charge histograms estimate the true muon density in CORSIKA showers, computed from the muon hits at the ground. We will also investigate the effect of snow on top of detectors and possible variations of the measured muon density over time.

A future publication of our results will contain the  $\mu$ -LDF measured over a wider range of shower energies and zenith angles, together with suitable parametrizations of the data. This will allow us to make several interpretations: The muon density  $\rho_\mu$  at 600 m scales with the size of the muon component of an air shower, while the standard energy proxy of IceTop, the signal  $S_{125}$  at 125 m scales primarily with the electromagnetic component. Following the analysis outlined in the introduction, and recently applied in Ref. [4], we will transform these two measurements into an estimate of the mean logarithmic mass  $\langle \ln A \rangle$  of cosmic rays using Sibyll-2.1 and more recent hadronic interaction models. In addition, we will investigate the muon attenuation with zenith angle. The muon attenuation is also sensitive to the mass composition and allows us to test the internal consistency of a hadronic interaction model, since it has to predict both the size and the attenuation of the muon component in agreement with our data.

## References

- [1] R. Jansson and G.R. Farrar, *Astrophys. J.* **757** (2012) 14.
- [2] K.-H. Kampert, M. Unger, *Astropart. Phys.* **35** (2012) 660.
- [3] J. Matthews, *Astropart. Phys.* **22** (2005) 387.
- [4] **Pierre Auger** Collaboration, A. Aab et al., *Phys. Rev. D* **91** (2015) 032003.
- [5] **IceCube** Collaboration, R. Abbasi et al., *Nucl. Instrum. Meth. A* **700** (2013) 188.
- [6] **IceCube** Collaboration, J.G. Gonzalez et al., *Measuring the Muon Content of Air Showers with IceTop*, in *Proc. ISVHECRI 2014*, CERN, Switzerland (2014), [arXiv:1501.03415].
- [7] M. Vraeghe, Master thesis: *Muon Counting with the IceTop Detector as Probe of Cosmic Ray Composition*, Gent University, Belgium (2012).
- [8] **IceCube** Collaboration, J.G. Gonzalez et al., *PoS(ICRC2015)338 these proceedings* (2015).
- [9] **IceCube** Collaboration, K. Rawlins et al., *PoS(ICRC2015)628 these proceedings* (2015).
- [10] **IceCube** Collaboration, D. Soldin et al., *PoS(ICRC2015)256 these proceedings* (2015).
- [11] D. Bindig, PhD thesis in preparation: *Measuring muons in IceTop*, Wuppertal University, Germany (2015).
- [12] **IceCube** Collaboration, M.G. Aartsen et al., *Phys.Rev. D* **88** (2013) 042004.
- [13] B. Kégl and D. Veberič, *Pierre Auger Observatory note GAP-2009-043* (2009), [arXiv:1502.03347].
- [14] E. Grushka, *Analytical Chemistry* **44** (1972) 1733.
- [15] D. Heck, G. Schatz, T. Thouw, J. Knapp, and J. N. Capdevielle, *Report No. FZKA 6019* (1998).
- [16] R.S. Fletcher, T.K. Gaisser, P. Lipari, T. Stanev, *Phys. Rev. D* **50** (1994) 5710; in *Proc. 26th Int. Cosm. Ray Conf., vol. 1*, Salt Lake City, USA (1999) 415.
- [17] A. Ferrari, P.R. Sala, A. Fassò, and J. Ranft, *CERN-2005-10* (2005), *INFN/TC\_05/11, SLAC-R-773*.
- [18] **HiRes-MIA** Collaboration, T. Abu-Zayyad et al., *Phys. Rev. Lett.* **84** (2000) 4276.

# Anisotropy in Cosmic-Ray Arrival Directions Using IceCube and IceTop

---

## The IceCube Collaboration<sup>†</sup>

<sup>†</sup>[http://icecube.wisc.edu/collaboration/authors/icrc15\\_icecube](http://icecube.wisc.edu/collaboration/authors/icrc15_icecube)

E-mail: [westerhoff@physics.wisc.edu](mailto:westerhoff@physics.wisc.edu)

The IceCube Neutrino Observatory recorded more than 250 billion cosmic-ray induced muon events between May 2009 and May 2014. We use this data set to study the anisotropy in the arrival direction distribution of cosmic rays in the TeV to PeV energy range. The anisotropy features large regions of relative excess and deficit with amplitude on the order of  $10^{-3}$ . A decomposition of the arrival direction distribution into spherical harmonics shows that most of the power is contained in the low-multipole ( $\ell \leq 4$ ) moments. However, higher multipole components are also statistically significant down to an angular scale of less than  $10^\circ$ . The data set also allows for a detailed study of the anisotropy for various cosmic-ray median energies. The large-scale structure observed at energies near 20 TeV reaches a minimum amplitude, accompanied by a change in phase, around 150 TeV. At higher energies, we observe a strong deficit with an amplitude increasing with energy up to 5 PeV, the highest energies currently accessible to IceCube. The deficit is also present in IceTop maps of similar energies. No time-dependence of the large-scale structure was observed in the five-year period covered by this analysis.

**Corresponding authors:** F.T. McNally<sup>1</sup>, P. Desiati<sup>1</sup>, and S. Westerhoff<sup>\*,1</sup>

<sup>1</sup>*Wisconsin IceCube Particle Astrophysics Center (WIPAC) and Department of Physics, University of Wisconsin–Madison, Madison, WI 53706, USA*

*The 34th International Cosmic Ray Conference,  
30 July-6 August, 2015  
The Hague, The Netherlands*

---

\*Speaker.

## 1. Introduction

Galactic magnetic fields sufficiently scramble the arrival directions of cosmic rays with TeV energies to prohibit any direct identification of sources based on their arrival direction distribution. However, cosmic rays at this energy propagate diffusively through the Galaxy, and their distribution in the sky shows a degree of anisotropy at the per-mille level that might give some indications of the location of nearby sources and the process of propagating from their sources to us.

Measurements of anisotropy in the arrival direction distribution of TeV cosmic rays have been published by a number of experiments, including the Tibet AS $\gamma$  [1], Super-Kamiokande [2, 3], Milagro [4, 5], EAS-TOP [6], MINOS [7], ARGO-YBJ [8], and HAWC [9] experiments in the Northern Hemisphere and IceCube [10, 11, 12] and its surface air shower array IceTop [13] in the Southern Hemisphere.

In both hemispheres, the observed anisotropy has two main features: a large-scale structure with an amplitude of about  $10^{-3}$  usually fitted as a dipole or a sum of low-order multipoles, and a small-scale structure with a few localized regions of cosmic-ray excesses and deficits of angular size  $10^\circ$  to  $30^\circ$ . The large-scale structure is usually interpreted as a result of diffusive propagation, with the maximum of the dipole possibly pointing in the direction of one or several nearby sources (see for example [14]). On the other hand, the misalignment between the cosmic-ray density gradient and the regular Galactic magnetic field would prevent pointing to any specific source, although it would suppress the anisotropy amplitude to a value closer to what is observed [15]. The small-scale structure is more difficult to explain. It could be the product of turbulence in the Galactic magnetic field [16, 17], among other explanations.

The IceCube detector at the geographic South Pole is currently the only detector that can study cosmic-ray anisotropy in the Southern Hemisphere. Based on data taken with partial detector configurations while the detector was still under construction, we have previously published observations of cosmic-ray anisotropy with IceCube [10, 11] and IceTop [13], as well as studies of the energy dependence of the anisotropy [12]. In this paper, we update the previous results using all of the currently available data, collected in 1690 days of livetime between May 2009 and May 2014. During this period, IceCube recorded about 250 billion events and IceTop recorded 170 million events.

## 2. The Data Set

IceCube is a cubic-kilometer neutrino detector installed in the ice at the geographic South Pole [18]. High-energy neutrinos are detected by observing the Cherenkov radiation from charged particles produced by neutrino interactions in the ice or in the bedrock below the detector. The Cherenkov light is detected by an array of 5160 digital optical modules (DOMs) deployed at depths between 1450 m and 2450 m below the surface of the ice sheet. Each DOM is a pressure-resistant glass sphere that contains a 10-inch photomultiplier tube (PMT) and electronics to digitize the signals. The DOMs are attached to 86 vertical strings separated by an average distance of 125 m, each string hosting 60 DOMs equally spaced over the kilometer of instrumented length.

The IceTop air-shower array is located on the surface of the ice sheet above the IceCube neutrino detector [19]. An integral part of IceCube, IceTop is a dedicated cosmic-ray detector

optimized for air-shower observations at PeV energies. It consists of 81 surface stations, with two light-tight tanks per station. Each tank measures 1.8 m in diameter, is filled with highly transparent ice of 0.9 m in height, and contains two DOMs with different gains.

Both the neutrino detector buried deep in the ice and the cosmic-ray shower detector on the surface can be used to study cosmic-ray arrival direction anisotropy. The in-ice component detects cosmic rays through the relativistic muons produced by cosmic-ray air showers. The trigger rate for events with eight or more DOMs in coincidence (see [20] for details) varies between 2 kHz and 2.4 kHz, with the modulation caused by seasonal variations of the stratospheric temperature [21]. The detected muon events are generated by primary cosmic-ray particles with median energy of 20 TeV, as determined by simulations. The air-shower muons preserve the arrival direction of the primary cosmic ray to within about  $0.2^\circ$ . Because of the high trigger rate and the limited data transfer bandwidth available from the South Pole, all cosmic-ray data are stored in a compact data storage and transfer (DST) format, containing only the results of a fast angular reconstruction and some limited information per event. The median angular resolution for this data set, as determined by simulation, is  $3^\circ$ . The DST data format does not contain event-by-event errors on the arrival direction reconstruction.

The IceTop air-shower array detects cosmic rays at a rate of approximately 30 Hz with a minimum primary particle energy threshold of about 400 TeV. IceTop is sensitive to the electromagnetic component of the shower, not just the muonic component. Due to transmission bandwidth limitations, IceTop data is subject to prescaling. The prescaling factor depends on the event size and has changed over time with the detector configuration. Only events that trigger eight or more stations have not been prescaled for any configuration, so to obtain a consistent data set for the entire period covered by this analysis, we used only this subset of showers. The resulting data set has a median energy of 1.7 PeV.

In the first two years used in this analysis, IceCube and IceTop operated in partial detector configurations, with 59 active strings/stations (IC59/IT59) from May 2009 to May 2010, and 79/73 strings/stations (IC79/IT73) from May 2010 to May 2011. Since May 2011, the detector has been operating in its full configuration (IC86/IT81).

### 3. Large- and Small-Scale Structure

Several steps are necessary to produce sky maps of the large- and small-scale cosmic-ray anisotropy. For our analysis, we implemented an equal-area binning of the sky using the HEALPix library [22]. The underlying resolution is about  $1^\circ$ , but the final maps are smoothed on angular scales corresponding to the resolution of the detector.

The first step in the study of anisotropy in cosmic-ray arrival directions is the creation of a reference map showing the response of the detector to an isotropic flux of cosmic rays. The reference map itself is not isotropic, as it accounts for changes in the cosmic-ray rate from atmospheric effects, occasional detector downtime, and effects from the detector geometry. The reference map is generated from the data themselves. For each event in the data map, events in the reference map are created by attaching the same arrival direction in local coordinates to randomly selected arrival times from the distribution of real arrival times within a time window of 24 hours. The technique is described in detail in [11]. We note that this technique only modifies the right ascension of the

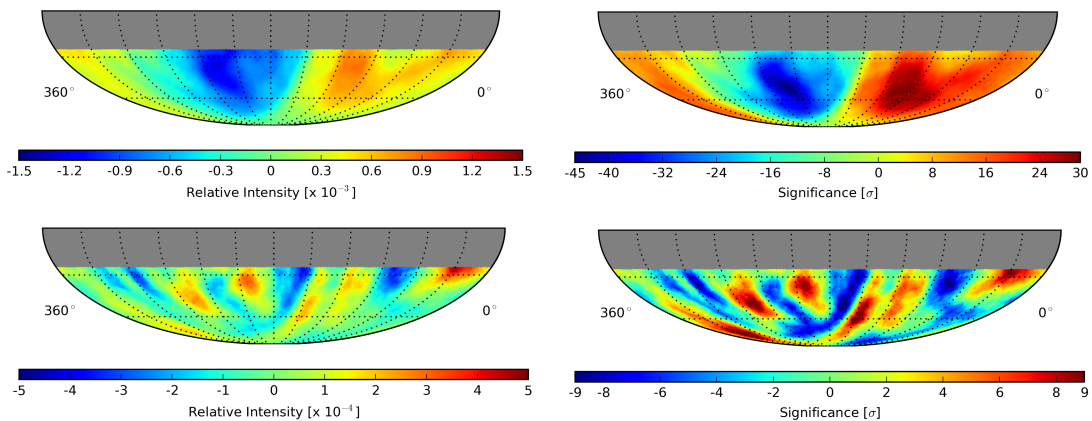


**Figure 1:** Equatorial maps of the relative intensity of the cosmic-ray flux (*left*) and the pre-trial statistical significance of the deviation from isotropy (*right*) before (*top*) and after (*bottom*) dipole and quadrupole subtraction. An angular smoothing with  $5^\circ$  radius is applied to all maps.

event within the same declination band. Consequently, any large-scale structure in the arrival direction distribution is reduced to its projection onto the equatorial plane. However, simulations show that localized (small-scale) structures are correctly reproduced with this method.

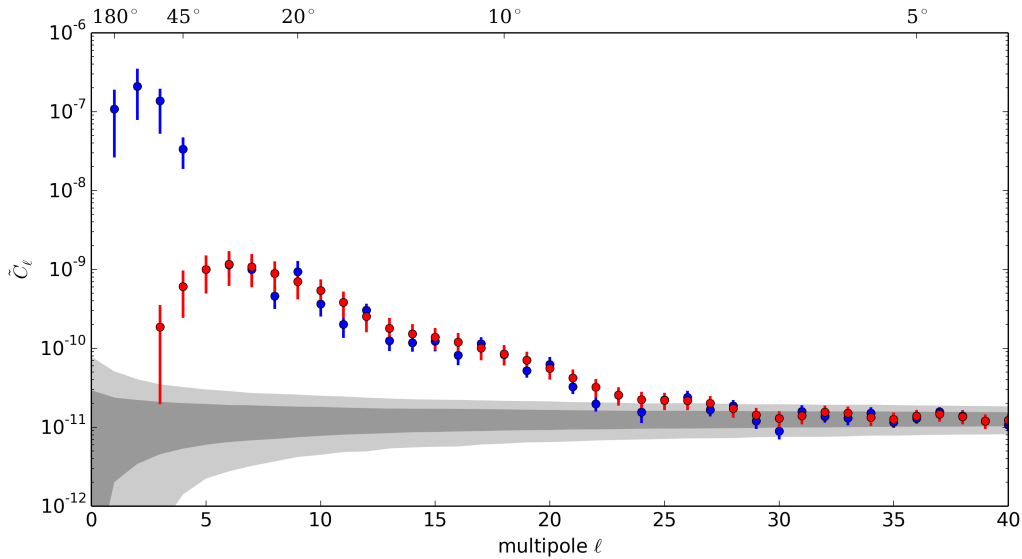
In the second step, the reference map is compared to the data map to obtain a sky map that shows the deviations from isotropy. Typically, these maps show the relative intensity of the cosmic-ray flux,  $\delta I_i = (N_i - \langle N \rangle_i) / \langle N \rangle_i$ , where  $N_i$  and  $\langle N \rangle_i$  are the number of observed events and the number of reference events in the  $i^{\text{th}}$  bin of the map, respectively. To evaluate the statistical significance of any deviation from isotropy, we also produce maps of significance calculated according to Li & Ma [23]. A top-hat smoothing procedure in which a single pixel's value is the sum of all pixels within a  $5^\circ$  radius has been applied to all maps.

Figure 1 (top) shows, in equatorial coordinates, the sky map of relative intensity (left) and statistical significance (right) for five years of IceCube data. No energy cuts have been applied for these maps, so the median energy of the cosmic-ray primaries is 20 TeV. The maps are dominated by large-scale structure, with a deep deficit from  $150^\circ$  to  $250^\circ$  in right ascension and a corresponding excess from  $30^\circ$  to  $120^\circ$ . The distribution is, however, not well described by a dipole or even a sum of the first low-order multipole moments (dipole, quadrupole, ...) of the spherical harmonic function, indicating the presence of structure at smaller angular scales. To study this small-scale anisotropy, the dominating large-scale structure has to be removed. To achieve this, the dipole and quadrupole terms are fit to the relative intensity map and then subtracted.

The bottom panels of Figure 1 show maps of relative intensity (left) and statistical significance (right) after the subtraction of the best-fit dipole and quadrupole terms. The regions of excess and deficit in cosmic-ray flux are similar to those shown in previous work [11], but the increased statistics of the five-year data set increases the significance of the features and leads to a better resolution of the small-scale structure. The maps clearly indicate statistically significant anisotropy down to angular scales approaching the angular resolution of the detector.

Figure 2 shows the angular power spectrum of the five-year data set both before (blue) and after (red) the subtraction of the dipole and quadrupole moments. It confirms the presence of significant





**Figure 2:** Angular power spectrum for five years of IceCube data (*blue*) and for the same date with best-fit dipole and quadrupole moments subtracted (*red*). The amplitudes  $C_\ell$  for  $\ell = 1, 2$  are consistent with 0 after the subtraction. Dark- and light-gray bands represent the power spectra for isotropic sky maps at the 68% and 90% confidence levels, respectively.

structure up to multipoles  $\ell \simeq 20$ , corresponding to angular scales of less than  $10^\circ$ .

#### 4. Energy Dependence

Studies of the arrival direction anisotropy between TeV and PeV energies have revealed a substantial change in the amplitude and phase of the best-fit dipole with energy [6, 12]. To analyze the energy dependence, we split the data set into nine bins with increasing median energy based on the number of DOMs that collected Cherenkov light and the reconstructed zenith angle (see [12] for details). The energy resolution is poor (on the order of  $0.5 \log(E/\text{GeV})$ ) because muons transport to the surface a small fraction of the total shower energy, with relatively large fluctuations. Therefore, events in each bin have a wide energy distribution and the distributions of the different energy bins overlap substantially. However, the data in the nine energy bins are statistically independent.

Figure 3 shows the dipole amplitude (left) and phase (right) as a function of energy. To obtain these values, we first produce a projection of the relative intensity onto right ascension and then perform a one-dimensional fit of the full set of harmonic functions to the projection. We fit this projection rather than the full sky map because the two-dimensional fit of spherical harmonics to the map is difficult to perform with a limited field of view. As a result of the method we applied to generate the reference map, the sky map will in any case only show the projection of any dipole component, so the one-dimensional fit is sufficient to study the energy dependence of the dominant dipole. The figure shows that a rapid shift of phase by almost  $180^\circ$  occurs at an energy between 130 TeV and 240 TeV. The dipole amplitude decreases with energy up to these energies, and increases again at higher energies. The red data point in Figure 3 is based on IceTop data with a median energy of 1.7 PeV. While the phase agrees well with that found in IceCube data at similar

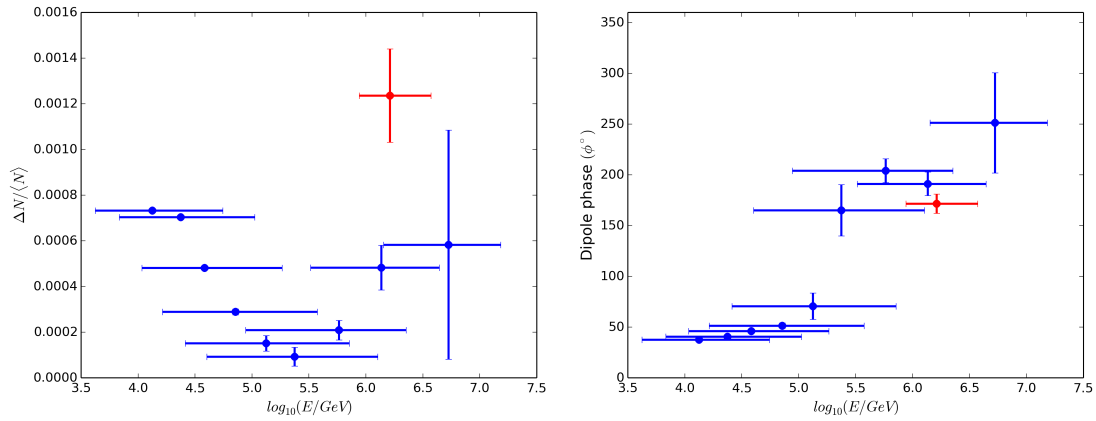


**Figure 3:** Amplitude (*left*) and  $\phi$ -component of phase (*right*) of dipole fit to IceCube (*blue*) and IceTop (*red*) sky maps for various energy bins. Data points indicate the median energy of each energy bin, with error bars showing the 68% containment interval.

energies, the amplitude of the anisotropy is larger in IceTop than in any IceCube energy bin. This could indicate a difference in the energy distribution and the chemical composition of IceCube and IceTop events and is currently under study.

## 5. Time Dependence

The data used in this analysis accumulated over a period of five years and therefore also allows for a study of the stability of the anisotropy over this time period. Such studies have been performed by other experiments, with contradictory results. Both the Tibet [24] and ARGO-YBJ experiments [8] have observed no significant variation in the anisotropy, whereas Milagro [5] reports a steady increase in the amplitude of the deficit region over a period of seven years (2000-2007). The discovery of time modulation in the shape of the anisotropy, in particular a variation with the 11-year solar cycle, could be evidence for a heliospheric influence on the arrival directions.

Figure 4 shows the one-dimensional projection of the relative intensity onto right ascension for each year of IceCube data. Systematic errors are estimated by calculating the maximum amplitude of the signal in the anti-sidereal time frame (see [11] for details). A  $\chi^2$ -test shows that within errors, the large-scale anisotropy is stable over the five years of IceCube data. This is in agreement with the results of a study of the stability over a period of 12 years (2000-2012) using data recorded with the AMANDA and IceCube detector [25].

## 6. Summary and Outlook

The analysis of five years of data taken with the IceCube detector and its air-shower array IceTop show an energy-dependent anisotropy in the arrival direction distribution of TeV to PeV cosmic rays in the Southern Hemisphere. In addition to a large-scale structure, we observe significant small-scale structure down to scales approaching the angular resolution of the detector. The phase of the large-scale anisotropy changes rapidly between 130 TeV and 240 TeV. During the time period analyzed, the large-scale structure is stable with time.

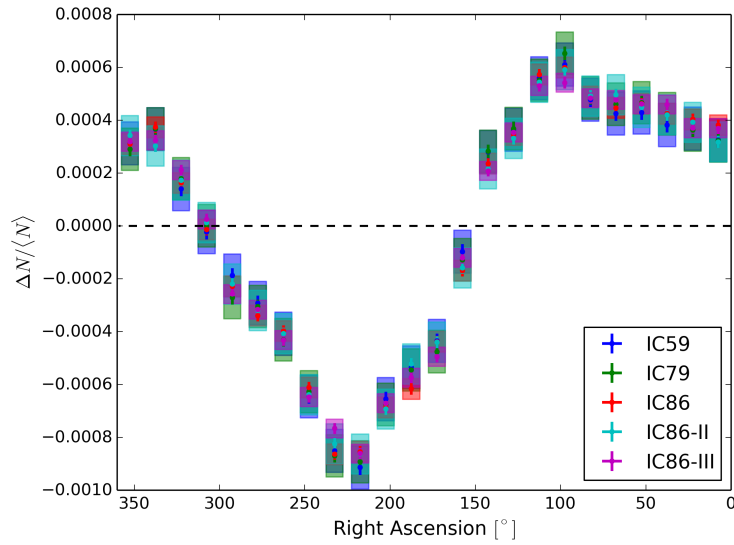


**Figure 4:** Relative intensity of the cosmic-ray flux as a function of right ascension for each configuration of the IceCube detector from IC59 to the third year of IC86. The plot is a one-dimensional projection of the sky map onto the right ascension axis. Systematic errors are calculated using the anti-sidereal frame for each year independently.

Due to the high data rate, the event-by-event information stored for the muon tracks in the in-ice detector is limited and does not allow for a more detailed analysis of the anisotropy. For data taken with the IceTop air-shower array, a more accurate energy reconstruction is available, and it is possible to study the energy spectrum of excess and deficit regions and a possible dependence of the anisotropy on the chemical composition of the primary cosmic-ray flux. Studies with detectors in the Northern Hemisphere have shown that the energy spectrum of the cosmic-ray flux in the most dominant excess regions is harder than the isotropic cosmic-ray flux [4, 8, 9]. In the near future, we plan to use IceTop data to search for similar effects in the southern sky.

## References

- [1] **Tibet AS $\gamma$**  Collaboration, M. Amenomori et al., *Large-Scale Sidereal Anisotropy of Galactic Cosmic-Ray Intensity Observed by the Tibet Air Shower Array*, *Astrophys. J.* **626** (2005) L29.
- [2] **Kamiokande** Collaboration, K. Munakata et al., *Large-Scale Anisotropy of the Cosmic-Ray Muon Flux in Kamiokande*, *Phys. Rev. D* **56** (1997) 23.
- [3] **Super-Kamiokande** Collaboration, G. Guillian et al., *Observation of the Anisotropy of 10 TeV Primary Cosmic Ray Nuclei Flux with the Super-Kamiokande-I Detector*, *Phys. Rev. D* **75** (2007) 062003.
- [4] **Milagro** Collaboration, A.A. Abdo et al., *Discovery of Localized Regions of Excess 10-TeV Cosmic Rays*, *Phys. Rev. Lett.* **101** (2008) 221101.
- [5] **Milagro** Collaboration, A.A. Abdo et al., *The Large-Scale Cosmic-Ray Anisotropy as Observed with Milagro*, *Astrophys. J.* **698** 2121 2009.
- [6] **EAS-TOP** Collaboration, M. Aglietta et al., *Evolution of the Cosmic-Ray Anisotropy Above  $10^{14}$  eV*, *Astrophys. J.* **692** (2009) L130.

- [7] **MINOS** Collaboration, J.K. deJong et al., *Observations of Large Scale Sidereal Anisotropy in 1 and 11 TeV Cosmic Rays from the MINOS Experiment*, Proc. 32nd ICRC, Beijing, China (2011) [arXiv:1201.2621].
- [8] **ARGO-YBJ** Collaboration, B. Bartoli et al., *Medium Scale Anisotropy in the TeV Cosmic Ray Flux Observed by ARGO-YBJ*, Phys. Rev. D **88** (2013) 082001.
- [9] **HAWC** Collaboration, A.U. Abeysekara et al., *Observation of Small-Scale Anisotropy in the Arrival Direction Distribution of TeV Cosmic Rays with HAWC*, Astrophys. J. **796** (2014) 108.
- [10] **IceCube** Collaboration, R.U. Abbasi et al., *Measurement of the Anisotropy of Cosmic-Ray Arrival Directions with IceCube*, Astrophys. J. **718** (2010) L194.
- [11] **IceCube** Collaboration, R.U. Abbasi et al., *Observation of Anisotropy in the Arrival Directions of Galactic Cosmic Rays at Multiple Angular Scales with IceCube*, Astrophys. J. **740** (2011) 16.
- [12] **IceCube** Collaboration, R.U. Abbasi et al., *Observation of Anisotropy in the Galactic Cosmic-Ray Arrival Directions at 400 TeV with IceCube*, Astrophys. J. **746** (2012) 33.
- [13] **IceCube** Collaboration, M.G. Aartsen et al., *Observation of Cosmic-Ray Anisotropy with the IceTop Air Shower Array*, Astrophys. J. **765** (2013) 55.
- [14] A.D. Erlykin and A.W. Wolfendale, *The Anisotropy of Galactic Cosmic Rays as a Product of Stochastic Supernova Explosions*, Astropart. Phys. **25** (2006) 183.
- [15] P. Mertsch and S. Funk, *Solution to the Cosmic Ray Anisotropy Problem*, Phys. Rev. Lett. **114** (2015) 021101.
- [16] G. Giacinti and G. Sigl, *Local Magnetic Turbulence and TeV-PeV Cosmic Ray Anisotropies*, Phys. Rev. Lett. **109** (2012) 071101.
- [17] M. Ahlers, *Anomalous Anisotropies of Cosmic Rays from Turbulent Magnetic Fields*, Phys. Rev. Lett. **112** (2014) 021101.
- [18] **IceCube** Collaboration, A. Achterberg et al., *First Year Performance of the IceCube Neutrino Telescope*, Astropart. Phys. **26** (2006) 155.
- [19] **IceCube** Collaboration, R.U. Abbasi et al., *IceTop: The Surface Component of IceCube*, Nucl. Instr. Meth. A **700** (2013) 188.
- [20] J.L. Kelley for the **IceCube** Collaboration, *Event Triggering in the IceCube Data Acquisition System*, AIP Conference Proceedings **1630** (2014) 154.
- [21] **IceCube** Collaboration, R.U. Abbasi et al., *Seasonal Variations of High Energy Cosmic Ray Muons Observed by the IceCube Observatory as a Probe of Kaon/Pion Ratio*, Proc. 32nd ICRC, Beijing, China (2011) [arXiv:1111.2735].
- [22] K.M. Górski et al., *HEALPix - a Framework for High Resolution Discretization, and Fast Analysis of Data Distributed on the Sphere*, Astrophys. J. **622** (2005) 759.
- [23] T.P. Li and Y.Q. Ma, *Analysis Methods for Results in Gamma-Ray Astronomy*, Astrophys. J. **272** (1983) 317.
- [24] **Tibet AS $\gamma$**  Collaboration, M. Amenomori et al., *On Temporal Variations of the Multi-TeV Cosmic Ray Anisotropy Using the Tibet III Air Shower Array*, Astrophys. J. **711** (2010) 119.
- [25] **IceCube** Collaboration, M.G. Aartsen et al., *Study of the Time-Dependence of the Cosmic-Ray Anisotropy with AMANDA and IceCube*, Proc. 33rd ICRC, Rio de Janeiro, Brazil (2013) [arXiv:1309.7006].

# Latest Results on Cosmic Ray Spectrum and Composition from Three Years of IceTop and IceCube

---

**The IceCube Collaboration<sup>1</sup>, T. Feusels<sup>2</sup>**

<sup>1</sup> [http://icecube.wisc.edu/collaboration/authors/icrc15\\_icecube](http://icecube.wisc.edu/collaboration/authors/icrc15_icecube)

<sup>2</sup> *University of British Columbia, Department of Physics and Astronomy*

*E-mail:* [krawlins@uaa.alaska.edu](mailto:krawlins@uaa.alaska.edu)

With the IceTop detector at the South Pole, a spectrum of cosmic ray air shower size  $S_{125}$  can be unfolded into an energy spectrum of primary cosmic rays. When the IceTop data is analyzed in coincidence with high-energy muon energy loss information from the deep IceCube detector, both the spectrum and mass composition of primary cosmic rays can be extracted using a neural network. Both of these analyses have been applied to three years of IceTop and IceCube data: from mid-2010 to mid-2013, using the 73-station/79-string and 81-station/86-string detector configurations. Both analyses are now sensitive to energies from  $2.5 \times 10^{15}$  eV to  $1.2 \times 10^{18}$  eV. The performance and relative advantages of the two analyses will be discussed, and both all-particle spectra as well as individual spectra for elemental groups will be presented.

**Corresponding authors:** K. Rawlins<sup>†\*</sup>

<sup>†</sup> *University of Alaska Anchorage, Department of Physics and Astronomy*

*The 34th International Cosmic Ray Conference,  
30 July- 6 August, 2015  
The Hague, The Netherlands*

---

\*Speaker.

## 1. Introduction

The IceCube Observatory consists of both a surface component and a deeply-buried component. The “in-ice” neutrino telescope (described in detail in [1]) consists of 5160 Digital Optical Modules (DOMs) arranged on 86 strings at 1450-2450m depths in 1 km<sup>3</sup> volume of Antarctic ice. The surface array “IceTop” (described in detail in [2]) consists of 162 ice Cherenkov tanks containing two DOMs arranged as 81 stations, covering an area of 1 km<sup>2</sup>. This work will focus on *two* analyses: an *IceTop-alone* analysis to measure the all-particle cosmic ray energy spectrum, and an *IceTop-IceCube coincidence* analysis which can measure both the spectrum and composition.

In [3], one year of data from the 73-station IceTop detector (IT73) alone was analyzed using shower size as a proxy for primary energy, and measured a spectrum from a few PeV to 1 EeV. With coincidence events, surface observables from IceTop can be combined with muon bundle energy loss observables from the in-ice detector. In [4], one month of 40-station/40-string coincidence data was used to measure a spectrum and average log mass  $\langle \log A \rangle$  from 1 to 30 PeV; an improved analysis was performed in [5, 6] using one year of 73-station/79-string (IT73-IC79) data, achieving better resolution and reaching to 1 EeV. In this work, both analyses are extended to 3 years of data.

## 2. Data and Reconstruction

### 2.1 The 3-year Dataset

The analyses described here use the same dataset: from June 1, 2010, until May 2, 2013, with a total livetime of 977.6 days. The first year of this data was taken in IceCube’s IT73-IC79 configuration. For the second and third years, IceCube was running in its complete configuration of 81 stations and 86 strings. In order to analyze the three years together and compare to Monte Carlo simulations of the IT73-IC79 configuration, the IT81-IC86 data was “retriggered” to the slightly smaller IT73-IC79 configuration.

### 2.2 Reconstructions

Data from IceTop tanks are put through a reconstruction procedure which has been described in detail in [2]. For each event, the best-fit shower core position  $(x_c, y_c, z_c)$  and direction  $(\theta, \phi)$  is found, as well as two parameters describing the shape of the lateral distribution function (LDF) of deposited charge  $(S_{125}, \beta)$ .  $S_{125}$  is the signal strength measured in vertical equivalent muons (VEM) at a reference distance of 125 meters, which is the average distance between stations. This shower size parameter is a proxy for primary energy with only minor composition sensitivity, as shown in Figure 1(left).  $\beta$  is related to the slope of the LDF.

Signals in the surface detectors are attenuated by snow, which accumulates unevenly over the array over time. The reconstruction accounts for snow attenuation through a simple exponential reduction applied to the expected charge, which depends only on the slant depth of snow overburden for the tank, and an “effective attenuation length”  $\lambda$ . As the snow load increases from year to year, the total signals in IceTop become on average more muonic, and  $\lambda$  (which describes the effective attenuation of the *total* signal) is expected to change. So, each of the three years was optimized separately to find the  $\lambda$  which best creates agreement in the  $S_{125}$  spectrum across different regions

in the array with different snow coverages. These best values of  $\lambda$  are: 2.1 meters for 2010/11, 2.25 meters for 2011/12, and 2.25 meters for 2012/13.

In the coincidence analysis, the energy loss pattern of the high-energy muon bundles in the IceCube strings is reconstructed using a technique discussed in detail in [7]. For each event, a detector response matrix is obtained from tables derived from simulations and parametrized using spline-fits. Inverting the detector response matrix allows the energy loss profile as a function of slant depth to be determined from the pattern of hits.

The energy loss profile is then fit, to extract a) the average energy loss behavior and b) the size and quantity of deviations from that average behavior due to stochastic losses (the ‘‘stochastics’’). The energy loss  $dE_\mu/dX$  at a fixed slant depth of  $X=1500$  m, which corresponds roughly to the top of the IceCube detector, is a highly composition sensitive observable, as shown in Figure 1(right).

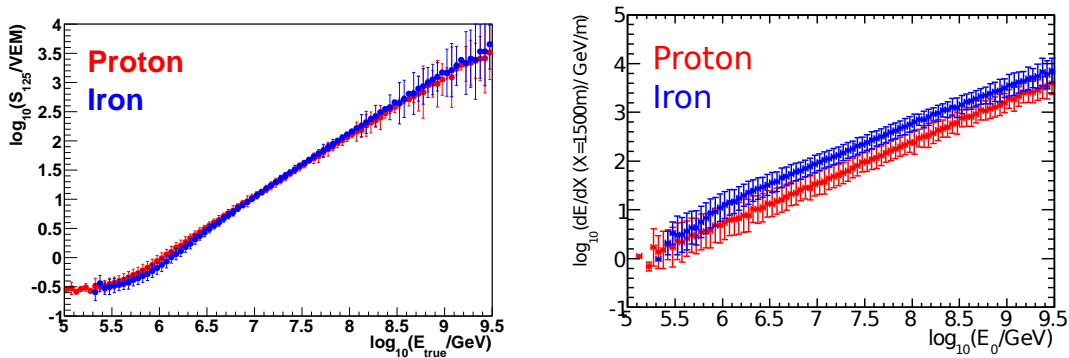


**Figure 1:** Left:  $S_{125}$  as a function of primary energy, which has minimal sensitivity to composition. Right:  $dE_\mu/dX$  at 1500 m as a function of primary energy, which is highly composition-sensitive.

The number of high-energy stochastics is also composition-sensitive. Iron bundles have more stochastics because the bundles contain more muons, despite that the energy losses from proton bundles can be more extreme. Two methods of selecting a number of high-energy stochastics from an energy loss profile are used in this work: a *standard selection* and a *strong selection* requiring higher stochastic energy loss. The standard stochastics count is composition sensitive at low energies. Above 100 PeV where the standard selection loses sensitivity, the strong selection becomes sensitive.

Changes in atmospheric temperature from summer to winter produce a measured variation in  $\log_{10}(dE_\mu/dX)$ . The magnitude of the variation is 10-15% of the difference between protons and iron in Figure 1(right). Simulations represent one atmosphere (from July, 1997), and all other months of data are corrected with respect to July, using a measured relationship between the temperature profile of the entire atmosphere, the muon production depth profile, and the measured variation of  $\log_{10}(dE_\mu/dX)$ . Applying this correction reduces the variation to  $\pm 3\%$  of the difference between protons and iron. For more details, see [15].

### 2.3 Quality Cuts

The IceTop quality cuts for the IceTop-alone and Coincidence analyses were unified, based

on the cuts described in [3] and [5, 6], requiring 5 hit stations, a converged reconstruction, and a slope parameter  $\beta$  between 1.4 and 9.5. To remove uncontained events, the “loudest” station must not be on the edge, and must have a charge of at least 6 VEM. Because the coincidence analysis is very sensitive to contamination from uncontained events and other rare outliers, some additional quality cuts are applied on the surface events. Additionally for coincidences, the track position and direction (determined by IceTop), is required to pass within 0.96 of the volume of the in-ice detector perimeter, and several additional cuts ensure the quality of the energy loss fit. In both analyses, the reconstructed core position is required to be contained within IceTop.

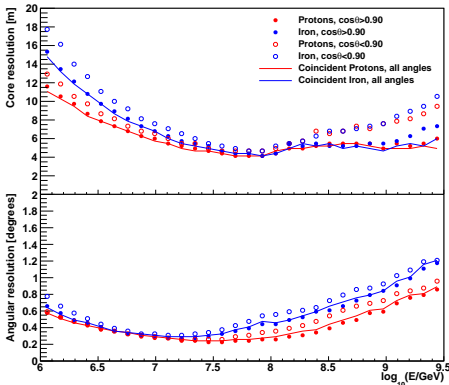


**Figure 2:** Core position resolution (upper) and angular resolution (lower) of the reconstructed air shower after quality cuts, as a function of primary energy. Defined as containing 68% of the events.

systematics studies. The IceTop tank simulation is performed by a detailed Geant4 [12] model, and the triggers and readout electronics are also simulated.

Additionally, for the Coincidence analysis, the high-energy muons in these events are propagated to the in-ice detector [13]. The propagation of Cherenkov photons through the South Pole ice from the muons to the DOM’s is done using retrieval from tables (“photonics [14]”) according to emission angles and distances, followed by simulation of the readout electronics and detector trigger.

In the IceTop simulations used by both analyses, the observation level in CORSIKA was found to be mistakenly set *below* the height of the snow over the tanks in 13 stations in the northeast corner of the array. As a result, the reconstruction algorithm assumed greater snow attenuation than was actually simulated, and showers landing in the northeast corner were reconstructed with an overestimated  $S_{125}$ . After reconstructing all events with this issue corrected, new  $S_{125}$ -primary energy relationships were derived from Monte Carlo and the scale of the energy spectrum is slightly different from [3].

#### 4. Analysis: IceTop-alone and Coincidence

In [3], a function relating  $\log_{10}(S_{125})$  to  $\log_{10}(E/\text{GeV})$  was derived using Monte Carlo simu-

After reconstruction and cuts, the event set has a core position resolution of 6-20 meters, and a track direction resolution of 0.3-1.0 degrees, as a function of energy as shown in Figure 2.

### 3. Simulation

The simulations used in this work are the same as is described in [3]: four primary types (protons, helium, oxygen, and iron) simulated between  $\log_{10}(E/\text{GeV}) = 5.0$  and 8.0, as well as thinned simulations stretching up to  $\log_{10}(E/\text{GeV})$  of 9.5. The baseline simulations use CORSIKA-6990, SIBYLL 2.1, and FLUKA. Other high energy hadronic interaction models are used for



lations divided into many small bins of  $\log_{10}(S_{125})$ , in four ranges of zenith angles and for several different composition assumptions including the "H4a" model<sup>1</sup> [8], which is repeated here.

The energy resolution and bias of this technique (after the update) is shown in Figure 4(left). Correcting the observation level problem described above results in an improvement in resolution with respect to [3].

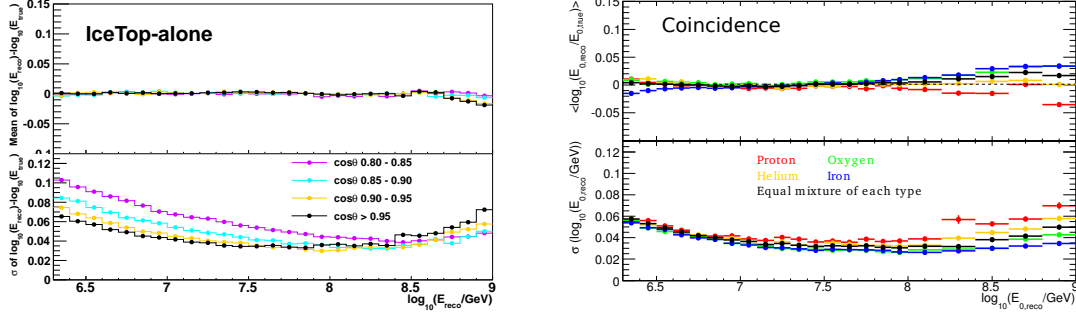


**Figure 3:** Energy reconstruction bias (top) and resolution (bottom) as a function of the reconstructed energy. For the IceTop-alone analysis (left), an H4a composition mixture is assumed, and four zenith angle bins are shown. For the Coincidence analysis (right), four nuclear types are shown.

In [5, 6], a neural network (NN) was used to estimate primary energy and primary mass using five variables: the shower size in IceTop  $S_{125}$ , the zenith angle  $\cos(\theta)$ , the muon energy loss in the ice  $dE_\mu/dX$  at  $X=1500\text{m}$ , and the number of high-energy stochastics under two selections (standard and strong). In this work, the neural network has been re-optimized and retrained after fixing the observation level problem in the Monte Carlo simulations. The chosen architecture maps the five inputs onto energy and mass using two hidden layers with respectively seven and four neurons (a 5-7-4-2 network). As before, half of the sample is used for the training (25%) and for testing (another 25%) the network. The other half (the verification sample) is used for comparing to data in the final stage of the analysis.

The energy dependence for the NN energy bias and NN energy resolution of both proton and iron showers is shown on Figure 4(right). Heavier primaries have a better energy resolution because of their lower intrinsic shower fluctuations. The worsening energy resolution beyond 100 PeV is believed to be caused by the worsening angular resolution which creates an extra smearing in  $S_{125}$ .

The neural network also reconstructs a natural logarithm of mass  $\langle \log A \rangle$  for each event. Within each bin of reconstructed energy, histograms of this reconstructed  $\langle \log A \rangle$  (“template histograms”) are constructed for each of the four simulated elemental types, as well as for experimental data. The four types exhibit four distinct shapes in each of the energy bins over the whole energy range. The histogram of NN mass outputs for data events is compared to the set of four template histograms, and the *fractions* of each which combine to form the data histogram is fitted using a binned likelihood fit that also accounts for Poisson fluctuations in MC [16].

<sup>1</sup>Since neither silicon nor magnesium were simulated, oxygen simulation was weighted by the sum of CNO and MgSi model components.

## 5. Systematic Uncertainties

Both analyses share sources of systematic errors in IceTop. To estimate the effect of the hadronic interaction model, a set was generated using QGSJET-II-03. Because  $S_{125}$  is most closely related to primary energy, this IceTop measurement is the dominant source of systematic uncertainty for the *spectrum* in both analyses. The calibration of the IceTop tanks contains an uncertainty of 3% on the absolute scale of  $S_{125}$ . A 0.2 m uncertainty on the snow attenuation length  $\lambda$  affects the  $S_{125}$  scale by approximately 3%, which translates to 4-7% uncertainty in flux.

In the IceTop-alone analysis, a composition model must be assumed, and there is a systematic uncertainty associated with this choice. Investigated in [3], this contribution to the overall systematic errors is isolated in Figure 5.

The dominant systematic on the *composition* determination is due to uncertainties related to the number of detected photons (the "light yield") in the in-ice detector. The total light yield uncertainty is +9.6%/–12.6% and has contributions from the DOM efficiency uncertainty (3%), hole ice uncertainty (3-5%) and uncertainties related to scattering and absorption properties of the ice (3-11%).

## 6. Results and Discussion

Figure 4 shows the result of the IceTop-alone 3-year analysis, for the 3 years separately on the left, and all combined on the right. This final energy spectrum is compared to the previously published one-year result [3]. A small shift of the spectrum is visible, which is expected after proper treatment of the observation level issue, as discussed in Section 3. Figure 5 shows a similar set of results for the Coincidence analysis, which agrees with the IceTop-alone analysis within the systematic errors.

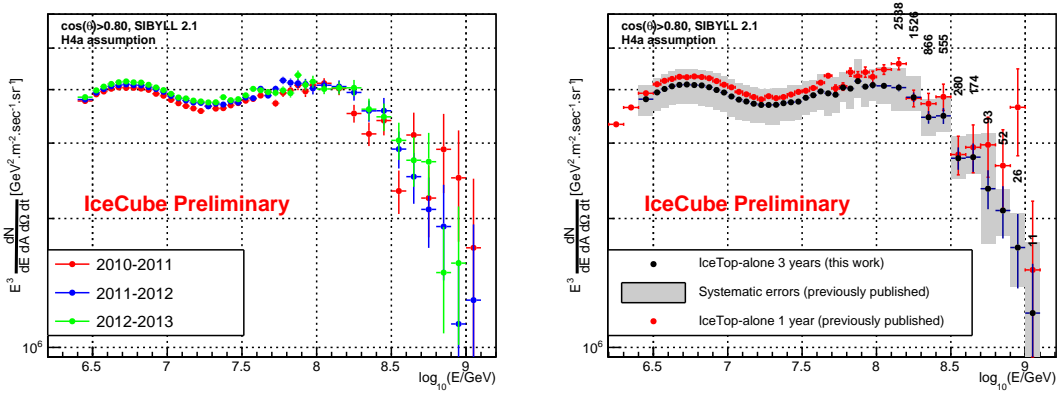


**Figure 4:** All-particle energy spectrum from the *IceTop-alone* analysis. Left: the three individual years, and Right: the combined three-year result compared to the previously published one-year result. The grey bands are the systematic errors from the previously published result [3], but applied to the new data points. Increased snow accumulation in the 3-year analysis causes the higher energy threshold with respect to [3].

The features in the energy spectrum seen in [3] are robust: a hardening of the spectrum around 20 PeV, and a softening again past 100 PeV. These features are present in both the IceTop-

alone and Coincidence analyses, and in all three years of data. The energy spectra of the three individual years agree well with each other within their systematic errors. The energy spectra of the two analyses agree within 2%, which is within the estimated systematic error due to the IceTop-alone analysis's assumption of a composition model.

The elemental energy spectra, deduced from multiplying the total energy spectrum with the reconstructed fractions from the template fitting of the NN mass output, are shown in both panels of Figure 6. We compare the result to alternate results from different systematics shown in grey, in particular: light yield factors (left), and QGSJET-II-03 (right), as discussed in Section 5. When broken down by the three individual years of data, both the general features and many of the small-scale fluctuations of these spectra are similar. Despite the large systematic uncertainties, clear differences in behavior between the four elemental groups are visible: protons and helium turning down steeply at lower energies, and oxygen and iron maintaining a harder spectrum up to higher energies.

Figure 7 sums the reconstructed fractions of all four elements weighted with the natural logarithm of their atomic mass  $\langle \log A \rangle$ . Systematic uncertainties are represented by alternate  $\langle \log A \rangle$  curves on this plot. The average composition increases from the lowest energies up to  $\sim 100$  PeV, where the slope of the trend changes. Approaching 1 EeV, there are hints that the average mass is getting lighter again, but in this region the error bars are large and the interpretation ambiguous. Although systematics dominate the absolute scale of the composition measurement, the general trends seen in Figures 6 and 7 are present in the systematics datasets.

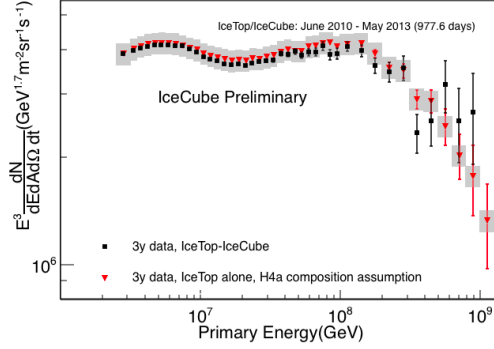


**Figure 5:** All-particle energy spectrum from the *Coincidence* analysis, compared to the IceTop-alone result. The grey bound shows the uncertainty due to the unknown composition on the energy spectrum measured by IceTop-alone.

## References

- [1] A. Achterberg et al., *Astropart. Phys.* **26** (2006) 155.
- [2] R. Abbasi et al., *NIM*, **A700**, (2013) 188-220.
- [3] M.G. Aartsen et al., *Phys. Rev. D*, **88**, (2013) 042004.
- [4] R. Abbasi et al., *Astropart. Physics*, **42**, (2013) 33.
- [5] T. Feusels et al., “Cosmic Ray Composition and Energy Spectrum between 2.5 PeV and 1 EeV with IceTop and IceCube”, *Contributions to the 33rd ICRC (Rio de Janeiro)*, (2013) paper 0861
- [6] T. Feusels, Ph.D. thesis, University of Gent (2013)
- [7] M. G. Aartsen et al., *JINST*, **9**, (2014) P03009.
- [8] T. K. Gaisser, *Astropart. Phys.* **35**, (2012) 801.

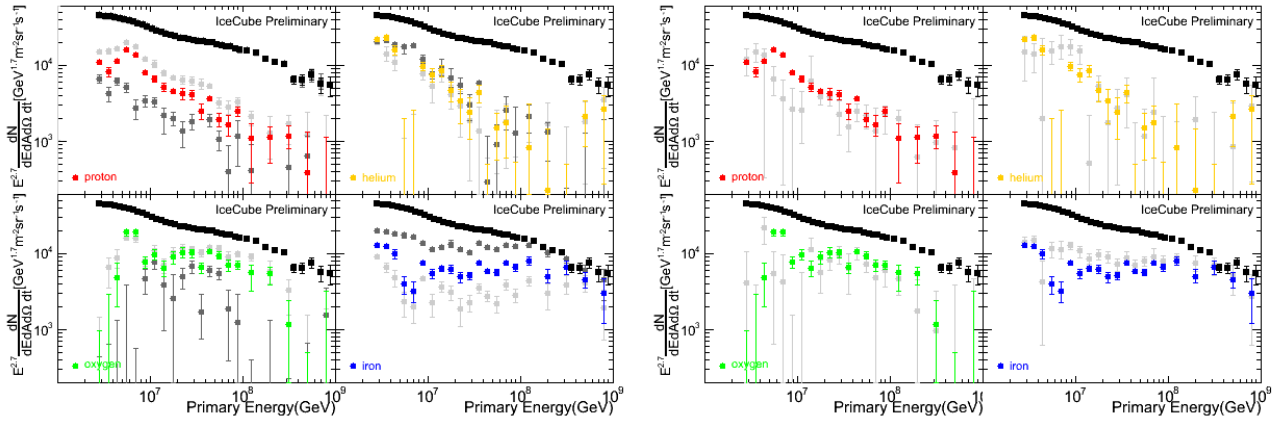


**Figure 6:** Individual spectra for the four nuclear types (protons, helium, oxygen, and iron), compared with two different sources of systematic uncertainty: the in-ice light yield (dark grey = -12.5%, light grey = +9.6%) on the left, and QGSJET-II-03 (light grey) as alternate hadronic interaction model on the right. The baseline result (in color) is the same on the left and right.

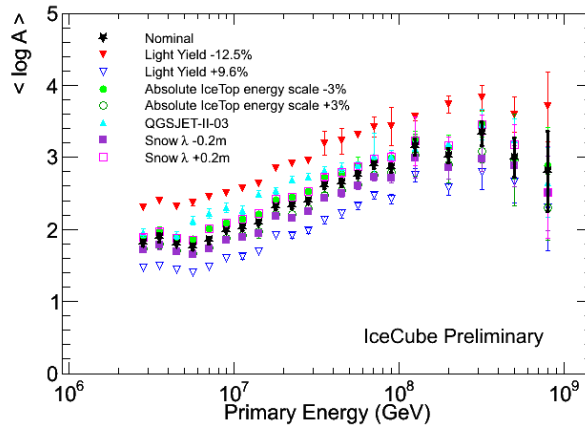


**Figure 7:** Mean log mass for the three years combined, using baseline simulations (black stars), and systematic uncertainties from alternate simulations represented by other symbols.

- [9] D. Heck et al., Report FZKA 6019 (1998).
- [10] E. J. Ahn, et al., *Phys. Rev. D* **80**, (2009) 094003.
- [11] G. Battistoni et al., *AIP Conference proceedings* **896**, (2007) 31.
- [12] S. Agostinelli et al., *Nucl. Instrum. Meth. A* **506**, (2003) 250.
- [13] D. Chirkin and W. Rhode “Muon Monte Carlo: A high-precision tool for muon propagation through matter” hep-ph/0407075 (2004)
- [14] J. Lundberg, P. Miočinović and K. Woschnagg et al., *Nucl. Instrum. Meth. A*, **581**, (2007) 619-631.
- [15] S. De Ridder et al., “Seasonal variation of the muon multiplicity in cosmic rays at South Pole”, *Contributions to the 33rd ICRC (Rio de Janeiro)*, (2013) paper 0763
- [16] R. Barlow and C. Beeston, *Computer Physics Comm.*, **77** (1993) 219-228.

# Studying Cosmic Ray Composition with IceTop using Muon and Electromagnetic Lateral Distributions

---

## The IceCube Collaboration<sup>†</sup>

<sup>†</sup>[http://icecube.wisc.edu/collaboration/authors/icrc15\\_icecube](http://icecube.wisc.edu/collaboration/authors/icrc15_icecube)

E-mail: [jgonzalez@icecube.wisc.edu](mailto:jgonzalez@icecube.wisc.edu)

In this contribution we will consider the methods at our disposal to estimate the mass of primary cosmic rays on an event-by-event basis using IceTop, the surface component of the IceCube detector at the geographical South Pole. Events are reconstructed using two lateral distribution functions, one for the muon component and one for the electrons and gamma rays. This results in a few parameters that are sensitive to primary mass: the muon density at large lateral distances and the steepness of the lateral distribution of the electromagnetic component of the air shower. This approach is complementary to the technique already used in IceCube, whereby one can get a mass-sensitive parameter using the air shower size in IceTop together with several observables from the deep portion of the detector. Most importantly, this approach allows the study of composition-dependent anisotropy, since the zenith angle range is not constrained by the requirement of detecting the air shower in the deep detector.

**Corresponding author:** J. G. Gonzalez

*Bartol Research Institute, University of Delaware, USA*

*The 34th International Cosmic Ray Conference,  
30 July- 6 August, 2015  
The Hague, The Netherlands*

It is well known that the muon content of an air shower, together with a measure of its electromagnetic component, can be used to estimate the energy and mass of its primary [1]. The main issue with the use of the muon content as an estimate of primary mass is the possible systematic differences between simulated and real air showers, arising from the lack of knowledge of high energy hadronic interactions. The IceTop detector is sensitive to the low-energy ( $E \gtrsim 200$  MeV) muon component of air showers [2]. Generally speaking, for near-vertical air showers and close enough to their axis, the signal from muons is overwhelmed by the signal from the electromagnetic (EM) component of the air shower (electrons, positrons and gamma-rays). This holds true in the zenith angle and lateral distance ranges that have been used in the cosmic ray spectrum determination with IceTop [3, 4, 5], where the lateral distance of any point is defined as the closest distance from the point to the shower axis.

In this article, signals recorded at large lateral distances are included for the first time in the event-by-event analysis of air showers recorded with IceTop. These signals are collected using a dedicated readout mode introduced in 2010 (Section 1). The general features of IceTop and the signals at large lateral distances are briefly described in Section 1 and their sensitivity to the muon content of the air shower is briefly reviewed in Section 2. This new analysis thus provides an extra observable which correlates to the number of muons in the air shower.

## 1. General Features of IceTop

The IceCube detector consists of two major components [6, 7]. It can measure air showers on the surface with IceTop, high energy muon bundles with the in-ice detector, and both components in coincidence provided that the air shower axis goes through both the surface and in-ice detectors. The specific characteristics of IceTop that are relevant for measuring the low-energy muon component of air showers is described in what follows. A more detailed description of IceCube and IceTop has already been presented elsewhere [7].

IceTop is an air shower array consisting of 81 stations forming a triangular grid with a separation of 125 m in its completed configuration. The results presented here were obtained with data collected between June 1st 2010 and May 13th 2011, when IceTop consisted of 73 stations. It is located above the deep IceCube detector at the geographical South Pole, covering an area of roughly one square kilometer. Each station consists of two ice Cherenkov tanks separated by ten meters. Each tank contains two Digital Optical Modules (DOMs) with a 10 inch photomultiplier tube (PMT) and electronics for signal processing and readout. A discriminator trigger occurs when the voltage in one of the DOMs in a tank has passed the discriminator threshold. The total charge collected at the PMT's anode, after digitization and baseline subtraction, constitutes the tank's signal. The tanks register signals ranging from 0.2 to 1000 Vertical Equivalent Muons (VEM). A Hard Local Coincidence (HLC) occurs when there are discriminator triggers in two neighboring tanks within a time window of 1  $\mu$ s. If there is a discriminator trigger but not an HLC, the result is a Soft Local Coincidence (SLC).

In previously-published analyses, including those measuring the all-particle spectrum and other IceTop analyses [3, 4, 5], the properties of the primary cosmic ray are reconstructed by first fitting the signal times with a function describing the shape of the shower front and then fitting the measured signals with a single Lateral Distribution Function (LDF) which includes an attenuation

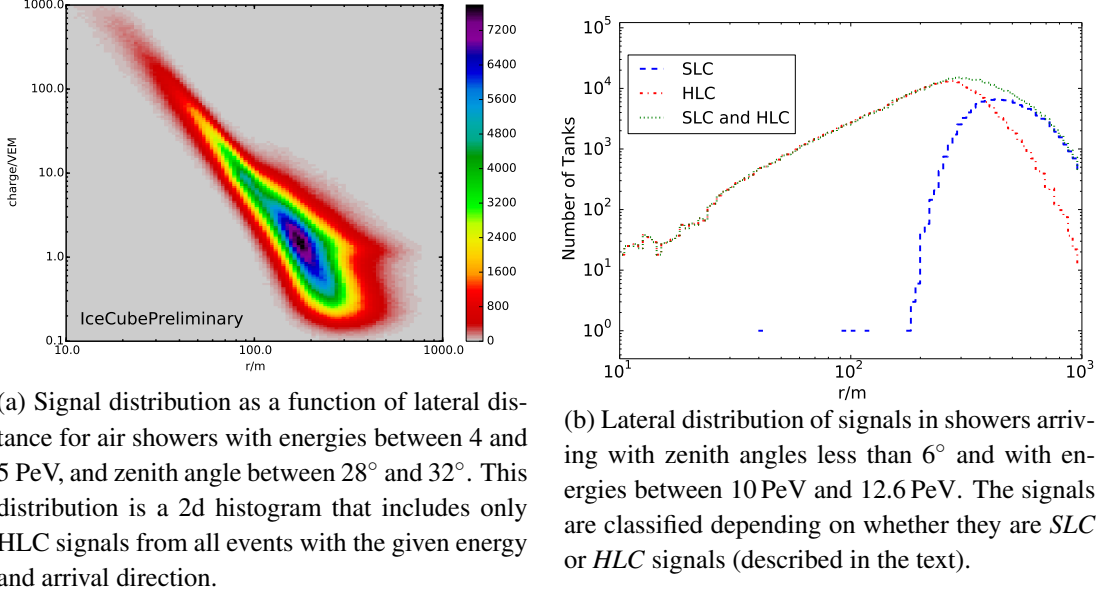


**Figure 1:** Lateral distribution of signals in IceTop

factor due to the snow cover on top of each tank [8]. The primary energy is given by the shower size  $S_{125}$ , defined as the signal interpolated at a lateral distance of 125 m. Only HLC signals were considered in these analyses. An example of the observed lateral distribution of HLC signals in IceTop data after selection—fiducial cuts on core location and on signal, and signals selected in a time window around the expected shower front time—is shown in Figure 1a for air showers with energies between 4 and 5 PeV, and zenith angle between  $28^\circ$  and  $32^\circ$ .

The main improvement described in this contribution is the addition of SLC signals, those where the partner tank within the station did not have a discriminator trigger. SLC signals occur at large lateral distances, where the triggering probability is smaller. An example of the lateral distribution of SLC and HLC signals from experimental data is shown in Figure 1b. The distinction between SLCs and HLCs provides a natural way to identify tanks where one expects to see a larger muon contribution to the signal. Generally speaking, one expects that signals at large lateral distances will be mostly due to muons, whereas the signals at short lateral distances will be mostly due to electrons and gamma-rays.

The sensitivity of SLC to muons can be seen in Figure 2, where the lateral distribution of SLC and all signals in experimental data is displayed. Note especially how the SLC signals follow a bimodal distribution. They can be described as two populations of signals. One population is the continuation of the main distribution at smaller distances, which roughly follows a power law, where the electromagnetic component of the shower dominates. The other population, with signals around 1 VEM, is made up mostly of tanks hit by one or more muons.

## 2. Modelling the Signal Distribution at Large Lateral Distances

In order to use SLC signals in the reconstruction procedure, the statistical signal distribution

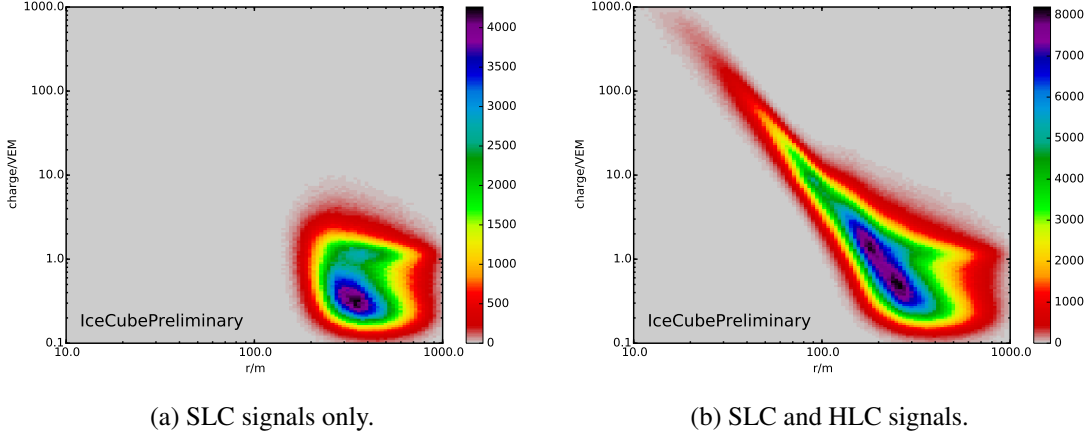


**Figure 2:** Signal distribution as a function of lateral distance for air showers with energies between 4 and 5 PeV, and zenith angle between  $28^\circ$  and  $32^\circ$ . Same as previous figure but including SLCs.

for low expected signals needs to be understood. This distribution is already used to estimate the average lateral distribution of muons at fixed energies and zenith angles [2, 9]. It is used now to produce a probability model of the signals in single events. This model is then used to implement a likelihood-based reconstruction procedure that yields a muon number for each event (Section 3).

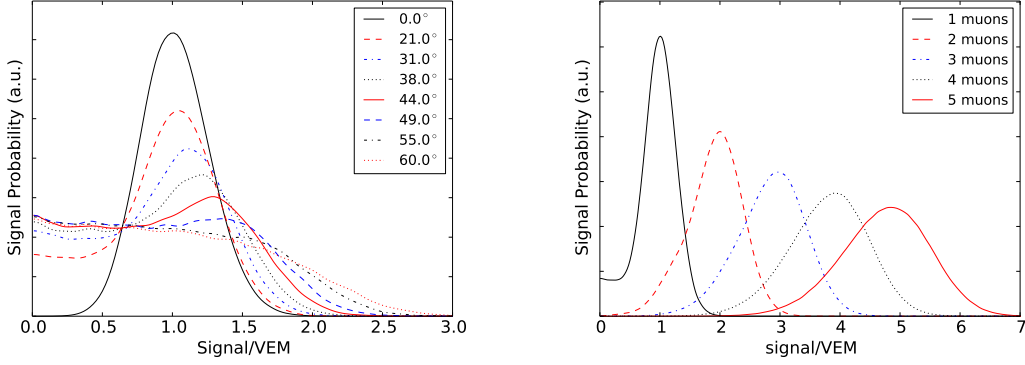
The characteristic features of the signal distribution at large lateral distances from the shower axis are mostly determined by the muon LDF. The muon LDF in IceTop can be described by the following function [10]:

$$\rho_\mu(r) = \rho_\mu(r_0) \left( \frac{r}{r_0} \right)^{-3/4} \left( \frac{320\text{m} + r}{320\text{m} + r_0} \right)^{-\gamma}, \quad (2.1)$$

which displays the same functional form as Greisen's function, with the first exponent of  $r$  fixed to  $-3/4$ , and  $r_0$  set to 600 m. It must be noted that the optimum value for  $r_0$  depends on energy. The  $\gamma$  parameter potentially depends on energy and zenith angle but one can use Greisen's value of 2.5. For a more detailed description, refer to the dedicated contribution in these proceedings [9].

The distribution of signals from EM particles (electrons and gamma rays) will roughly mimic their energy distribution, with a mean signal that corresponds to a few tens of centimeters of track length inside the tank. On the other hand, the distribution of signals from muons is mainly determined by the geometry of the tank. The signal distributions produced by single muons are obtained using the Geant4 toolkit [11]. Example distributions at various incident angles are displayed in Figure 3a. The distributions are clearly not symmetric. The peak of the distribution corresponds to muons that enter through the top of the tank and exit through the bottom. By definition, the peak position for vertically through-going muons is one *Vertical Equivalent Muon* (VEM). For muons arriving at a zenith angle  $\theta$ , the peak is at  $1/\cos(\theta)$ . The flat part at low signal values in Figure 3a corresponds to muons with a short track through the tank, known as *corner clipping* muons. At large angles, few muons go through top and bottom. For an integer number of muons, the signal distribution is just the multiple auto-convolution of the single-particle distribution. An example of this is displayed in Figure 3b. The statistical distribution of the total signal  $S$  for an expected aver-





(a) Signal distributions resulting from simulating the detector response for single muons arriving at fixed zenith angles from 0° to 57°.

(b) Signal distributions resulting from simulating the detector response for an integer number of muons arriving at 10°.

**Figure 3:** Detector response to muons.

age number of muons  $\langle N_\mu \rangle$  is given by a linear combination of the signal distributions for integer numbers of muons:

$$p_{\text{pois}}(S | \langle N_\mu \rangle) = \sum_{n=0}^{\infty} \frac{\langle N_\mu \rangle^n}{n!} e^{-\langle N_\mu \rangle} p(S | N_\mu = n) \quad (2.2)$$

## 2.1 The Likelihood Function

The concepts just described are included in a likelihood function of the air shower size, electromagnetic shower age, muon number, arrival direction, and core location. The likelihood function in this *two-LDF* model of air showers takes the form:

$$\mathcal{L}(S_{r_0}, s, \rho_{r_0}, \theta, \phi, \vec{r}_c) = \prod_i p(S_i | \theta, \langle S_{em}(\vec{r}_i) \rangle, \langle S_\mu(\vec{r}_i) \rangle), \quad (2.3)$$

where the index  $i$  labels all tanks in the array, with or without signal.  $S_{em}(\vec{r})$  and  $S_\mu(\vec{r})$  are lateral distribution functions of the electromagnetic and muon components respectively. They are given by NKG-like functions

$$\langle S_\mu \rangle = \rho_\mu(r) = \rho_{r_0} \left( \frac{r}{r_0} \right)^{-0.75} \left( \frac{r + r_{m\mu}}{r_0 + r_{m\mu}} \right)^{-\gamma} \quad (2.4)$$

$$\langle S_{em} \rangle = S_{r_0} \left( \frac{r}{r_0} \right)^{s-2} \left( \frac{r + r_m}{r_0 + r_m} \right)^{s-4.5}, \quad (2.5)$$

in which the relevant parameters are the shower age  $s$ , the electromagnetic signal at a reference radius  $S_{r_0}$  and the muon density at a reference radius  $\rho_{r_0}$ . The  $r_0$  parameter is an arbitrary constant that is absorbed in the normalization of the function. The Moliere radius  $r_m$  is a constant that depends on the arrival direction and the air density profile. It can be determined for each event. The equivalent number in the muon LDF  $r_{m\mu}$  is an empirical number that is fixed to 320 m, the

value determined by Greisen. The parameter  $\gamma$  is fixed to 2.5, the value from Greisen. Note that the expected muon signal in VEM is just the muon density. The number of muons going through the tank is  $N_\mu = \rho_\mu(r)(A_{top} \cos \theta + A_{side} \sin \theta)$ .

The probability of getting an electromagnetic signal, when  $\langle S_{em} \rangle$  is expected, is given by a normal distribution centered at  $\langle S_{em} \rangle$  with a width  $\sigma_{em} = 0.3 \langle S_{em} \rangle^{1/2}$  and the probability of measuring a muon signal is given the muon density as described in Section 1. In other words:

$$p_\mu(S|\theta, \langle S_\mu \rangle) = \sum_{n=1}^{\infty} p_{det}(S|\theta, n) \cdot p_{pois}(n|\langle N_\mu \rangle) \quad (2.6)$$

$$p_{em}(S|\theta, \langle S_{em} \rangle) = \frac{1}{\sigma_{em} \sqrt{2\pi}} e^{-(S_{em} - \langle S_{em} \rangle)^2 / 2\sigma_{em}^2}, \quad (2.7)$$

where  $p_{det}(S|\theta, n)$  is a tabulated response function like the one depicted in Figure 3b and  $p_{pois}(n|\langle N_\mu \rangle)$  is given by Eq.2.2. Using these functions, the probability of recording a signal  $S$  at a given lateral distance and arrival direction is

$$p(S|\theta, \langle S_{em} \rangle, \langle S_\mu \rangle) = p_{tr}(S) \cdot \int_0^S p_{em}(S_{em}|\theta, \langle S_{em} \rangle) \cdot p_\mu(S - S_{em}|\theta, \langle S_\mu \rangle) dS_{em}, \quad (2.8)$$

where  $p_{tr}(S)$  represents the discriminator trigger probability, which is parametrized as

$$p_{tr}(S) = \frac{1}{2} \left( \operatorname{erf} \left( \frac{\log(S) + 0.66}{0.14\sqrt{2}} \right) + 1 \right), \quad (2.9)$$

## 2.2 The Effect of Snow

The effect of the snow on the detection process is accounted for by multiplying the expected signal by an attenuation factor parametrized from Monte Carlo simulations. This factor depends on snow cover, primary energy, arrival direction, lateral distance and the distance from the detector to shower maximum. It is described in a separate contribution [8]. The muon component is assumed not to be affected by the presence of snow, and only the effect on the electromagnetic component is considered. If the expected EM signal is  $S_{em}$ , the expected EM signal after going through the snow  $S'_{em}$  is

$$S'_{em} = c_{snow} S_{em}, \quad (2.10)$$

and 2.8 becomes

$$p(S|\theta, \langle S_{em} \rangle, \langle S_\mu \rangle) = \int_0^S p_{em}(S'_{em}/c_{snow}|\theta, \langle S_{em} \rangle) \cdot p_\mu(S - S'_{em}|\theta, \langle S_\mu \rangle) dS'_{em}. \quad (2.11)$$

The attenuation due to snow is parametrized in terms of shower evolution stage  $t$ , the distance between the observation point and the shower maximum in units of radiation length in air ( $X_0 = 36.7 \text{ g/cm}^2$ ). It is possible, within this model of air showers, to relate the stage parameter to the shower age. If one assumes a Greisen profile, they are related by:

$$t = \frac{1}{2} \frac{X}{X_0} \left( 1 + \frac{3}{s} \right), \quad (2.12)$$

where  $X$  represents the slant depth of the observation point. The effect of this correction is under study.

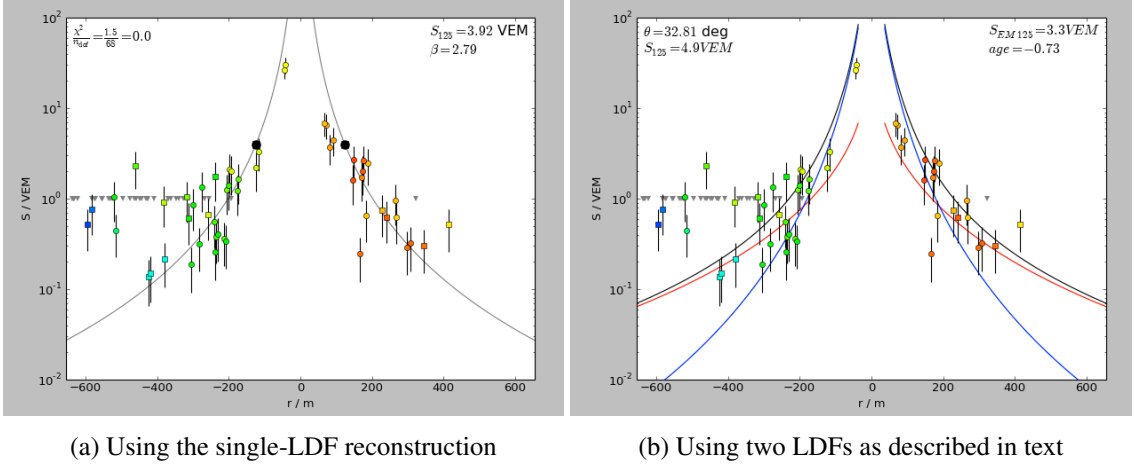


**Figure 4:** Reconstructed lateral distribution using the two methods: the *single-LDF* (a) and *two-LDF* (b). Note that the signals depicted as squares are SLCs and the circles are HLCs. SLCs are not used in the single-LDF reconstruction. The triangles mark the locations of tanks that did not register a signal even though they were functioning. The blue line in (b) denotes the electromagnetic LDF while the red line denotes the muon LDF. The black line is the sum of the EM and muon LDF.

### 3. Event by Event Reconstruction and Results

The reconstruction of IceTop events proceeds by first selecting the events according to standard selection criteria, and reconstructing them with a single-LDF using only HLC signals [3]. Standard selection criteria consist of fiducial cuts on core location and on signal. This gives the initial values for the core location, arrival direction and shower size. At this point, SLC signals are selected based on their agreement in time with the arrival of the air shower. This removes most random background coincidences. Finally, a two-LDF model is fit to the signals in the event, maximizing the log-likelihood function described in section 2.1.

A typical reconstructed event is shown in Figure 4. For comparison, the same event is shown with the single-LDF and the two-LDF reconstructions. As already noted, the single LDF reconstruction does not consider SLC signals (marked as squares in Figure 4). In this figure, the two branches of the LDF denote the early and late parts of the air shower. The filled gray triangles denote the location of tanks that had no signal. This particular event has most tanks—with or without signal—in the late part of the shower due to purely geometric reasons. Note the signals at large lateral distances around 1 VEM. Figure 4b shows three lines, the blue line represents the EM component, the red line represents the muon component, and the black line is the sum of the EM and muon LDFs. As expected, at short lateral distances the electromagnetic LDF dominates and determines the values of the HLC signals (circles), while at large lateral signals the muon LDF dominates, determining the probability that a tank has a signal and the values of the SLC signals (squares). Note also how the blue line follows the position of the small signals between 200 and 400 m from the core. It is important to keep in mind that the red line is not expected to go right through the points between 500 and 600 m. The red line gives the expected number of muons, which are either present—giving signals around 1 VEM—or there is no signal at all. For the same reason,

the black line does not follow the points. It includes information on tanks without signal.

#### 4. Outlook

The method described here uses SLC signals detected in IceTop in the analysis of individual air shower events. The inclusion of this kind of signals in the reconstruction has the potential to yield independent observables that are sensitive to the mass of the primary. The obvious one is the muon number at a fixed radius  $\rho_{r_0}$ , but the use of an NKG function for the EM component provides an age parameter. The sensitivity to composition arising from these two parameters is still under investigation.

The signal model relies on splitting the air shower in two components, a muon component and an electromagnetic component, but one can foresee improvements on this approach by considering multiple components in a way similar to the one described by Ave et al. [12].

#### References

- [1] K.-H. Kampert and M. Unger, *Astropart.Phys.* **35** (2012) 660–678, [[arXiv:1201.0018](#)].
- [2] **IceCube** Collaboration, J. G. Gonzalez et al., *Measuring the Muon Content of Air Showers with IceTop*, in *Proc. of the 18th meeting of the International Symposium on Very High Energy Cosmic Ray Interactions (ISVHECRI 2014)*, 2014. [arXiv:1501.0341](#).
- [3] **IceCube** Collaboration, R. Abbasi et al., *Astropart.Phys.* **44** (2013) 40–58, [[arXiv:1202.3039](#)].
- [4] **IceCube** Collaboration, B. Ruzybayev et al., *Cosmic ray composition and energy spectrum between 2.5 PeV and 1 EeV*, in *Proc. of the 33rd ICRC #246, Rio de Janeiro, Brasil*, 2013. [arXiv:1309.7006](#).
- [5] **IceCube** Collaboration, T Feusels et al., *Measurement of the cosmic ray energy spectrum with IceTop 73*, in *Proc. of the 33rd ICRC #861, Rio de Janeiro, Brasil*, 2013. [arXiv:1309.7006](#).
- [6] **IceCube** Collaboration, A. Achterberg et al., *Astropart.Phys.* **26** (2006) 155–173, [[astro-ph/0604450](#)].
- [7] **IceCube** Collaboration, R. Abbasi et al., *Nucl.Instrum.Meth.* **A700** (2013) 188–220, [[arXiv:1207.6326](#)].
- [8] **IceCube** Collaboration, K. Rawlins et al., *A Function to Describe Attenuation of Cosmic Ray Air Shower Particles in Snow*, PoS(ICRC2015)628 these proceedings.
- [9] **IceCube** Collaboration, H. Dembinski and J. Gonzalez et al., *Surface Muons in IceTop*, PoS(ICRC2015)267 in these proceedings.
- [10] K. Greisen, *Annual Review of Nuclear Science* **10** (1960) 63.
- [11] S. Agostinelli et al., *Nuclear Instruments and Methods in Physics Research A* **506** (2003) 250–303.
- [12] M. Ave et al., *Extensive air shower universality of ground particle distributions*, in *Proc. of the 32nd ICRC, Beijing, China*, 2011.

## Cosmic Ray Physics with the IceCube Observatory

---

### The IceCube Collaboration

[http://icecube.wisc.edu/collaboration/authors/icrc15\\_icecube](http://icecube.wisc.edu/collaboration/authors/icrc15_icecube)

E-mail: [timo.karg@desy.de](mailto:timo.karg@desy.de)

The IceCube Neutrino Observatory at the geographic South Pole comprises the cubic-kilometer deep-ice detector as well as a square-kilometer particle detector at the surface, IceTop. This unique combination allows measuring multiple components of cosmic-ray induced air showers in the PeV to EeV energy range: IceTop samples the electromagnetic component at ground level and enables studies of GeV muons in the periphery of the air shower; the deep-ice detector is sensitive to TeV muons in the shower core and in addition has collected a high-statistics sample of atmospheric muons from cosmic rays in the tens to hundreds TeV energy range. I will review recent cosmic-ray results obtained from IceCube data, including the cosmic ray energy spectrum and mass composition with three years of IceCube data, studies of the anisotropy at different energies, and investigations on the muon content of air showers.

**Corresponding author:** T. Karg\*

*DESY, Platanenallee 6, 15738 Zeuthen, Germany*

*The 34th International Cosmic Ray Conference,  
30 July- 6 August, 2015  
The Hague, The Netherlands*

---

\*Speaker.

## 1. Introduction

The IceCube Observatory, installed at the geographic South Pole, not only allows the measurement of atmospheric and astrophysical neutrinos, but also serves as an excellent instrument to study cosmic rays. IceCube comprises a detector component in the deep-ice, consisting of 86 vertical strings installed in boreholes of 2500 m depth. The bottom 1000 m of each string are instrumented with 60 digital optical modules (DOMs) each that detect the Cherenkov light emitted by charged particles traversing the detector [1]. In addition, the IceTop surface array serves as an air shower detector. IceTop comprises 81 stations at an altitude of 2835 m a.s.l. ( $X \approx 680 \text{ g cm}^{-2}$ ) that are installed at the top of the strings of the deep-ice detector with a typical horizontal spacing of 125 m. Each station has two ice-Cherenkov tanks, separated by 10 m, with a diameter of 1.8 m which are filled with 0.9 m of clear ice. The tank is instrumented with two DOMs operating at different gain to cover a dynamic range from about 1/6 VEM (vertical equivalent muon) to 1140 VEM [2]. The IceCube Observatory has been completed in December 2010, but already with partial detector configurations physics analyses were possible during the construction phase.

## 2. Observation Modes

In this section the different possibilities for detecting various components of air showers with the IceCube Observatory are discussed. Recent results employing these observation modes are presented in Sec. 3.

The IceTop surface array is triggered when six tanks in three stations register a signal in coincidence. The signal in the triggering tanks is typically dominated by the electromagnetic component of air showers. On every trigger generated by IceTop or the deep-ice detector, the signals from all tanks and the deep-ice detector are stored. IceTop has a small, central in-fill array with a threshold of about 100 TeV primary cosmic-ray energy, and the regular spaced array has a threshold of 300 TeV. It records air showers from primary cosmic rays of energies up to about 2 EeV above which the rate becomes too low for analysis. The direction of events passing standard selection cuts can be reconstructed with an uncertainty of about  $0.2^\circ$  at 30 PeV; the energy resolution for protons at this energy is 0.05 in  $\log_{10}(E/\text{GeV})$  [2]. Using only data from the IceTop array, the all-particle energy spectrum is derived, the anisotropy of PeV cosmic rays is studied, and searches for point-like sources of neutrons are performed.

The low trigger threshold of the individual IceTop tanks of 1/6 VEM allows detailed studies of the periphery of extensive air showers. At large distances from the shower core the signal in the tanks will be dominated by single muons. The coincidence between two tanks in a station, required for the array trigger, typically will not be fulfilled, but the data of these single tanks will be read out and stored on an air shower trigger. This allows measuring the GeV muon content of an air shower and supplies a handle to study cosmic-ray composition and hadronic interaction models. In addition, muon-poor showers can be selected as candidate events in searches for a diffuse flux, or point-like sources of PeV photons.

The deep-ice detector component is sensitive to high energy muons produced early in the air shower development. Vertical muons with a surface energy larger than about 1 TeV can trigger the deep-ice detector and this energy threshold increases with increasing zenith angle, i.e. growing

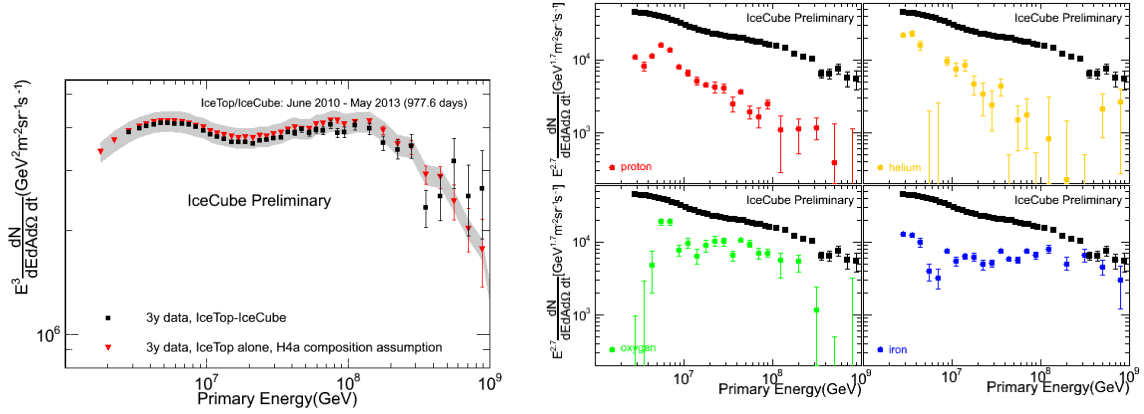


**Figure 1:** *Left:* All-particle energy spectrum based on three years of IceCube data. The red markers show the IceTop-alone analysis; the grey band represents the systematic uncertainty due to the unknown composition. The black markers show the result of the spectrum and composition analysis using coincident events in IceTop and the deep-ice detector [3]. *Right:* Energy spectra for four individual mass groups measured from coincident events [3].

overburden of ice. Due to the large detector volume, an unprecedented statistics of about  $10^{11}$  atmospheric muon events per year is collected. These atmospheric muons enable studies of the cosmic-ray anisotropy above 1 TeV. At higher cosmic-ray energies, the central muon core of the air shower can penetrate down to the deep-ice detector. The amount of light measured in the deep-ice detector allows to estimate the number of muons in the bundle, which in turn is related to the mass number  $A$  of the primary cosmic particle. Another, independent handle on cosmic-ray composition and hadronic interactions models.

Finally, the information from IceTop and the deep-ice detector can be combined on an event-by-event basis, leading to more precise measurements, but limiting the available zenith range to  $\theta < 30^\circ$  since the shower axis must pass through both detector components. Combining the cosmic-ray primary energy measured in IceTop with the size of the TeV muon bundle yields energy spectra for different mass groups of primary cosmic rays. Well-reconstructed showers in IceTop with a shower axis intersecting the deep-ice detector, but with no measurable TeV muons are good candidates for PeV photons. And in reverse, muons in the deep-ice detector whose track direction passes through IceTop, but which have no corresponding air shower in IceTop, are good candidates for astrophysical neutrinos interacting in the ice between the two detector components.

### 3. Results

#### 3.1 All-Particle Spectrum and Composition of Primary Cosmic Rays

The energy of primary cosmic rays is inferred from the reconstructed shower size at a distance of 125 m from the shower axis,  $S_{125}$ . At this distance, the shower size depends least on the mass of the primary particle. The shower size is mapped to primary cosmic-ray energy using CORSIKA [4] simulations with SYBILL 2.1 [5] and FLUKA [6] as high-energy and low-energy hadronic interaction models respectively. The efficiency of IceTop as a function of primary energy is determined with a detailed detector simulation, using Geant4 [7] to model the tank response and the effect of

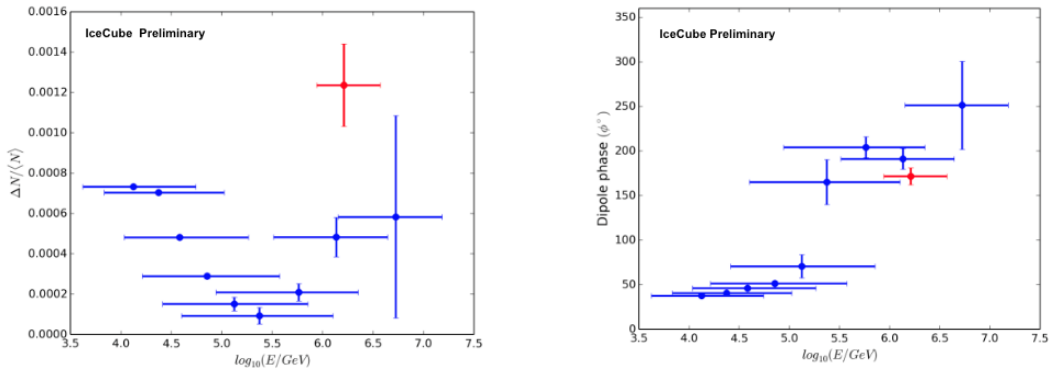


**Figure 2:** Amplitude (*left*) and phase (*right*) of the dipole anisotropy as function of primary cosmic ray energy. The data points mark the median energy of each subsample; the horizontal error bars show the 68% containment interval. Blue data points are obtained from the deep-ice detector; red data points are from IceTop [16].

snow on top of the tanks. An energy spectrum using one year of data of the partially completed IceTop detector with 73 tanks was previously published [8]. At this conference, an update based on three years of data (June 2010 to May 2013) was presented [3]. Figure 1 (left) shows the all-particle spectrum for the IceTop-alone analysis (red markers).

The analysis of air showers in IceTop where in addition the TeV muon core passes through the deep-ice detector allows the measurement of the primary mass. A first analysis based on one month of data with the 40-string, 40-station partial detector configuration has been published for primary energies up to 30 PeV [9]. The analysis technique has been refined and applied to three years of data. It uses an artificial neural network to map the shower size  $S_{125}$ , the cosine of the zenith angle  $\cos \theta$ , the muon bundle energy-loss in the ice  $dE_\mu/dX$  at  $X = 1500$  m slant depth, and the number of high-energy stochastic energy losses in the ice under two selections to the primary energy and a proxy of the primary mass. Histograms of the mass proxy are generated for small intervals in reconstructed energy and are fitted with template histograms derived from Monte Carlo simulations of four different mass groups (proton, helium, oxygen, iron), using a binned likelihood fit. This way the fraction of the different mass groups for each bin of reconstructed energy is determined [3]. Figure 1 (left) shows the resulting all-particle spectrum (black markers). It is in good agreement with the IceTop-alone result. In Fig. 1 (right) the individual spectra for the four different mass groups are shown. The heavy components, represented by oxygen and iron, maintain a hard spectrum up to higher energies than proton and helium. The systematic uncertainties of the measurement are discussed in [3].

### 3.2 Anisotropy

Cosmic-ray induced air showers above about 10 TeV can produce muons that can be measured and reconstructed with the deep-ice detector. Between May 2009 and May 2014, IceCube recorded more than  $2.5 \cdot 10^{11}$  muon events that allow detailed studies of the anisotropy as function of angular scale [10, 11, 12, 13], time [14], energy, and possibly primary mass. In addition, IceTop can be used to study anisotropies in the PeV energy range [15].



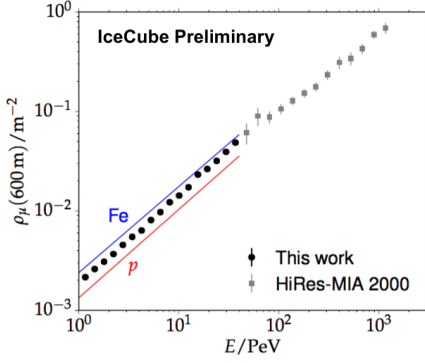


**Figure 3:** Measured muon density at 600 m from the shower axis in near vertical showers ( $\theta \approx 13^\circ$ ) [17]. Simulations with SYBILL 2.1 and FLUKA are shown for reference. The data are in good agreement with the HiRes-MIA measurement [18], which was performed at a different atmospheric depth of  $X \approx 860 \text{ g cm}^{-2}$ .

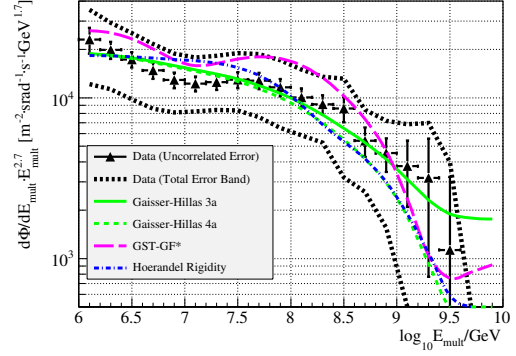


**Figure 4:** Muon multiplicity spectrum (cf. main text for definition) measured with one year of IceCube data. The error bars include systematic uncertainties that are uncorrelated between bins and statistical uncertainties; the error band represents correlated uncertainties (overall scaling effects) [19]. Different cosmic-ray models are shown for comparison [20, 21, 22].

In Fig. 2 the amplitude (left) and phase (right) of the dipole component of the anisotropy is shown. It can be seen that the energy resolution is poor since only a small fraction of the primary cosmic ray energy is transported by the muons and fluctuations of the muon energy loss in the detector are large. Still, the data can be separated in nine independent energy bins with increasing median energy. One data point (in red) obtained with IceTop at 1.7 PeV median energy is also displayed. The figure shows that a rapid shift of phase by almost  $180^\circ$  occurs at an energy between 130 TeV and 240 TeV. The dipole amplitude decreases with energy up to these energies, and increases again at higher energies. While the phase of the IceTop data agrees well with that found in the deep-ice data at similar energies, the amplitude of the anisotropy is larger in IceTop. This could indicate a difference in the energy distribution and the chemical composition of deep-ice and IceTop events and is currently under study [16].

### 3.3 Air Shower Physics

**Low energy (GeV) muons** in the periphery of air showers give an additional handle on primary mass and the systematic uncertainties introduced by hadronic interaction models. The low trigger threshold of the individual tanks of about  $1/6$  VEM allows determining muon densities on a statistical basis at large distances from the shower axis where the tank signal is not longer dominated by electromagnetic particles. For a sample of showers with equal reconstructed energy and zenith angle, tanks have been binned in distance to the shower axis and measured charge. At large distances (depending on the primary energy) two populations of tanks can be identified: tanks with a charge of approx. 1 VEM that have registered a muon and tanks with  $\ll 1$  VEM measuring electromagnetic particles. Slices at constant distance are fitted with a model for electromagnetic and muonic signals, taking into account multiple muons and the angular response of the tank to muons [17]. Figure 3 shows the measured muon density at 600 m from the shower axis. The measurement

is independent of air shower simulations. Simulations with SYBILL 2.1 [5] and FLUKA [6] are given for reference and the data are well bracketed by proton and iron simulations.

In the future, the measured muon lateral distribution function will be added to the IceTop reconstruction and the electromagnetic and muonic component of the shower can be reconstructed separately on an event-by-event basis. This is expected to improve IceCube's sensitivity to the mass of the primary cosmic particle considerably. First results of the improved reconstruction are presented in [23].

**High energy (TeV) muons** can be produced with large transverse momentum ( $p_T$ ). These muons will separate from the air shower core during flight and can be measured as distinct double tracks (core muons + high- $p_T$  muon) in the deep-ice detector [24]. The typical transverse momentum to produce laterally separated muons in IceCube is about 2 GeV, where parton interactions can be described in the context of perturbative quantum chromodynamics (pQCD). The analysis and simulation techniques for high- $p_T$  muons have been refined and the sensitivity to cosmic ray composition has been studied [25].

**High energy muon bundles** can be measured with the deep-ice detector over a much wider zenith angle range, and thus with much higher statistics, than what can be used for the coincident composition analysis (cf. Sec. 3.1). In this mode, a direct measure for the primary cosmic ray energy can not be obtained, but tests of cosmic ray models are possible. The relevant observables are the energy loss per length of the muon bundle in the ice and large stochastic energy losses. The latter allow to separate high energy single muons from muon bundles. Using air shower simulations, these observables are related to the muon multiplicity  $E_{\text{mult}} := E_{\text{prim}} \cdot (A/56)^{\frac{1-\alpha}{\alpha}}$ , where  $E_{\text{prim}}$  is the primary cosmic ray energy,  $A$  is the mass number, and  $\alpha = 0.79$  is an empirical parameter derived from simulation [19]. Figure 4 shows the muon multiplicity spectrum measured with  $1.2 \cdot 10^7$  muon bundle events from the 79 string configuration of IceCube. The data are compared to cosmic ray composition models from [20, 21, 22], which have been translated to  $E_{\text{mult}}$  using the equation given above.

### 3.4 Searches for Neutral Particles

With the IceCube Observatory searches for high energy neutrons, photons, and neutrinos have been performed.

**Neutron**-induced air showers cannot be distinguished from proton-induced showers. Since neutrons carry no electric charge they are not deflected in magnetic fields and a neutron source within the decay length of the particles would show up as an excess in the event distribution in celestial coordinates. With typical cosmic ray energies between 10 and 100 PeV, IceTop is sensitive to neutron sources within a distance up to about 1 kpc. Two searches have been performed. A binned all sky search using all cosmic-ray events in the zenith range  $\theta < 37^\circ$  with energies higher than 10 PeV revealed no statistically significant clustering. Figure 5 shows the upper limit on the neutron flux at 90% confidence level as a function of declination derived with four years of IceTop data [26]. A targeted search with an energy threshold of 100 PeV for neutrons from close-by millisecond pulsars,  $\gamma$ -ray pulsars, and high mass x-ray binaries showed no statistically significant correlations [26].

**PeV photons** are searched for by looking for muon-poor showers. A search has been performed with the 40 string configuration in the declination region  $\delta < -60^\circ$  [28]. No correlation of

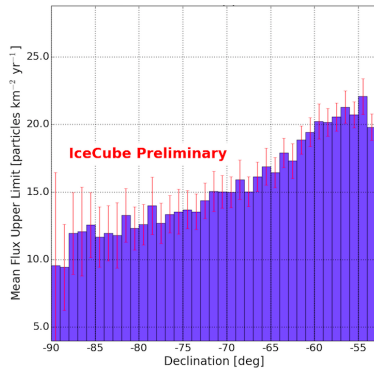


**Figure 5:** Upper limit (90% C.L.) on the flux of neutrons from point-like sources as a function of declination. The error bars indicate the statistical uncertainty [26].

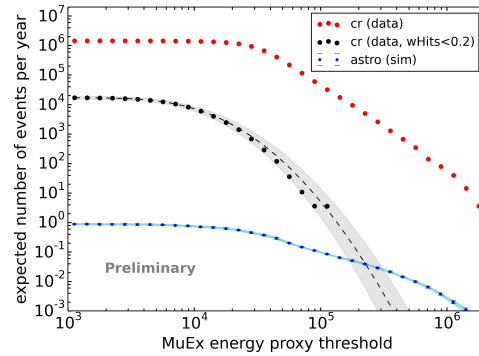


**Figure 6:** Atmospheric muon bundle event rates as function of the energy measured by the deep-ice detector before and after applying IceTop as active veto. The expected flux of astrophysical neutrinos is shown for reference [27].

photon candidates with the Galactic plane was found and an upper limit on the photon fraction of  $1.2 \cdot 10^{-3}$  was set in the energy range from 1.2 to 6 PeV. Further, no clustering of photon candidate events was observed in a search for point-like sources in the complete field of view. A similar analysis with the full IceCube detector is in preparation.

**Neutrino** searches in the Southern hemisphere suffer from atmospheric muons as dominant background. This has been mitigated in previous searches by using part of the instrumentation of the deep-ice detector as an active veto, thus reducing its effective mass. If IceTop can be used as an air shower veto, the whole ice volume below IceTop and above the deep-ice detector can be utilized as additional interaction target for astrophysical neutrinos. A study of the veto efficiency for IceTop has been performed [27]. Figure 6 shows the possible reduction of the cosmic ray background by using IceTop information. While the expected astrophysical neutrino rate after applying the veto is as low as 0.1 events per year due to the small solid angle for coincident events, the analysis demonstrates the capability and requirements of a surface veto array for the IceCube-Gen2 project.

#### 4. Future Plans

A new collaboration, IceCube-Gen2, has been founded in April 2015 to pursue the design and construction of the IceCube-Gen2 facility at the South Pole. It is envisioned to comprise a low-energy array, PINGU, for precision neutrino measurements, a  $\sim 10 \text{ km}^3$  high-energy deep-ice array to study the astrophysical neutrino flux [29] and a large area surface array consisting of a  $10 \text{ km}^2$  cosmic-ray detector and a  $\sim 100 \text{ km}^2$  air shower veto of less sophisticated detection units. The cosmic-ray detector together with the high-energy deep-ice array, due to the largely increased range of zenith angles for coincident events, is expected to boost the coincident data rate by a factor of 50 and enables lateral and production depth muon measurements for every event [30], promising the most precise studies of the transition region from Galactic to extra-galactic cosmic rays.

## References

- [1] F. Halzen and S. Klein, *Rev. Sci. Instrum.* **81** (2010) 081101.
- [2] **IceCube** Collaboration, R. Abbasi et al., *Nucl. Instrum. Meth. A* **700** (2013) 188–220.
- [3] **IceCube** Collaboration. POS(ICRC2015)334 these proceedings.
- [4] D. Heck, J. Knapp, J. N. Capdevielle, et al., *CORSIKA: A Monte Carlo code to simulate extensive air showers*, Tech. Rep. FZKA 6019, Forschungszentrum Karlsruhe, 1998.
- [5] E.-J. Ahn, R. Engel, T. Gaisser, et al., *Phys. Rev. D* **80** (2009) 094003.
- [6] A. Ferrari, P. Sala, A. Fassó, et al., *FLUKA: a multi-particle transport code*, 2005. CERN-2005-10 (2005), INFN/TC\_05/11, SLAC-R-773.
- [7] S. Agostinelli et al., *Nucl. Instrum. Meth. A* **506** (2003) 250–303.
- [8] **IceCube** Collaboration, M. Aartsen et al., *Phys. Rev. D* **88** (2013) 042004.
- [9] **IceCube** Collaboration, R. Abbasi et al., *Astropart. Phys.* **42** (2013) 15–32.
- [10] **IceCube** Collaboration, R. Abbasi et al., *Astrophys. J.* **718** (2010) L194–L198.
- [11] **IceCube** Collaboration, R. Abbasi et al., *Astrophys. J.* **746** (2012) 33.
- [12] **IceCube** Collaboration, R. Abbasi et al., *Astrophys. J.* **740** (2011) 16.
- [13] **IceCube** Collaboration, M. Aartsen et al., *Astropart. Phys.* **66** (2015) 39–52.
- [14] **IceCube** Collaboration, *Study of the time-dependence of the cosmic-ray anisotropy with AMANDA and IceCube*, in *Proceedings of the 33rd International Cosmic Ray Conference*, (Rio de Janeiro, Brazil), July, 2013. [arXiv:1309.7006](https://arxiv.org/abs/1309.7006).
- [15] **IceCube** Collaboration, M. Aartsen et al., *Astrophys. J.* **765** (2013) 55.
- [16] **IceCube** Collaboration. POS(ICRC2015)274 these proceedings.
- [17] **IceCube** Collaboration. POS(ICRC2015)267 these proceedings.
- [18] T. Abu-Zayyad et al., *Phys. Rev. Lett.* **84** (2000) 4276–4279.
- [19] **IceCube** Collaboration, M. Aartsen et al., *submitted to Astropart. Phys.* (2015) [[arXiv:1506.07981](https://arxiv.org/abs/1506.07981)].
- [20] T. Gaisser, *Astropart. Phys.* **35** (2012) 801–806.
- [21] T. Gaisser, T. Stanev, and S. Tilav, *Frontiers of Physics* **8** (2013) 748–758.
- [22] J. Hörandel, *Astropart. Phys.* **19** (2003) 193–220.
- [23] **IceCube** Collaboration. POS(ICRC2015)338 these proceedings.
- [24] **IceCube** Collaboration, R. Abbasi et al., *Phys. Rev. D* **87** (2013) 012005.
- [25] **IceCube** Collaboration. POS(ICRC2015)256 these proceedings.
- [26] **IceCube** Collaboration. POS(ICRC2015)250 these proceedings.
- [27] **IceCube** Collaboration. POS(ICRC2015)1086 these proceedings.
- [28] **IceCube** Collaboration, M. Aartsen et al., *Phys. Rev. D* **87** (2013) 062002.
- [29] **IceCube-Gen2** Collaboration. POS(ICRC2015)1146 these proceedings.
- [30] **IceCube-Gen2** Collaboration. POS(ICRC2015)694 these proceedings.

## An IceTop module for the IceCube Masterclass

---

### The IceCube Collaboration<sup>1</sup>

<sup>1</sup> [http://icecube.wisc.edu/collaboration/authors/icrc15\\_icecube](http://icecube.wisc.edu/collaboration/authors/icrc15_icecube)

*E-mail:* [hdembins@udel.edu](mailto:hdembins@udel.edu)

The IceCube Masterclass for high school students is an outreach project developed for the South Pole IceCube Neutrino Observatory. The Masterclass is designed to provide an authentic astrophysics research experience by demonstrating typical elements of IceCube research. It is a full-day event, consisting of engaging activities, educational talks, and scripted analyses, where students reproduce some of the main IceCube science results using real data. A highlight of the analysis activities are interactive applications, which run directly in standard web browsers and offer opportunities for students to intuitively develop insights into data processing. This contribution describes a new analysis module which reproduces the measurement of the cosmic ray energy spectrum with IceTop, the surface component of IceCube. The module features a web application that allows students to interactively fit representative IceTop events to determine the direction and energy estimator  $S_{125}$  from the raw data.

**Corresponding authors:** Hans P. Dembinski\*  
*Bartol Institute, University of Delaware*

*The 34th International Cosmic Ray Conference,  
30 July- 6 August, 2015  
The Hague, The Netherlands*

---

\*Speaker.

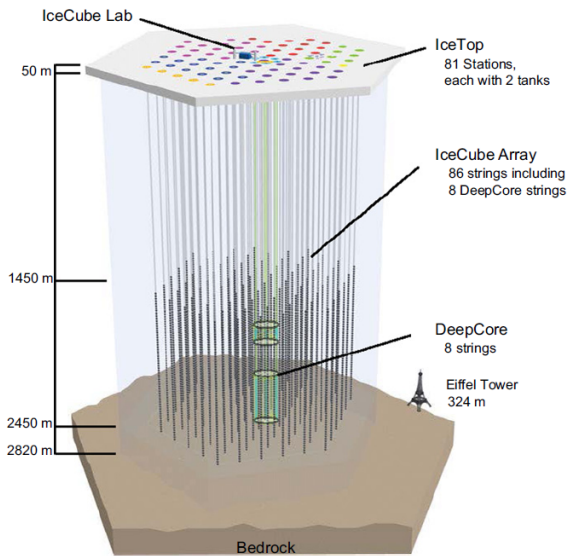


Figure 1: Schematic view of the IceCube experiment. The bulk of the light detectors are buried under 1.5 km of ice and form the in-ice detector. The in-ice detector is used mainly for neutrino astronomy and neutrino physics studies. The IceTop sub-detector consists of 81 pairs of ice-filled tanks at the surface. They serve two purposes: vetoing particles from cosmic-ray induced air showers that reach the in-ice detector (non-neutrino events), and studies of cosmic rays.

## 1. IceCube and the Masterclass

The IceCube Neutrino Observatory, shown in Fig. 1, is a cubic-kilometer neutrino detector located at the geographic South Pole. It has a rich physics program, including the study of extraterrestrial neutrinos, neutrino oscillations, searches for dark matter, and studies of the cosmic-ray spectrum, composition, and angular distribution. Its surface component, IceTop [1], located at 2835 m above sea level, is an excellent detector for probing cosmic rays [2], which are detected through secondary air shower particles produced during interactions in Earth's atmosphere.

In 2014, the IceCube Collaboration launched the IceCube Masterclass [3], a new educational program that gives high school students the opportunity to learn about cosmic rays and neutrinos, and what they tell us about the universe. Students discover that IceCube is a unique, extreme experiment, both because of its location and the phenomena studied. The IceCube Masterclass program was inspired by the International Masterclasses program, started in 2005 by the International Particle Physics Outreach Group [4], and supported in the USA by QuarkNet [5].

The IceCube Masterclass invites high school students, and accompanying teachers, to join an IceCube institute for one day. They experience real research in an authentic environment, including performing an analysis using IceCube data, meeting active physicists, and linking up in person and virtually with student peers from the U.S. and several countries in Europe. A highlight is the live interactive webcast with IceCube personnel at the South Pole station.

Each Masterclass leads students through one IceCube analysis, focusing on the fundamental aspects of astrophysical measurement. Preselected data sets are used to teach how to distinguish between signal and background events, develop the art of event selection, calculate an observable from data and determine the significance of a result. The technicalities of handling large amounts of data are avoided.

The first edition, held on May 2014, included around 100 students visiting five IceCube institutions in the U.S. and Europe. The second edition took place in March 2015 with 175 students in the U.S., Germany, Belgium and Denmark, at a total of ten institutions.

## 2. The IceTop module

In November 2014, the Education and Outreach Group and the Cosmic Ray Group decided to add a new analysis activity to increase the variety of topics available in the IceCube Masterclass, which so far focused on the observation of extraterrestrial neutrinos [6]. The measurement of the cosmic-ray flux with the IceTop sub-detector [2], an important result for investigating cosmic rays that is relatively accessible, was selected as the topic for the new activity.

The measurement of the cosmic-ray flux can be split into four steps. Step 1 is the reconstruction of air shower events from the raw data measured by the IceTop detector array, in particular the shower size  $S_{125}$ . This observable, which is the equivalent signal strength at a radial distance of 125 m from the shower axis, is a proxy for the energy of the incident cosmic ray. Step 2 is the selection of well-reconstructed events above the detection threshold of the detector, around 1 PeV. Step 3 is the conversion of the shower size  $S_{125}$  into an equivalent cosmic-ray energy; this assignment uses air shower simulations. The final step 4 is the computation of the cosmic-ray flux from a histogram of the measured cosmic-ray energies. The flux is obtained by dividing the event count per bin through the respective energy interval covered by the bin and the exposure of the detector over the time of data taking.

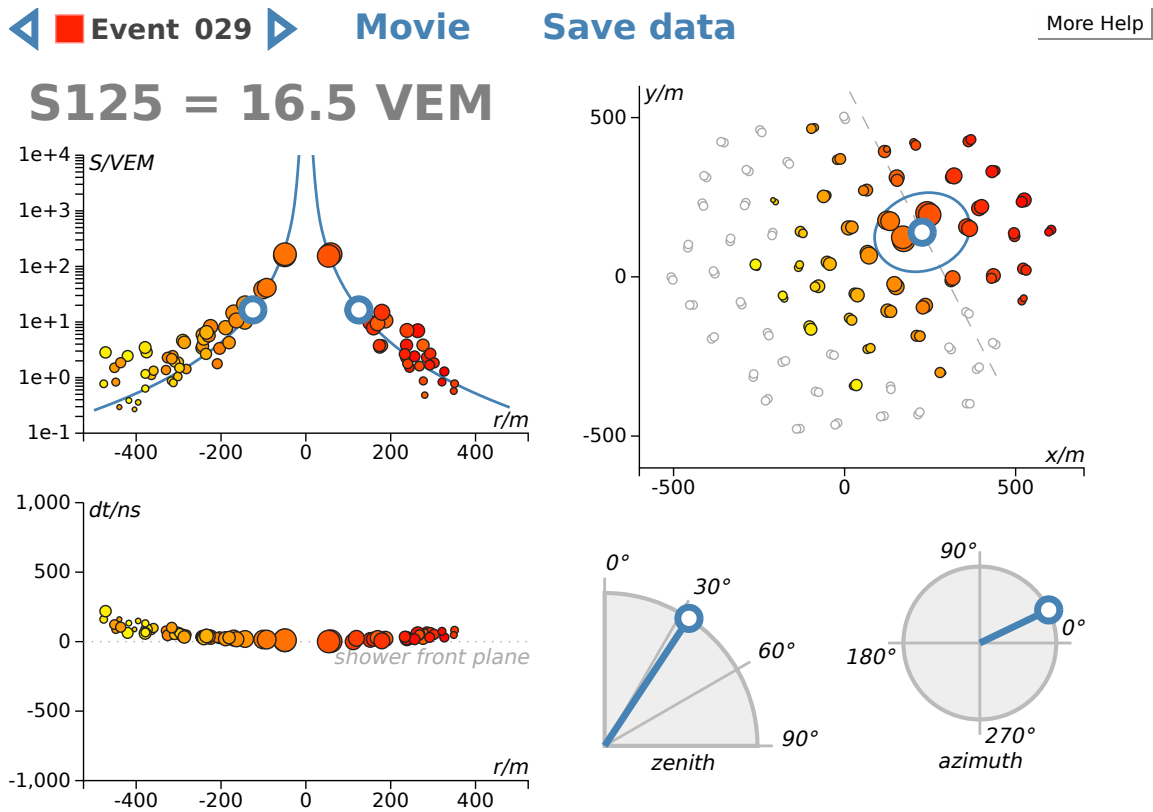
For the non-expert, data are numbers without meaning; they are abstract entities. Illustrating a complex data analysis, such as a measurement of the cosmic-ray flux from data, is the main educational challenge of the Masterclass. We address this challenge with dedicated interactive data visualizations, designed to make the concepts and processes underlying the analysis accessible to the students.

These applications create a playground for students to explore. Interaction with the visualization allows them to quickly build an intuitive understanding of the physics, the methods and the techniques, without requiring previous knowledge of the mathematics or programming skills needed to handle large data sets. This simple but deep approach aims to create a positive experience for the students – a feeling that they can be an IceCube researcher – that could have an impact on their future perception of and interest in science.

The new IceTop exercise followed this approach and was designed in two parts. An interactive analysis of real and simulated IceTop events formed the first part (step 1). The events presented to students were already pre-selected to simplify the exercise (step 2 described above is skipped).

The reconstruction of showers from raw data is rather intuitive. Students estimated  $S_{125}$  using the interactive fitting application shown in Fig. 2. To do so, they also had to reconstruct the direction and location of the shower axis. The fitting application runs inside current web browsers and is built on standard web resources; HTML, SVG, and JavaScript. The design focus was on simplicity and consistency. All interactive elements were given the same blue-gray color, to make them easily recognizable. Large round knobs invite the user to drag them around. Markers that represent signals have the same size and color in all three plots, and react immediately in unison when the orientation or location of the shower axis is changed.

In the second part of the IceTop analysis, students were guided to perform a simple measurement of the cosmic-ray flux based on the fitted  $S_{125}$  values from the first part. They learned how energies are assigned to air shower events (step 3), and how counting events in narrow energy bins leads to an estimate of the cosmic-ray flux that arrives at Earth (step 4).



Take a guess! The event is... **Real** **30 guesses**  
**50% correct**

Figure 2: The interactive fit of an air shower event in IceTop, as it appears on the Masterclass website [7]. Recorded signals (colored dots) are characterized by arrival time, encoded in the color, and their charge left in the detectors, encoded in the dot size. All blue-gray elements are interactive and can be clicked or dragged. A detailed explanation of the application can be found on the website.

The second part of the analysis activity used spread sheet-templates to perform calculations. Students first determined the relationship between  $S_{125}$  and the known cosmic-ray energy in simulated events by fitting a straight line in a double-logarithmic plot of the energy of the cosmic ray and the reconstructed value of  $S_{125}$ . Then they assigned this calibration to the real events in the set, which had been weighted beforehand to reflect their relative abundance in a full day of data. These weighted events were filled into an energy histogram. At this point, the cosmic-ray flux was computed using the given bin sizes in energy and the pre-determined exposure of the detector for one day of data.

An example result from the students is shown in Fig. 3 and compared with the published spectrum. The agreement is good, considering the extreme simplifications (only 15 weighted events, manual event reconstruction). The discrepancy in the first bin is caused by the low resolution of the energy assigned by the students in small shower events. It is difficult for humans to assess



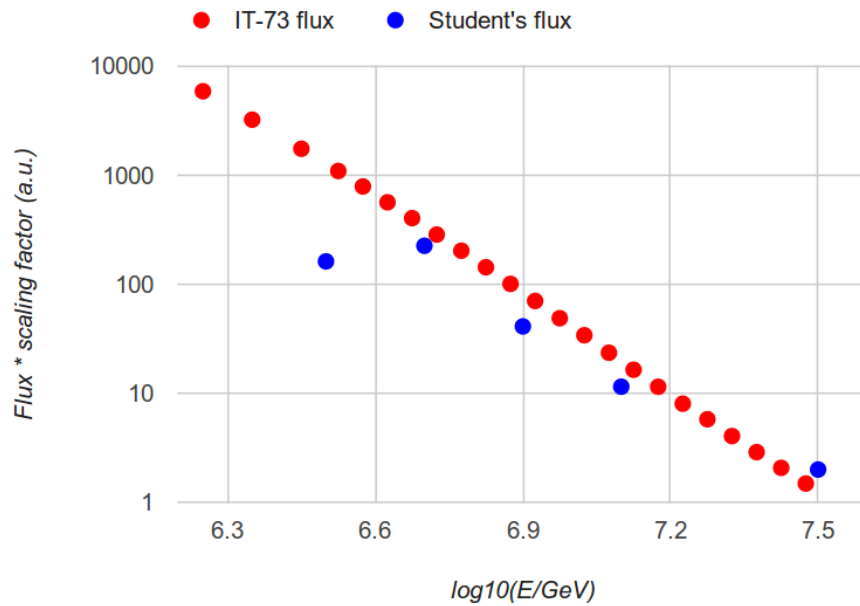


Figure 3: The cosmic-ray flux from the IT-73 publication [2] (red dots) and the flux estimated by the students in the exercise (blue dots). The student estimate scatters around the official result, because the estimate is derived from only 15 weighted events. The main features are nevertheless apparent, the power law shape and the rapid decrease with increasing energy. Both fluxes were scaled by a constant factor to have the y-axis run from 1 to 1000 in arbitrary units.

the shower size  $S_{125}$  in showers with few recorded signals. Low energy events, whose energy was interpreted as too low, fall outside of the histogrammed range, and thus create the dip in the first bin.

Students performed these tasks in groups of two to three, each with an independent set of 15 real and 15 simulated events. Using independent data sets allowed the students to combine their results in the end, to obtain an improved estimate of the cosmic ray spectrum by computing the average. Initially, students were asked to guess if each event was real or simulated data, and the truth was only revealed after the guess. The idea of this game was to convey that simulated and real data are virtually indistinguishable. The students responded very well to the game and it turned out to be an entertaining element, creating a positive form of suspense and competition between the groups.

### 3. Feedback and evaluation

A detailed pre- and post-evaluation of the Masterclass is performed by the students as part of each year's Masterclass. The evaluations are used to track the satisfaction of the students with the different aspects of the program. Since the purpose of the Masterclass is to raise interest in astroparticle physics, this is an important measure.

Results for this year's activities are shown in Fig. 4 for the two participating U.S. institutes. The activities got good response in general. The analysis activities differed between Wisconsin and

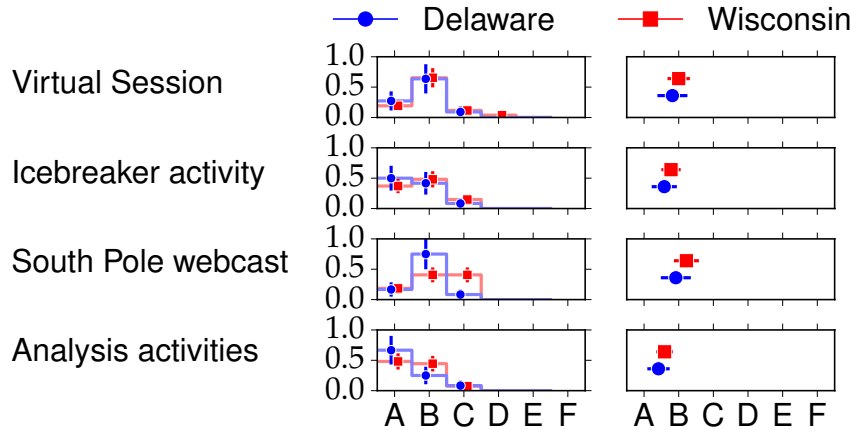


Figure 4: Student evaluation of the activities during this year’s Masterclass for WIPAC, University of Wisconsin-Madison, and University of Delaware. The scale follows the U.S. grading system, where A is the most positive grade, and F the most negative. *Left*: Evaluation histograms with Poisson uncertainties. *Right*: Average grade. The IceTop module was used only in Delaware.

Delaware. The new IceTop module was used only in Delaware, which replaced an analysis activity related to finding an anisotropy in the neutrino flux.

The students expressed special preference for the interactive parts, like the analysis activities and the Icebreaker activity.

#### 4. Ideas for future development

The IceTop module got positive feedback and will remain part of the IceCube Masterclass program in following years. The IceTop analysis could also be used by new undergraduate researchers as a gentle introduction to this research field. Further development of supporting educational resources will also enable its use as a research-based activity in classrooms.

The first part of the module, the interactive fit of IceTop events, could also be used in other contexts. It is an intuitive challenge, similar to solving a puzzle. The application could be part of the activities during an Open House Day at the university. A computer could be set up for visitors to interact with IceTop events. Also, physics institutes working on IceTop could link to the application on their websites to illustrate how the experiment works.

A stand-alone version is planned for these uses. To increase its appeal to a more general audience, the stand-alone version is planned to incorporate a passive demonstration mode – serving as a tutorial – and a ranking list for participating users could serve as a reward system. Rankings could be based on the achieved total  $\chi^2$ -value of the fits, and the percentage of correct guesses on the origins of the events.

#### References

- [1] IceCube Collaboration: R. Abbasi *et al.*, Nucl. Instrum. and Meth. **A700** (2013) 188-220 [arXiv:1207.6326].

- [2] IceCube Collaboration: M. G. Aartsen *et al.*, Phys. Rev. **D88** (2013) 042004 [arXiv:1307.3795].
- [3] IceCube Collaboration, Masterclass: <http://icecube.wisc.edu/masterclass> (2015).
- [4] International Particle Physics Outreach Group: <http://ippog.web.cern.ch> (2015).
- [5] National Science Foundation and the Office of High Energy Physics, Office of Science, U.S. Department of Energy, QuarkNet: <https://quarknet.i2u2.org> (2015).
- [6] IceCube Collaboration: M. G. Aartsen *et al.*, Science **342** (2013) 1242856 [arXiv:1311.5238].
- [7] H. Dembinski and D. Schultz, Interactive fit of IceTop events:  
<http://icecube.wisc.edu/viewer/icetop> (2015).

## A Function to Describe Attenuation of Cosmic Ray Air Shower Particles in Snow

---

**The IceCube Collaboration<sup>1</sup>,**

<sup>1</sup> [http://icecube.wisc.edu/collaboration/authors/icrc15\\_icecube](http://icecube.wisc.edu/collaboration/authors/icrc15_icecube)

E-mail: [krawlins@uaa.alaska.edu](mailto:krawlins@uaa.alaska.edu)

Snow overburden has become a part of the IceTop detector at the South Pole, and becoming more significant over time as snowdrift buries the array. Snow attenuates the electromagnetic component of cosmic ray air showers before they reach the detectors, reducing the measured signals, raising the threshold of the array in general, and introducing a potential source of systematic error in measuring shower energy. Understanding this attenuation is vital for shower reconstruction and energy resolution. A simulation of cosmic ray air shower particles has been used to map the attenuation response due to snow, and parameterize the behavior of the attenuation as a function of zenith angle and shower evolution stage.

**Corresponding authors:** K. Rawlins<sup>1\*</sup>

<sup>1</sup> *University of Alaska Anchorage, Department of Physics and Astronomy*

*The 34th International Cosmic Ray Conference,  
30 July- 6 August, 2015  
The Hague, The Netherlands*

---

\*Speaker.

## 1. Overview: Why is a complicated snow reconstruction necessary?

IceTop [1] is the surface component of the IceCube Observatory, composed of tanks of frozen water deployed at the surface of the Antarctic ice at the South Pole. Although the tanks were initially deployed with their tops flush with the snow surface, drifting snow at the site buries the tanks over time. The rate of accumulation is irregular over the array, but is about 20 cm per year on average. Figure 1 shows the snow coverage on the array, measured in three different years. Some tanks have very little snow overburden; others have close to 3 meters of coverage.

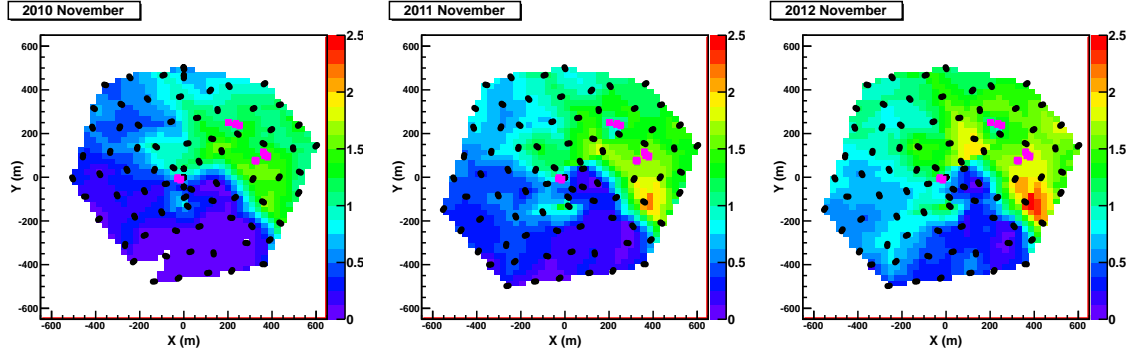


**Figure 1:** Snow accumulation over the IceTop detector, measured in three different years: 2010, 2011, and 2012. The pink dots indicate the positions of buildings at the site.

The charged particles in the air showers measured by IceTop get attenuated by any snow that is piled on top of a tank. A reconstruction algorithm must take into account these varying snow depths when computing the signals that are expected in a tank; one would expect smaller signals in a deeply-buried tank. But how much smaller?

In analyses published so far [2, 3, 4, 5] the expected signal in a snow-covered tank is attenuated by a simple exponential:

$$S/S_{nosnow} = \exp(-x/\lambda_{eff}),$$

where  $x$  is the slant depth of the tank through the snow (equal to the snow depth  $z$  divided by  $\cos(\theta)$ ), and  $\lambda_{eff}$  is the “effective attenuation length” due to snow. The same attenuation formula is applied uniformly to all tanks regardless of their distance from the core and in the same way for all showers regardless of their energy, composition, or zenith angle.

In reality, however, the physics of snow attenuation can be complicated in a variety of ways. For one thing, electrons and photons experience snow attenuation much more so than muons, and the relative contributions of electrons, photons, and muons to the tank signal depend on several factors, such as distance of the tank to the center of the shower and the shower morphology which depends on the energy, composition, and zenith angle of the shower. In addition, tank signals result not just from one incoming particle but a whole spectrum of them, and since the response of the snow depends on the particle energy, the shape of the spectrum affects the overall attenuation. The spectrum of the EM particles, like the fraction of signal from muons, depends on the distance to the core and the shower morphology. Where particle energies are very high (such as near the shower core), snow can even result in production of particles rather than attenuation [6]. When applying a “one size fits all” treatment to all tanks as we do currently, all of these effects are averaged over into

a single “effective attenuation length”. This effective  $\lambda_{eff}$  cannot be predicted easily from theory, and varies from year to year as the tanks are buried by more snow and the signal becomes more dominated by muons [5].

A better way of correcting for snow is to: a) estimate the fraction of the signal which is electromagnetic, and apply a snow correction to *only* that fraction, and b) to develop a correction which is a function of the tank’s distance to the core, and the shower’s morphology. This work is a continuation of what was begun in [6], in which a simulation of IceTop-like tanks at discrete radii and under discrete snow depths is used to develop such a function. The expectation is that this more complicated function will replace the simple exponential, and result in better reconstructions of shower sizes and energies.

## 2. The simulation

Vertical (zenith= $0^\circ$ ) showers from proton and iron primaries were simulated using CORSIKA [7] and FLUKA [8], at discrete energies of  $\log(E_{primary}/GeV) = 5.0, 5.5, 6.0, 7.0,$  and  $8.0$ . A smaller sample of showers at non-vertical zeniths ( $30^\circ, 45^\circ,$  and  $60^\circ$ ) at these same energies were also produced. The showers were thrown at a fictitious ideal array comprised of 235 single IceTop-like tanks arranged in rings of constant radius. The layout of the tanks is shown in Figure 2; there is a dense inner core of tanks at radii of 3, 5, 7, and 10 meters, a series of tanks at intermediate distances (15 - 200 meters), and more sparsely-spaced rings out to 500 meters. The azimuths of the tanks in the dense inner core are offset so as to avoid physical overlap between the closely-spaced tanks.

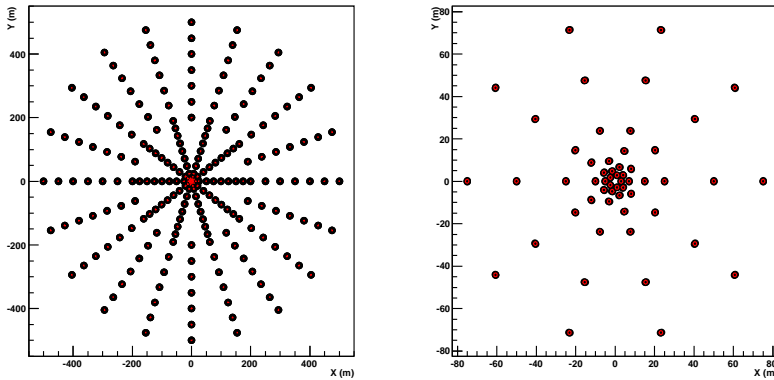


**Figure 2:** Layout of the tanks in the simulation. Left: the full array of tanks. Right: zoomed-in look at the tanks within 80 meters of the core.

A detector simulation package based on GEANT4 [9] is used to simulate the response of the tanks to the air shower particles. To restrict this study to electromagnetic particles only, all the muons in the shower are removed from the simulation before injection into the detector simulation. Photons which arrive at the photocathode of each DOM are recorded and counted. No simulation of other IceTop-specific downstream processes such as generating waveforms or triggers is performed; this study focuses on photoelectrons only.

Each of the simulated primaries is aimed at the array's center ( $x=0, y=0$ ). However, because CORSIKA includes a magnetic field, the charged particles will experience some deflection. Since the shower as a whole carries a net positive charge, vertical events are deflected slightly to grid south of the origin in the CORSIKA coordinate system. When present, this small offset is taken into account when computing the distance to the shower core for each of the tanks in the simulation, and becomes significant only for the very close tanks at low energies.

Each set of showers is repeated with the same array under different uniform coverages of snow, with depths ranging from 0 to 4 meters.

### 3. Attenuation curves

For each primary energy and mass simulated, photoelectrons arriving at each tank are counted, and the results are sorted according to the radius of that tank from the shower core and the snow coverage over the tank. The results can be visualized with a set of "attenuation curves", such as those shown in Figure 3. Each small panel in this figure represents a different radius  $r$  from the shower core. Within each panel is an attenuation curve ( $S/S_{nosnow}$  vs. snow depth  $x$ ) for tanks at that radius. The entire figure depicts attenuation curves for a particular primary energy and mass (for instance "protons at 1 PeV"); similar figures can be made for all primary energies and both masses. All of the curves, by construction, intercept the y-axis at a value of 1.

**Table 1:** Offsets in core location due to magnetic deflection (in meters along the y-axis).

$\log(E/GeV)$	protons	iron
5.0	-0.31	-7.10
5.5	0	-2.44
6.0	0	-0.62
7.0	0	0
8.0	0	0

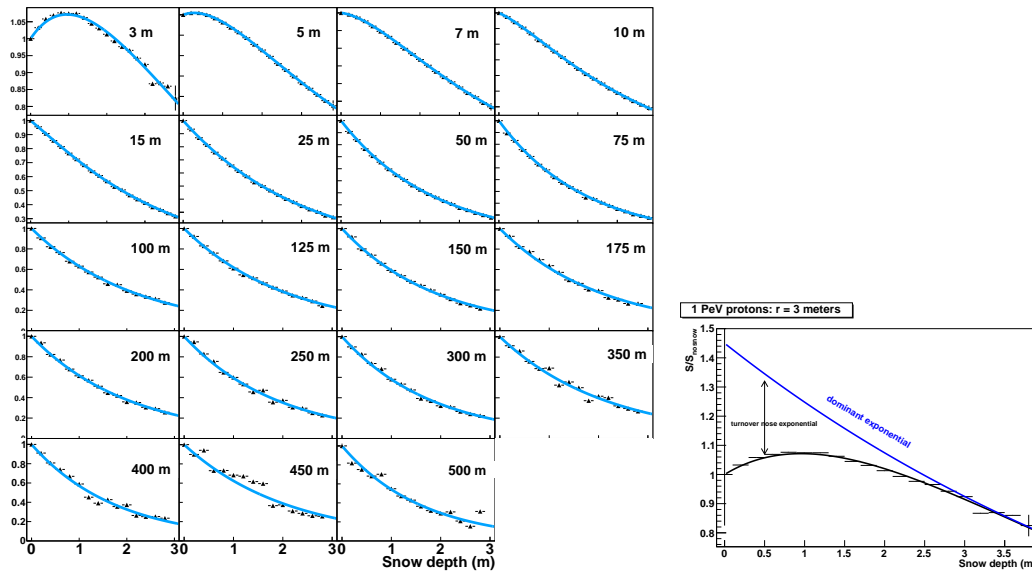


**Figure 3:** Left: Series of attenuation curves, for 16 different distances from the core (ranging from 3 meters to 500 meters), for 1 PeV vertical proton primaries. Right: Sketch of the idea of a dominant exponential and a turnover nose term. Note: the blue curve is *not* an actual fit to this curve, but is drawn in by hand to visualize the construction of the general function.

Beyond  $r = 30$  meters, all of the attenuation curves look like a simple exponential decay. But closer than  $r = 30$  meters, the attenuation curves exhibit signs of particle production at small depths, followed by eventual exponential attenuation deeper into the snow. A general form which fits all the attenuation curves well is a “dominant exponential with turnover nose”:

$$S/S_{nosnow} = c_0 \exp(x \cdot s) - (c_0 - 1) \exp(x \cdot s_{nose})$$

The first term describes the “dominant exponential”, which is evident in all tanks at all distances. Its slope is  $s$ , which one expects to be a negative number, and  $c_0$  describes where the dominant exponential intercepts the  $y$ -axis. The second term describes the “turnover nose”, which appears only for small radii, and is non-zero only if  $c_0$  is greater than one. It is an upside-down exponential whose slope is  $s_{nose}$ , another number expected to be negative. Figure 3 (right) demonstrates the contributions of these two terms to the overall curve. For tanks further away than 30 meters,  $c_0 = 1$ , and the second term disappears.

First, all attenuation curves are fit to the function above, with  $c_0$  restricted to 1.0 for tanks beyond 30 meters and all three parameters ( $s$ ,  $c_0$ , and  $s_{nose}$ ) floating free for tanks within 30 meters. Next, we examine each of these parameters as a function of  $r$ , and primary energy/composition, to search for parametrizable patterns. It has been argued by [10, 11] that the measurable properties of an air shower are related to the number of particles at shower maximum, and the stage of shower evolution  $t$ :

$$t = \frac{X - X_{max}}{X_0},$$

where  $X$  is the slant depth through the atmosphere traveled by the shower,  $X_{max}$  is the slant depth of shower maximum, and  $X_0$  is the radiation length (36.7 g/cm<sup>2</sup>). Therefore in the following sections we study the behavior attenuation curve parameters ( $s$ ,  $c_0$ , and  $s_{nose}$ ) as a function of  $t$ , rather than as a function of primary energy and composition.

### 3.1 $R > 30$ meters: the dominant exponential

Figure 4 shows the fit values of  $s$  for different showers as a function of radius. For the points beyond 30 meters radius, no turnover nose is allowed and  $s$  is the *only* free parameter. Although the protons (solid symbols) and iron (open symbols) occupy very different regions of this plot, a composition-independent pattern arises when the points in Figure 4 are organized by average stage of shower evolution  $t$ , represented by colors. All the  $s$ 's past 30 meters can be fit to a function of  $t$ :

$$s = d + e \cdot t + \gamma \log_{10}(r)$$

where  $d$ ,  $e$ , and  $\gamma$  have best-fit numerical values shown in Table 2.

### 3.2 $R < 30$ meters: the turnover nose

Once the fit to  $s$  past 30 meters is complete, these numbers are held fixed, and the attenuation curve fits are repeated but with only  $c_0$  and  $s_{nose}$  allowed to float free. Once again, patterns related to  $t$  emerge, as shown in Figure 5. As with  $s$ ,  $c_0$  and  $s_{nose}$  can be fit to a general function of  $t$ :

$$c_0 = A \exp(-r/(r_0 + B \cdot t)) + 1.0$$



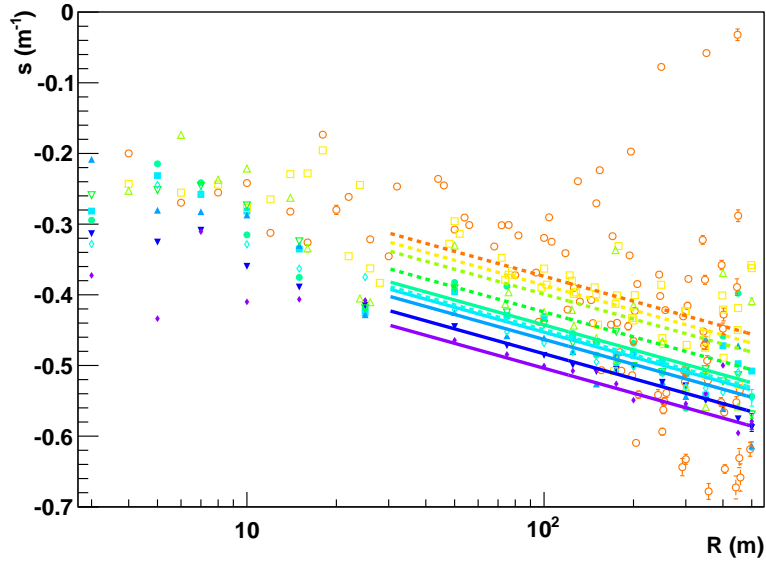


**Figure 4:** Fitting the exponential slope, using radii  $> 30$  meters. Solid points = proton showers, open points = iron showers. The color of the points represents the stage of shower evolution  $t$  (violet = -1, red = 10).

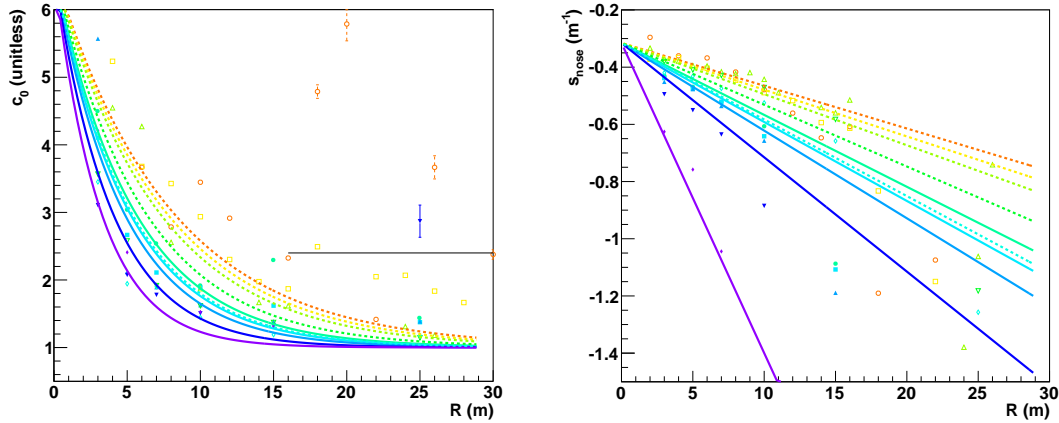


**Figure 5:** Fitting the features of the “turnover nose” (left =  $c_0$ , right =  $s_{nose}$ ) at small radii. Solid points = proton showers, open points = iron showers. Stage of shower evolution  $t$  is represented by color (violet = -1, red = 10).

$$s_{nose} = a + (b \log_{10}(t + 1.0) + c)r$$

where  $A$ ,  $r_0$ ,  $B$ ,  $a$ ,  $b$ , and  $c$  and additional best-fit numerical values shown in Table 2. As expected,  $c_0$  approaches a value of 1 as the radius goes beyond 30 meters, and although  $s_{nose}$  appears to diverge in this region, its effect is modulated by  $c_0$  going to 1, making it less and less relevant to the overall curve as 30 meters is approached.

**Table 2:** Best-fit values for the parameters that go into the complete snow attenuation function. Values obtained when fitting *only* proton or iron showers are shown for comparison.

parameter	both compositions	p / Fe individually
$d$	-0.259	-0.263 / -0.293
$e$	0.0133	0.0136 / 0.0195
$\gamma$	-0.116	-0.112 / -0.121
$A$	5.57	6.88 / 5.80
$B$	0.489	0.248 / 0.117
$r_0$	3.63	3.40 / -0.756
$a$	-0.317	-0.321 / -0.334
$b$	0.0312	0.0264 / 0.0232
$c$	-0.0457	-0.0486 / -0.0331

#### 4. Next steps: using this function in reconstruction

In order to apply this function to actual IceTop cosmic ray air shower data, there are two additional functions which must be explored and quantified.

- *Estimate the fraction of the signal which is electromagnetic.* Near the core of a shower the signals in tanks should be dominated by EM particles, whereas at the edge of the shower it should be dominated by muons. The fraction of the signal which is electromagnetic  $f_{EM} = S_{EM}/(S_{EM} + S_{\mu})$  is a function of the distance from the core  $r$ , and expected to vary from 1 at small  $r$  to zero at large  $r$ . This function is expected to depend on the shower's energy, composition, and zenith angle.

To estimate this, IceTop detector simulations were run in a mode in which only certain particle components were propagated to the tanks (for instance, “electromagnetic only” or “muons only”), and the individual signals measured. The signals from these individual components as a function of radius can be fit to parabolas in log-log space ( $\log_{10}(S)$  vs  $\log_{10}(r)$ ). The ratio of the electromagnetic curve to the total is shown in Figure 6. Fits to the log-log parabolas for the 0-degree and 25-degree curves (which are very similar in Figure 6) as a function of  $\log E$  can be used to estimate  $f_{EM}$  for each tank in real IceTop events according to their radius from the core and the reconstructed energy of the event.

- *Estimate the shower evolution  $t$  for each shower.*

Because IceTop only samples particles at ground level, estimating the stage of shower evolution with this detector is a challenge. In theory, the shower *age* should be related to  $t$ . The lateral distribution function model used for IceTop signals does include a slope parameter called  $\beta$ , which is related to the shower age [1], but this variable appears to not be robust for this purpose in initial testing. If the signal can be modeled by two lateral distribution functions, a Nishimura-Kamata-Greisen function for the electromagnetic component and a separate function for muons [12, 13], then the age of the electromagnetic component may be a better estimator.

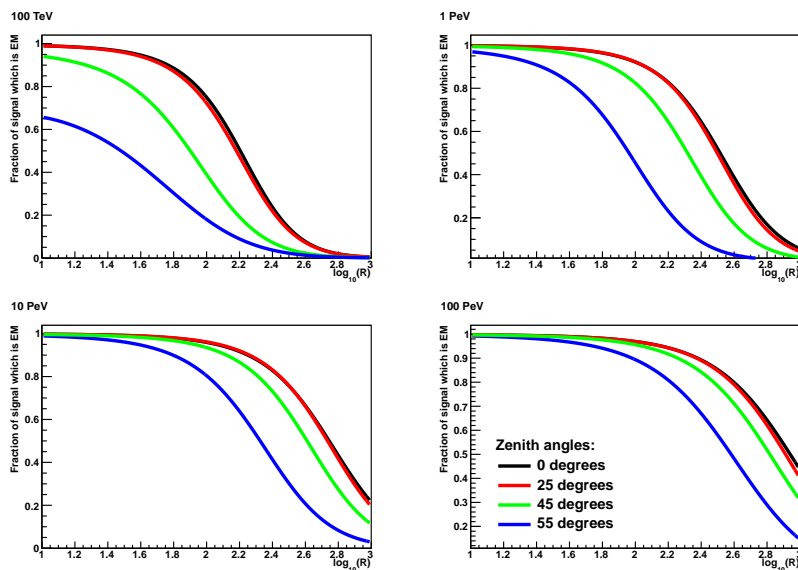


**Figure 6:** Fraction of the signal which is electromagnetic, broken down by energy (the four different panels) and by zenith angle (the four colors).

## References

- [1] R. Abbasi et al. *NIM*, **A700**, (2013) 188-220.
- [2] R. Abbasi et al. (IceCube Collab.) *Astropart. Phys.*, **42**, (2013) 33.
- [3] M.G. Aartsen et al. (IceCube Collab.) *Phys. Rev. D*, **88**, (2013) 042004.
- [4] T. Feusels et al. (IceCube Collab.) “Cosmic Ray Composition and Energy Spectrum between 2.5 PeV and 1 EeV with IceTop and IceCube”, *Proc. of the 33rd ICRC (Rio de Janeiro)*, paper 0861 (2013)
- [5] K. Rawlins et al. (IceCube Collab.), PoS(ICRC2015)334, these proceedings
- [6] K. Rawlins et al. (IceCube Collab.) “The Effect of Snow Accumulation on Signals in IceTop”, *Proc. of the 33rd ICRC (Rio de Janeiro)*, paper 1106 (2013)
- [7] D. Heck et al., Report FZKA 6019 (1998).
- [8] G. Battistoni et al., *AIP Conference proceedings* **896**, (2007) 31.
- [9] S. Agostinelli et al., *Nucl. Instrum. Meth. A* **506**, (2003) 250.
- [10] P. Lipari, *Phys. Rev. D* **79**, (2009) 063001.
- [11] S. Lafebre, et al. *Astropart. Phys.* **31**, (2009) 243.
- [12] J. Nishimura and K. Kamata, *Progr. Theor. Phys.* **6** (1958) 93.  
K. Greisen, *Ann. Rev. Nucl. Part. Sci.* **10** (1960) 63.
- [13] J. Gonzalez et al. (IceCube Collab.), PoS(ICRC2015)338, these proceedings

## IceTop as Veto for IceCube

---

### The IceCube Collaboration<sup>†</sup>,

<sup>†</sup> [http://icecube.wisc.edu/collaboration/authors/icrc15\\_icecube](http://icecube.wisc.edu/collaboration/authors/icrc15_icecube)

*E-mail:* [delia.tosi@icecube.wisc.edu](mailto:delia.tosi@icecube.wisc.edu)

The IceCube neutrino observatory includes a surface array, IceTop, designed to detect and study cosmic rays. This array, located directly above IceCube, can be used to distinguish astrophysical neutrinos from atmospheric neutrinos and penetrating muons, increasing the effective volume of the IceCube detector for the southern sky. In this contribution we present the efficiency of such a veto technique as a function of energy, and compare data and simulation. In particular we focus on one event which was found in a separate analysis (starting event search) in IceCube and passing through IceTop and we study the probability of this event being background.

**Corresponding authors:** K. Jero<sup>1</sup>, D. Tosi<sup>\*1</sup>,

<sup>1</sup>*Dept. of Physics and Wisconsin IceCube Particle Astrophysics Center, University of Wisconsin, Madison, WI 53706, USA*

*The 34th International Cosmic Ray Conference,  
30 July- 6 August, 2015  
The Hague, The Netherlands*

---

\*Speaker.

## 1. Introduction

The IceCube observatory, completed in 2010, is a particle detector located at the geographic South Pole [1]. The experiment features two major detectors, one buried in ice and the other on the ice surface. The in-ice neutrino telescope, IceCube, consists of 86 strings equipped with 60 optical sensors each, instrumenting a volume of a cubic kilometer. The optical sensors are installed between depths of 1450 m and 2450 m in the ice sheet. The IceTop air shower array consists of 81 stations located near the top of each in-ice string. A station consists of two frozen water tanks, each equipped with two optical sensors. The optical sensors (digital optical modules, DOMs) of both arrays detect the Cherenkov radiation emitted by secondary charged particles. On the surface, these are charged leptons produced in hadronic or electromagnetic interactions in the atmosphere. In ice, these are either penetrating muons from showers, or particles produced by neutrino interactions in the Antarctic ice cap or in the bedrock.

The discovery of an astrophysical neutrino flux [2] was achieved in 2013 by using the outer layer of the in-ice detector as a veto. This technique allows high energy events to be distinguished as starting inside the detector or coming from the outside, with the former indicating the events are astrophysical neutrino interactions. Variations of this method have been implemented to improve sensitivity and widen its energy range [3]. IceTop was designed to measure the spectrum and composition of cosmic ray particles in the energy range between  $10^{14}$  and  $10^{18}$  eV, exploiting the relationship between air shower energy and the energy of penetrating muons (as detected by the in-ice detector) [4]. In this paper we investigate the possibility of using IceTop as a veto for IceCube. The location of the detector makes it a suitable instrument to tag air shower particles which accompany muons that penetrate deep into the ice. This veto could create a background free phase space for down-going astrophysical neutrinos undergoing a charged current interaction between IceTop and the in-ice detector, which are currently not detectable by any other analysis. This study aims to determine the efficiency of IceTop as a veto for IceCube, and its energy threshold, with an improved methodology as compared to [5]. In particular this analysis focuses on events which cross both the IceCube array and IceTop. We call these events "vertical events".

While this analysis was being developed, a vertically down-going muon neutrino was found in the starting event analysis [6]. The interaction vertex is reconstructed near the horizontal center of the detector, after the neutrino candidate has passed more than 10 layers of DOMs. The outgoing muon travels nearly vertically and deposits over 400 TeV in the detector. It is highly improbable that the particle whose interaction generated the event was a muon which did not emit detectable amounts of light before the reconstructed vertex. Additionally, the findings of [7] show that only neutrinos produced by charmed mesons in the atmosphere can be a background to this event. From dedicated simulations with CORSIKA [8] utilizing the DPMJET II.5 [9] hadronic model, a background of one event per  $\sim 390.5$  years was found to be accompanied by a muon bundle with less than 300 GeV energy. Since DPMJET II.5 is known to overproduce charm muons and neutrinos, this simulation alone provides a conservative estimate that this event is a  $3\sigma$  deviation from background. As such, it is interesting to consider this event within the framework of an IceTop veto. In the following sections data selection, background and signal estimation are presented. The presented analysis was performed on 102 days of data between 2012 and 2014.

## 2. Data selection

The data collected by the IceCube observatory is transferred to the northern hemisphere by satellite and therefore must be greatly reduced in rate before transmission. Several filters are in place to select events which are interesting for one or the other analysis. In the analysis presented here the events of interest are down-going bright vertical events which pass through both IceTop and IceCube. The most suitable stream for this analysis is the one containing events which triggered the in-ice detector with a charge greater than one thousand photoelectrons (PE). The typical trigger rate for this stream is between 1 and 2 Hz. Events passing very close to a DOM may deposit a disproportionate amount of charge into that DOM with respect to the charge detected in all the other DOMs, leading to an out-of-ordinary value of the charge for events which are otherwise not very bright. To account correctly for this effect, the total number of photoelectrons is recalculated by removing the DOMs which have more than 50% of total charge. This quantity is called "homogenized total charge" ( $Q_{\text{toth}}$ ). Passing events are required to have  $Q_{\text{toth}} > 1000$  PE.

The direction of each event is reconstructed using a likelihood-based algorithm (see section 3). The track is required to have a length greater than 800 m in IceCube (as measured along the reconstructed direction) and a trajectory such that the extrapolated intersection with the ice cap surface (impact point) lies inside the perimeter of IceTop by at least 75 m. This series of cuts reduces the data rate to 2.8% of the original trigger level where only 1000 PE in ice was required. Events selected by these containment cuts are muon tracks reconstructed to sub-degree angular resolution. A sample of extrapolated impact points and the distribution of reconstructed zenith angles for all events are shown in fig. 2 and fig. 3 respectively.

The time of impact at each DOM on the surface ( $t_{0i}$ ) is calculated for a hypothetical shower generating the reconstructed track of the muon/muon bundle. Pulses recorded by IceTop DOMs are then processed to remove redundant information, leaving a unique time for each hit tank. The difference ( $t_i - t_{0i}$ ) between the hit time ( $t_i$ ) and the expected arrival time of the shower ( $t_{0i}$ ) is calculated, and shown as the distribution in fig. 4.

Most of the hits are recorded at the predicted time and in a window of a few hundred nanosecond afterwards. This distribution is used as a template to establish the likelihood of a hit to be correlated with a shower, rescaled so that the maximum value is one. In this construction, a hit in perfect time will be counted as one hit while early and late hits will be penalized proportionally to how often they are observed to occur. This smooth weighting strategy does not require an arbitrary time window but naturally takes into account all the hits recorded (an improvement compared to [5]). The sum of weighted IceTop hits ("wHits") produces a floating value for each event which can span from 0.0 (no tanks having any hit) to 162.0 (all tanks having a hit at the shower time).

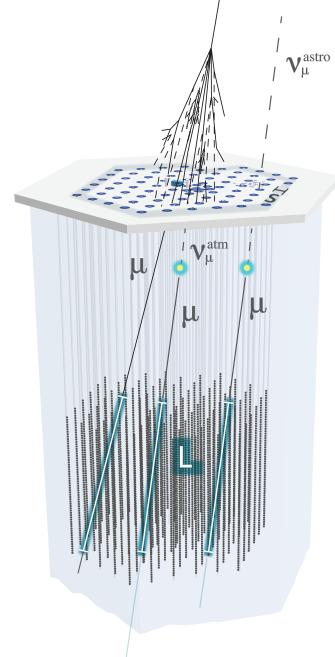


Figure 1: Illustration of the cuts used to select events for this analysis:  $L \geq 800$  m and  $S \geq 75$  m.

To determine a proxy to the muon energy, the expected number of photons is fitted via an analytic template which scales with the energy of the muon. This calculation leads to an energy estimator, called "MuEx" [10], which is more sophisticated than Qtoth and accounts for energy losses outside the detector. In the following, this energy proxy is given in units which can be roughly interpreted as GeV, but this should be not interpreted as the true value of the energy of the muon or muon bundle. A calibration to muon energy needs a high statistics simulation. In another analysis the value of MuEx has been found to correspond to about half the energy of the muon/muon bundle [11]. However, since the calibration depends on the specific cuts of each analysis, this should not be taken as the correct conversion factor for this analysis.

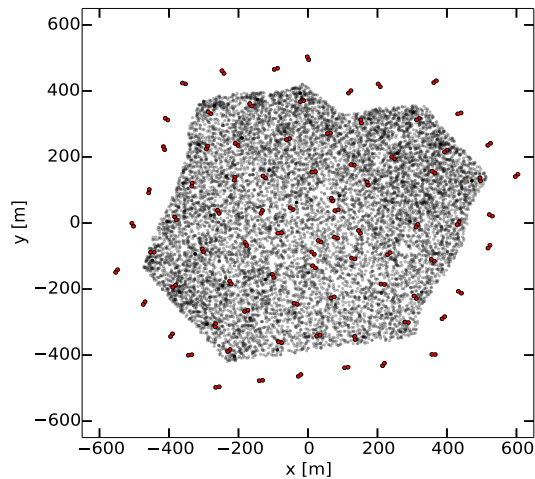


Figure 2: Distribution of a sample of selected events in surface coordinates.

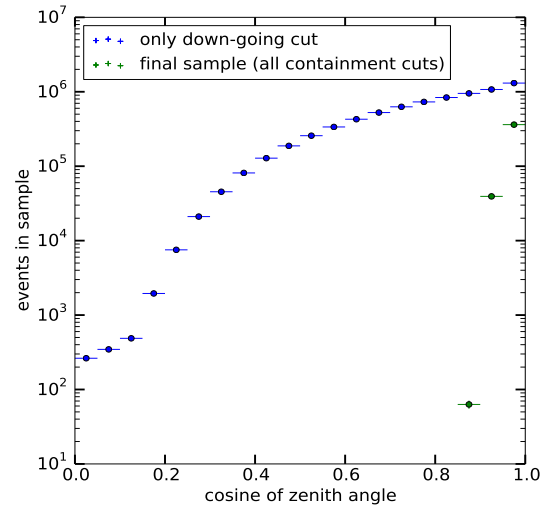


Figure 3: Distribution of events as a function of cosine of zenith angle for down-going events and for the final sample which selects vertical events ( $\cos(\theta) > 0.85$ ).

### 3. Simulation

In order to save time and space in generating a simulation set, the generation was targeted to mimic the background of the vertically down-going starting track discussed in section 1. The air shower simulation code CORSIKA [8] was modified and used to generate the particles at ground which were then simulated as events in the detectors using the standard IceTop and IceCube simulation tools. The development of the shower was modified to simulate the hadronic and muonic portions while holding the electro-magnetic component. If the total muon energy was found to be below the deposited energy of the specimen event, then the shower was discarded and the propagation time saved. DPMJET II.5 was used for the reasons mentioned in section 1.

The dataset produced, equivalent to 0.1 year in the phase space relevant to the candidate neutrino (see section 4), was used to validate this new simulation technique and for reconstruction verification. Although this test set is not sufficient to serve the scope of the analysis presented here, it was used to compare the performance of different reconstruction algorithms. The best performance in terms of time extrapolation and zenith reconstruction was found to be achieved by a

two-step reconstruction algorithm. A likelihood-based algorithm, performed in the offline processing of the stream selected at trigger level, is used as best guess for direction and vertex position. This algorithm fits the first arrival times and charge of detected photoelectrons on all the DOMs in the detector, assuming that the arriving light is originating from a muon moving at the speed of light and emitting Cherenkov radiation. The Cherenkov radiation loses intensity as it moves away from the muon, according to a simple analytic parameterization of photon propagation in ice. This reconstructed direction is then used as seed for a second fitting algorithm, which fits for the time of the interaction using only the time of the first unscattered photon and the total charge in each DOM. The combination of these steps provides better agreement between true and reconstructed values in simulation.

#### 4. Background estimation

The distribution of events in the space of wHits and energy proxy MuEx is shown in fig. 5, normalized (for visualization purpose) by the events in each MuEx bin. At low energy, there appears to be a turn-on feature which is caused by selecting data on a different energy proxy (Qtoth) (see section 2). The value of wHits is correlated with the energy since higher energy showers will produce on average more hits in IceTop synchronously with the shower. The spread of wHits is also reduced at high energy as the total value of wHits is dominated by the high-weight hits.

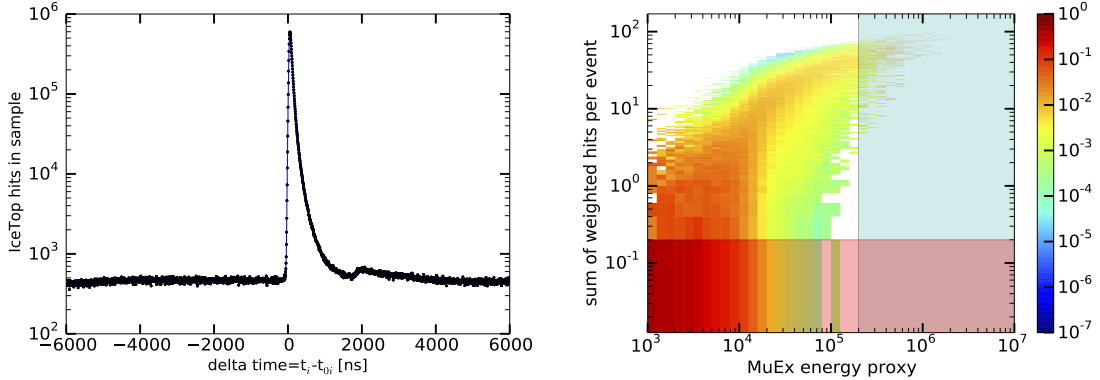


Figure 4: IceTop hit times minus arrival time of shower at surface, as extrapolated from the fit performed on pulses recorded in ice. The weight of an IceTop hit is calculated from this template after rescaling it so that the maximum is 1.

Figure 5: 2D histogram of all the events selected as a function of MuEx and IceTop weighted hits. For visualization reasons, the histogram is normalized by the number of entries in each energy bin. For shaded areas refer to text.

A detected flux from astrophysical neutrinos would populate a specific area in the phase space of high energy and low wHits (bottom right of the histogram) since astrophysical neutrinos would have IceTop hits only due to random coincidences and noise hits. In our sample, no cosmic ray events above  $\text{MuEx} \approx 2 \times 10^5$  have less than  $\text{wHits} = 1$ .

The distribution of showers observed in the sample here analyzed appears to be steeply falling towards the region of interest. Rare events (such as muons from prompt decay, or unusual showers which develop after an early or a late interaction, creating exceptional muons), not visible in the



sample, may disrupt the distribution or introduce a change in slope. In order to properly estimate the background of cosmic rays in the region of interest, a comprehensive simulation including all these phenomena with high statistics is needed. Since no such simulation has been produced so far, it is conceivable to attempt to extrapolate the background into the region of interest from the data, assuming that the population of cosmic rays follows smoothly the distribution observed.

To do so, two methods can be envisioned. The first method is based on looking at the wHits distribution of showers with an energy proxy value above a certain threshold: from this distribution, mostly concentrated at high wHits, one can extrapolate the rate of events expected at low wHits. This means integrating in energy to the right of the vertical line in the fig. 5 (green shaded area) and projecting to the wHits axis. The second method is based on looking at the energy distribution of showers with less than a maximum acceptable value of wHits (for example 0.2): from this distribution one can extrapolate the expected rate for a certain value of energy proxy. This is equivalent to integrating the 2-dimensional distribution in wHits from 0.0 up to the chosen value of wHits (red shaded area in fig. 5) and then projecting it on the energy proxy axis.

The two methods should provide a consistent estimation of the background for the same bin. The first method, however, is difficult to apply because of the low statistics at high energy and because of the large gap between the data and extrapolation region. In addition, the lack of a proper fit model makes any fit of the data difficult. The second method offers the advantage of higher statistics and is therefore more robust and reliable with the current set of data analyzed.

## 5. Signal estimation

Neutrino-generator, a Monte Carlo simulation program based on ANIS [13] with CTEQ cross section tables is used to generate neutrinos and propagate them through the Earth. The neutrinos are forced to interact before passing through the detector and are assigned a weight. For this analysis a general purpose dataset of muon neutrinos with a spectrum of  $E^{-1}$  over an angular range of  $0^\circ \leq \theta \leq 180^\circ$  and energy range of  $10^2 \text{ GeV} \leq E_\nu \leq 10^7 \text{ GeV}$  was used. The same data selection criteria as explained in section 2 was applied. To obtain the signal spectrum (shown in fig. 6) the surviving events were re-weighted to the best fit astrophysical neutrino spectrum of [12]  $E^2 \phi(E) = 1.5 \times 10^{-8} (E/100 \text{ TeV})^{-0.3} \text{ GeV cm}^{-2} \text{ s}^{-1} \text{ sr}^{-1}$ . From the observed event rate the expected number of events above a certain energy threshold was calculated.

## 6. Sensitivity

By lowering the maximum allowed value of wHits, it is possible to increase the rejection power of the veto and lower the energy threshold above which the veto is efficient. The trend is shown in

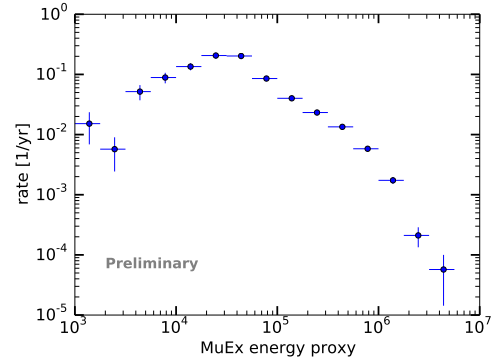


Figure 6: Expected neutrino rate (from simulation) vs reconstructed energy proxy using the best fit astrophysical flux from [12].

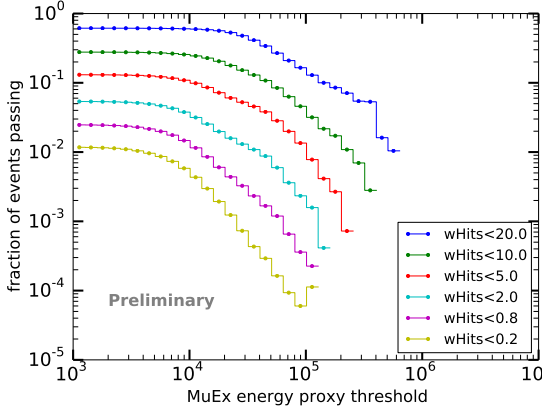


Figure 7: Fraction of events with less than a certain value of wHits.

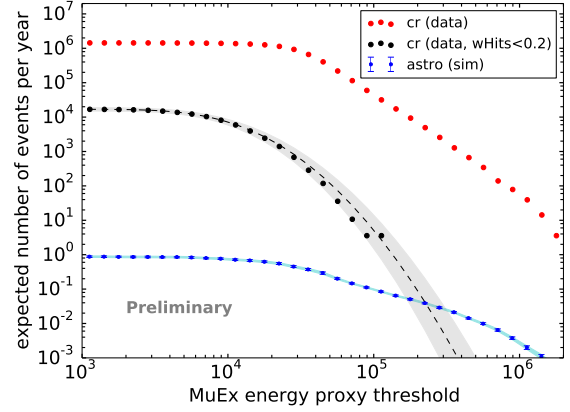


Figure 8: Observed background rate and expected neutrino signal versus energy proxy threshold.

fig. 7 for some example values of wHits. Fig. 8 shows the number of expected neutrino (blue line) and background events (black dots) above a certain threshold for the energy proxy, rescaled to one year, for events with a wHits value less than 0.2. The total number of events in the selection (i.e. all the events shown in fig. 5) is shown in red. The energy threshold at which the signal expectation exceeds the background is roughly  $2 \times 10^5$  MuEx, and the expected number of neutrino events is 0.1 per year, primarily due to the very small solid angle to which this analysis is sensitive.

No events in the sample exceed the  $5 \sigma$  error band of the background estimation. The brightest event in the sample with  $w\text{Hits} < 0.2$  has a MuEx value of  $104 \times 10^3$  and a wHits value of 0.03. The bright vertical event found by the starting event analysis has a MuEx value of  $180 \times 10^3$  and 13 hits for a value of wHits of less than 0.01, so it would be slightly above the background.

For comparison fig. 9 shows the event viewer of the muon neutrino candidate, while fig. 10 shows a shower of similar energy which lights up IceTop ( $w\text{Hits} \approx 47$ ) and is reconstructed by IceTop as having an energy of 7.5 PeV.

## 7. Outlook

Several improvements to this analysis are under investigation. The value of wHits can be optimized with a more detailed study of the background. The distance of a hit DOM from the impact point can be used as additional information in establishing the weight of each hit. The effect of the angular resolution of individual events on the veto probability is under study. Higher statistics might make possible the extrapolation of background along the wHits axis and lead to increased analysis efficiency.

This analysis allows for the first time a measurement of the veto potential of IceTop against cosmic ray muon and neutrino background. A proper understanding using data and simulation will allow for reliable predictions of the veto efficiency of a large ( $\sim 100 \text{ km}^2$ ) array as is currently envisioned for a future upgrade of IceCube [14] [15] [16].

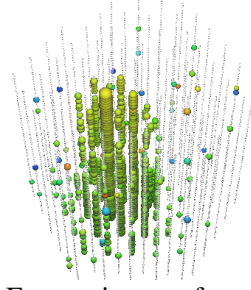
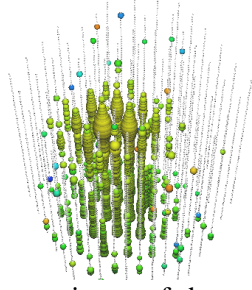
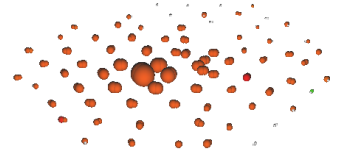
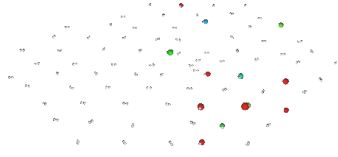


Figure 9: Event viewer of the candidate muon neutrino event starting in the detector, found by the starting track analysis. The dot colors indicate the relative time of hits (red: first, blue: last), the size indicates the amount of charge detected by each DOM. MuEx value for this event is  $\approx 180 \times 10^3$ , wHits is 0.03.

Figure 10: Event viewer of a typical shower which produces a muon bundle of energy similar to the energy of the neutrino candidate event in fig. 9. MuEx value is  $\approx 180 \times 10^3$  and wHits is 47.

## References

- [1] **IceCube** Collaboration, A. Achterberg et al., *Astropart. Phys.* **26** (2006) 155.
- [2] **IceCube** Collaboration, M. G. Aartsen et al., *Science* **342** (2013) 1242856.
- [3] **IceCube** Collaboration, M. G. Aartsen et al., *Phys. Rev. D* **91** (2015) 022001.
- [4] **IceCube** Collaboration, *PoS(ICRC2015)334, these proceedings.*
- [5] **IceCube** Collaboration, M. G. Aartsen et al., *The IceCube Neutrino Observatory Part VI: Ice Properties, Reconstruction and Future Developments, Proc. 33rd ICRC.*
- [6] **IceCube** Collaboration, *PoS(ICRC2015)1081, these proceedings.*
- [7] A. K. T. Gaisser, K. Jero and J. van Santen, *Phys. Rev. D* **90** (2014) 23009.
- [8] J. C. G. S. D. Heck, J. Knapp and T. Thouw, *Tech. Rep. FZKA* **6019** (1998).
- [9] J. Ranft, *Phys. Rev. D* **51** (1995) 64.
- [10] **IceCube** Collaboration, M. G. Aartsen et al., *J. Inst.* **9** (2014) P03009.
- [11] **IceCube** Collaboration, M. G. Aartsen et al., [arXiv:1507.0400](https://arxiv.org/abs/1507.0400).
- [12] **IceCube** Collaboration, M. G. Aartsen et al., *Phys. Rev. Lett.* **113** (2014) 101101.
- [13] A. Gazizov and M. P. Kowalski, *Comput. Phys. Commun.* **172** (2005) 203.
- [14] **IceCube** Collaboration, *PoS(ICRC2015)1146, these proceedings.*
- [15] **IceCube** Collaboration, *PoS(ICRC2015)1070, these proceedings.*
- [16] **IceCube** Collaboration, *PoS(ICRC2015)1156, these proceedings.*

